

*Ab initio* embedded cluster study of optical  
second harmonic generation below the gap  
of the NiO(001) surface



**Dissertation**

zur Erlangung des akademischen Grades  
doctor rerum naturalium (Dr. rer. nat.)

vorgelegt der

Mathematisch-Naturwissenschaftlich-Technischen Fakultät  
(mathematisch-naturwissenschaftlicher Bereich)  
der Martin-Luther-Universität Halle-Wittenberg

von

Frau Khompat Satitkovitchai  
geboren am 22.03.1972 in Bangkok

Gutachter:

1. Prof. Dr. W. Hübner
2. Prof. Dr. V. Staemmler
3. PD Dr. A. Chassé

Halle a.d. Saale, den 7. Mai 2003  
Tag der mündlichen Prüfung: 14. Nov 2003

**urn:nbn:de:gbv:3-000005840**

[<http://nbn-resolving.de/urn/resolver.pl?urn=nbn%3Ade%3Agbv%3A3-000005840>]



# Contents

Abbreviations . . . . .	3
<b>1 Introduction</b>	<b>5</b>
1.1 Motivation for a theoretical framework . . . . .	6
1.2 Why Quantum Chemistry . . . . .	7
1.3 The scope of this work . . . . .	8
<b>2 NiO</b>	<b>11</b>
2.1 Experimental and theoretical studies . . . . .	11
2.2 NiO and its low-lying excited states . . . . .	13
2.3 Second Harmonic Generation . . . . .	14
<b>3 Materials and methods</b>	<b>17</b>
3.1 Quantum chemistry methods and background . . . . .	17
3.1.1 Hartree-Fock method . . . . .	17
3.1.2 Configuration Interaction (CI) approach . . . . .	20
3.1.3 Spin-orbit coupling . . . . .	25
3.2 Method implementation . . . . .	27
3.2.1 <i>Ab initio</i> embedded cluster method . . . . .	27
3.2.2 Improvements of electron correlation . . . . .	29
3.2.3 Treatment of spin-orbit coupling . . . . .	29
3.3 Nonlinear optical surface response . . . . .	30
<b>4 Results and Discussion</b>	<b>33</b>
4.1 Ground state properties . . . . .	33
4.2 Excited states and optical properties . . . . .	34
4.2.1 Madelung field effects . . . . .	34
4.2.2 CIS results and optical properties . . . . .	35
4.2.3 Optical gap . . . . .	36
4.2.4 Excitation spectra of NiO(001) surface . . . . .	37
4.2.5 Oscillator strengths and optical absorption spectra . . . . .	37
4.2.6 Electronic correlation effects on <i>d-d</i> transitions . . . . .	37
4.2.7 <i>d-d</i> transitions . . . . .	39
4.3 Electron density . . . . .	40
4.3.1 NiO(001) surface . . . . .	41

4.3.2	Bulk NiO . . . . .	48
4.4	Inclusion of spin-orbit coupling . . . . .	55
4.4.1	Crystal field theory and the Shubnikov point groups . . . . .	55
4.4.2	Fine structure of the bulk NiO and NiO(001) surface . . . . .	60
4.5	SHG intensity . . . . .	66
<b>5</b>	<b>Conclusions</b>	<b>71</b>
	<b>Appendices</b>	<b>75</b>
A	Basis sets and effective core potentials used in calculations . . . . .	75
B	The relativistic effective core potentials . . . . .	76
	<b>Bibliography</b>	<b>81</b>

## Abbreviations

AF <sub>1</sub>	fcc type I antiferromagnet
AF <sub>2</sub>	fcc type II antiferromagnet
AO	atomic orbital
BIS	bremsstrahlung isochromat spectroscopy
CASPT2	complete active space with second-order perturbation theory
CASSCF	complete active space self-consistent field method
CC	coupled cluster method
CCSD	CC calculation including single and double excitations
CCSD(T)	CCSD with perturbative treatment of triple excitations
CI	configuration interaction approach
CID	CI calculation with all double substitutions
CIS	CI calculation with all single substitutions
CIS-MP2	CIS with the second-order Møller-Plesset perturbative correction involving single and double substitutions from the reference state
CISD	CI calculation with all single and double substitutions
DHF	Dirac-Hartree-Fock equations
DOS	density of states
ECP	effective core potential
ED	electric-dipole
EELS	electron energy loss spectroscopy
FM	ferromagnet
FWHM	full width at half maximum
GGA	generalized gradient approximation
GTO	Gaussian type orbital
GUGA	graphical unitary group approach
GW	approximation for the self-energy $\Sigma(12) = iG(12)W(1+2)$
HF	Hartree-Fock approximation
HOMO	highest occupied molecular orbital
LanL2DZ	the Los Alamos National Laboratory second Double-Zeta basis set
LCAO	linear combination of atomic orbitals
LDA	local density approximation
LEED	low-energy electron diffraction
LSDA	local spin density approximation
LUMO	lowest unoccupied molecular orbital
MC-SCF	multiconfiguration self-consistent field
MD	magnetic-dipole
MO	molecular orbital
MP	Møller-Plesset perturbation theory
MP2	the second-order Møller-Plesset perturbation theory
MP4	the fourth-order Møller-Plesset perturbation theory

MRAMs	magnetic random access memories
MRCISD	multi-reference CI singles and doubles
QCI	quadratic configuration interaction approach
QCISD	QCI calculation with single and double excitations
QCISD(T)	QCISD with perturbative treatment of triple excitations
RAMs	random access memories
ROHF	restricted open-shell HF approximation
SCF	self-consistent field
SIC	self-interaction correction
SHG	second harmonic generation
STO	Slater type orbital
TMs	transition metals
TMOs	transition metal oxides
TMR	tunneling magnetoresistance
UHF	unrestricted Hartree-Fock approximation
XAS	x-ray absorption spectroscopy
XPS	x-ray photoemission spectroscopy

# Chapter 1

## Introduction

Among the materials, which are of interest for physical science and technology, transition-metals (TMs) are outstanding for their special characteristics and different and widespread uses. They have attracted the attention of many researchers for a long time, for their unique physicochemical properties about the electronic structure. The description of the electronic structure of TM materials is responsible for their properties. All TMs have the common properties of metals such as being very hard, possessing high density, retaining high melting and boiling points, exhibiting high electrical conductivity, etc. Indeed, there are four such series of TMs which can be distinguished depending on the partially filled  $d$ -orbitals. Thus, for the first TMs series e.g. Scandium (Sc) through Copper (Cu), the electronic configuration of the outer orbitals is  $4s^2$ , while the second outer orbitals (i.e. the  $3d$  shell) are incompletely occupied. The second series consists of Yttrium (Y) through Silver (Ag), which the  $4d$  orbital are incompletely filled. Lanthanum (La), Hafnium (Hf) through Gold (Au) are the third series in which the  $5d$  shell is partially filled, while the incomplete  $6d$  orbitals are found in the fourth transition series (e.g. Actinium (Ac), the  $104^{th}$  element through the  $109^{th}$  element). In addition, it was discovered that they could easily form complexes with one or more other elements, e.g. a halogen (F, Cl, ...) or a chalcogen (O, S, ...). Furthermore, these compounds show a variety of properties depending on the composition. Compounds of the TMs can be paramagnetic or diamagnetic. Paramagnetism in the TMs is caused by unpaired electrons in the  $d$ -orbitals, which can be affected by a magnetic field. Diamagnetism is hardly affected by a magnetic field since all electrons are paired in the  $d$ -orbitals. Some transition metal compounds form colored characteristics, which enables to absorb specific frequencies of light. Moreover, the TM compounds even exhibit a wide range of electrical conductivities, from insulator to superconductor.

The most interesting transition-metal compounds today are the transition-metal oxides. These materials show rich variety of phenomena, e.g. Mott transition, high- $T_c$  superconductivity, ferromagnetism, antiferromagnetism, low-spin/high-spin transitions, ferroelectricity, antiferroelectricity, colossal magnetoresistance, charge ordering, and bipolaron formation [1]. These appear to behave as numerous important phenomena in condensed matter physics. The main actors in these phenomena are the  $d$ -orbitals of the TMs ions surrounded by oxygen ions. The  $d$ -orbitals extend to attract the oxygen ions and are subject to the crystal fields. This manner gives rise to the splitting of the  $d$ -orbitals. In the octahedral symmetry, which

corresponds to the three-dimensional rocksalt structure, the five  $d$ -orbitals are shifted into two  $e_g$  orbitals ( $x^2 - y^2$ ,  $3z^2 - r^2$ ) and three  $t_{2g}$  orbitals ( $xy$ ,  $yz$ ,  $xz$ ). When the symmetry is reduced, the further splitting occurs. These subjects are interesting from both points of view of physics and chemistry.

Of particular interest in this active research is an optical gap<sup>1</sup>, which involves the crucial description of the optical properties. Of course, this optical behavior forms the basis for many important applications. The gap widths of TMO have been determined by several experimental methods [2], such as optical absorption spectroscopy, electron energy-loss spectroscopy, and photoconductivity and electroreflectance measurements. The differences in the published gap widths arise mainly from different gap definitions, and it seems to be more or less a matter of taste which is preferred.

In an earlier series of articles [3, 4, 5, 6, 7, 8], it has been shown that the transition metal oxides such as MnO, FeO, CoO, and NiO are regarded as Mott insulator concept. The definition of a Mott insulator is described by the following notion. For a Mott insulator the electron-electron interaction leads to the occurrence of (relative) local moments. The gap in the excitation spectrum for charge excitations may arise either from the long-range order of the pre-formed moments (Mott-Heisenberg insulator) or by a quantum phase transition induced by charge and/or spin correlations (Mott-Hubbard insulator) [9].

More recently, the transition metal oxides MnO, FeO, CoO, and NiO are known to reveal the second kind of antiferromagnetic compounds forming in the rocksalt structure, whose band gap is specified by charge-transfer excitations ( $p \rightarrow d$ ), not  $d \rightarrow d$  transitions [10, 11, 12, 13]. This type of transition is intrinsically much more intense than the  $d-d$  kind treated by the crystal field theory, and may often be important in the optical properties of solids. Therefore, the electronic structure of TMO can be described as band structure of an ionic insulator supplied with the local states of  $d$ -electrons [14].

## 1.1 Motivation for a theoretical framework

Future computer memories require a merger between the existing technologies of permanent (magnetic) information storage and random access memories (RAMs). The envisaged magnetic random access memories (MRAMs) [15] are assumed to be faster and non-volatile while beating the contemporary designs also in storage density. One of the most successful approaches so far is based on tunneling magnetoresistance (TMR) junctions, where the relative magnetization direction of two ferromagnetic metallic layers governs the tunneling rate through an insulator placed between them (reading). The magnetization of one of the ferromagnetic layers can be adjusted (writing), while the other ferromagnetic layer is usually pinned by an antiferromagnet. For such a design, transition-metal oxides (TMOs) such as NiO are of interest since they are *both* insulating and antiferromagnetic. One of the crucial elements of the proposed device is the metal-TMO interface. The properties of this interface can conveniently be assessed by the technique of optical second harmonic generation (SHG),

---

<sup>1</sup> The gap is not describable in term of single-particle band structure calculation or HOMO-LUMO gap (HOMO and LUMO mean the highest occupied molecular orbital and the lowest unoccupied molecular orbital, respectively).

which is highly sensitive to antiferromagnetism occurring at surfaces and interfaces of materials which possess central symmetry [16, 17, 18]. Furthermore, SHG has the unique potential to become a tool for investigating buried oxide interfaces, where other techniques fail. Until now, it has been proven to be a very useful technique for the study of ferromagnetism at surfaces. This is the reason why SHG became the subject of intensive experimental and theoretical studies [16, 19]. These technological developments require a detailed theoretical understanding of the nonlinear optical processes on TMO surfaces. This is, however, a formidable task for two main reasons: (i) an electronic *ab initio* theory of the nonlinear magneto-optical response at solid surfaces has long been in its infancy and is just about to emerge due to the enormously high-precision requirements for obtaining reliable results and (ii) transition metal oxides are notorious examples of strongly correlated electron systems that have escaped a description by even phenomenological many-body theories since the 1960s [20, 21, 22].

In view of these difficulties, any tractable theoretical attempt at the theoretically, experimentally, and technologically interesting problem of a first-principles description of nonlinear magneto-optics from the surface of NiO(001) has to start at the entry level and to leave aside a great deal of the sophistication underlying both subproblems individually, viz (i) the consistent many-body description of the electronic properties of transition metal oxide surfaces and (ii) the *ab initio* theory of nonlinear optics from a magnetic solid.

## 1.2 Why Quantum Chemistry

*Ab initio* quantum chemistry is capable of calculating a wide range of the chemical and physical phenomena of interest to a chemist or physicist. These methods can be used both to predict the results of future experiments and to assist in the interpretation of existing observations. Quantum chemistry calculations can also be a fast and inexpensive guide to the experiment necessary. Although calculations will never exclude the need for experiment, they can be a valuable tool to provide insight into chemical and physical problems that may be unavailable to the experimentalist.

By starting from first-principles and treating the molecule as a collection of positive nuclei and negative electrons moving under the influence of Coulombic potentials, the computational *ab initio* quantum chemistry attempts to solve the electronic Schrödinger equation and seeks to determine the electronic energies and wave functions. The full Schrödinger equation for a molecule  $\hat{H}\Psi = E\Psi$  involves the Hamiltonian  $\hat{H}$  containing the kinetic energies of each of the  $N$  electrons and  $M$  nuclei as well as the mutual Coulombic interactions among all of these particles ( $\frac{e^2}{r_{ij}}, i, j = 1, 2, 3, \dots, N; \frac{Z_a Z_b e^2}{R_{ab}}, a, b = 1, 2, 3, \dots, M; -\frac{Z_a e^2}{r_{ja}}, j = 1, 2, 3, \dots, N, a = 1, 2, 3, \dots, M$ ) and  $\Psi$  depending on Cartesian and spin coordinates of the component particles. Such a full Schrödinger equation has never been solved exactly for more than two-particle systems. Therefore, the essential approximation made in *ab initio* quantum chemistry is called the Born-Oppenheimer approximation [23], in which the motions of the nuclei are fixed at a geometry (denoted  $R$ ). Then, the Schrödinger equation produces the wave functions  $\psi_k(r; R)$  and the energy surfaces  $E_k(R)$  of the nuclear positions whose gradients give the forces  $F_k = -\Delta_k V$  acting on the atomic centers. Wave functions contain all information needed to compute dipole

moments, polarizability, and transition properties such as electric dipole transition strengths among states [24]. They also permit evaluation of system responses with respect to external perturbations such as geometrical distortions [25], which provides information on vibrational frequencies and reaction paths.

A point charge cluster embedding technique [26, 27, 28] is developed to model the crystalline solids. In principle, one treats quantum mechanically only a small part of the crystal lattice as the cluster. The rest of the crystal will be called the environment. The action of the environment on ions in the cluster is represented by an embedding potential,  $V_{Mad}(r_0) = \sum_k^N \frac{q_k}{|r_k - r_0|}$ . Many accurate techniques have been developed for calculating the Madelung potential at any point charges determined by lattice positions [29]. Perhaps, the best choice of calculating the exact Madelung field is the Ewald summation [30].

In this work we will present some examples of how quantum chemistry can be used to investigate the electronic and optical properties of significant metals such as NiO. In Chapter 3, section 3.1, readers are provided with an overview<sup>2</sup> of the essential concepts of quantum chemistry and the computational features that differ among commonly used methods. Here, the Hartree-Fock and configuration interaction methods are introduced. The computational steps involved in their implementation are given in section 3.2.

### 1.3 The scope of this work

In this study, we make the first step towards an *ab initio* theory of SHG from TMO surfaces and calculate optically active states on the NiO(001) surface. We first perform the computation of optical properties such as discrete excitations below the gap and continuous excitation spectra above the gap for NiO(001) within the configuration interaction singles (CIS) framework [31]. In this method, the CIS wave function is expressed as a combination of all determinants obtained by replacing one occupied orbital (from the ground-state determinant) with a virtual orbital. The single excitations do not only cause a shift of excitation energy but also allow a proper calculation of optical spectra in the UV and the visible range. In our study, we do not only perform an *ab initio* calculation to estimate *d-d* transitions but we also assess the relative importance of the different electronic correlations. In order to do so, *d-d* excitation energies are determined on several correlated levels of theory such as CI (configuration interaction) and QCI (quadratic configuration interaction) approaches [32, 33].

We now turn our attention to investigate other effects coming from the relativistic part of Hamiltonian, which describes the spin-orbit coupling. In this study we use COLUMBUS program, based on the graphical unitary group approach (GUGA), which provides us the multi-reference CI singles and doubles (MRCISD) calculations. For multi-reference calculations, CI is the simplest correlation method to use in a general way. Thus, the spin-orbit interaction can be included in the correlation step. In this part, the main features of our work are:

- Non-perturbative treatment of spin-orbit matrix elements

---

<sup>2</sup> Excellent overviews of these methods are included in: W. J. Hehre, L. Radom, P. v. R. Schleyer, and J. A. Pople, *An initio molecular orbital theory*, Wiley, New York, 1986.

- 
- Calculation on the CIS level of theory
  - Using effective spin-orbit interaction operators in the form similar to effective core potentials.

Then, we turn to the second step for developing an *ab initio* theory of SHG in NiO. We calculate the nonlinear optical response following an expression developed by Hübner and Bennemann [34].



# Chapter 2

## NiO

As stated before, the first-row transition-metal oxides are among the most interesting series of materials, exhibiting wide variations in physical properties related to electronic structure. The optical and magnetic behavior, in particular, forms the basis for the enormous range of applications. As a result, they have been the subject of extensive experimental and theoretical investigations for the past several years. In this chapter we will address some features (for a review) which form an essential background in studying these materials. Such as NiO, one of the most favored antiferromagnets, is a prototypic system for strong electronic correlations with high spin AF<sub>2</sub> structure at low temperatures and has a simple crystallographic rocksalt structure with a lattice constant of 0.417 nm (see Fig. 2.1). There are two components of spin configurations due to the non-local exchange interaction. For the first component, the direct exchange interaction between the nearest neighbour of Ni ions favors paring of spins to lower energy. For another one, a very strong interaction comes from the superexchange between the next-nearest neighbour of Ni ions [35, 36]. This makes the antiferromagnetic spin structure for the ground state of NiO.

### 2.1 Experimental and theoretical studies

In the field of solid state physics, many experimental and theoretical attempts have been made to investigate the interesting physical properties of the 3*d* transition-metal oxides, which are characterized by the partially occupied 3*d*-orbitals. This range of properties also imposes many difficult problems of scientific understanding. Especially, the insulating behavior of these materials has been extensively studied for several decades.

Mott and Hubbard have reported that the strong *d*-*d* Coulomb interaction is essential to explain why some of transition metal compounds play a major role as insulators with partially filled 3*d* bands, while the others exist as metals [3, 37]. The transport of electrical charge in the solid state is provided by electrons that are subjected to the Coulomb interaction with the ions and the other electrons. The importance of a large Coulomb interaction  $U_{dd}$  is implicit in the common Anderson superexchange theory [38], and is fundamental to concept of the Mott-Hubbard insulator. When the *d*-*d* Coulomb interaction is larger than the band width, 3*d*-orbitals are localized and the magnitude of the band gap is determined by the *d*-*d* Coulomb

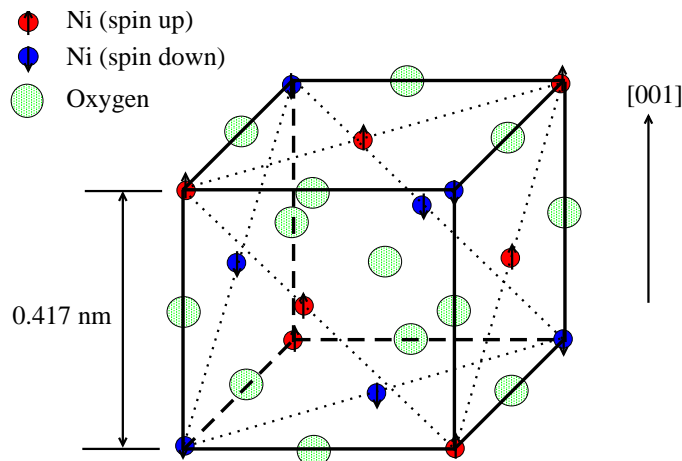


Fig. 2.1: Structure of NiO showing the AF<sub>2</sub> antiferromagnetic spin structure.

interaction.

Later, experimentally the powerful characterizations such as the combination of x-ray photoemission spectroscopy (XPS) and bremsstrahlung isochromat spectroscopy (BIS) measurements of cleaved single crystals of NiO have provided unambiguous evidence that the intrinsic charge transfer gap is 4.3 eV [39]. In addition, the band gap of  $\sim 4$  eV ( $p \rightarrow d$  character) has been indicated by a range of spectroscopic techniques including optical absorption [40], x-ray absorption spectroscopy (XAS) at the oxygen K-edge [41], and electron energy loss spectroscopy (EELS) [42]. Computationally it has been shown that the band gap of NiO is not determined by  $d-d$  Coulomb interaction, but by ligand-to- $d$  charge transfer energy ( $\Delta$ ) by analyzing the photoemission spectrum with the configuration interaction cluster model approach [43, 44]. By using this calculation, one predicts the gap of 5 eV whereas the density functional theory predicts a gap of 0.3 eV [10]. Based on the local-cluster and single-impurity approach, a classification scheme have been proposed [11], where the TMOs can be classified into two regimes according to the relative magnitude of  $\Delta$  and  $U_{dd}$ . For the Mott-Hubbard regime,  $\Delta > U_{dd}$ , the band gap is determined by  $d-d$  transition and its magnitude is given by  $U_{dd}$ . For the charge transfer regime,  $\Delta < U_{dd}$ , the magnitude of a  $p \rightarrow d$  band gap is  $\Delta$ .

Alternatively, several theoretical studies have been carried out, to understand the electronic structure and band gap of NiO. The band structure calculations of TMOs were treated by the local-spin-density approximation (LSDA) as described in Ref. [10]. This model have been successfully applied to describe many details of electronic structure, magnetic coupling, and character of the band gap since a long time. However, the local density approximation (LDA), which is widely used in solid-state physics, fails to describe the band structure of NiO as an insulator and predicts it to be as a metal [45]. This deficiency of the LDA is not fully solved by the generalized gradient approximation (GGA) level of theory, which still provides too small band gap of NiO, indicating either a metal or a semiconducting character [46, 47]. It has been suggested that the problem of the LDA (and the GGA) for properly describing a narrow band gap is related to the insufficient cancellation of the self-interaction correction (SIC) inherent in the local exchange function. The SIC-LDA introduces a better description of band gap ( $\sim 3$

eV) in the spectrum and improves the magnitude of the magnetic moment and the value of lattice constant in NiO [48, 49]. More recently, density functional calculations have tended to include modifications, such as self-interaction-corrected (SIC) LSDA [50] and LSDA+U [51]. These studies have offered improved descriptions of the Mott insulators. An analysis of the electronic and magnetic structure as well as the exchange coupling constants in bulk NiO and at the NiO(100) surface is also presented by means of SIC-LSDA approach, which improved compared with the LSDA [52]. Another method has included the self-energy in the GW (Green's function  $G$  times the dynamically screened Coulomb potential  $W$ ) approximation [22]. These studies have provided a gap of  $\sim 5.5$  eV, which is in reasonable agreement with the experimental value ( $\sim 4$  eV). Moreover, the GW approximation also improves the magnetic moments and density of states relative to LDA. This analysis has clarified some problems in the attempts of first-principles methods for the electronic structure calculation of NiO.

## 2.2 NiO and its low-lying excited states

Magnetic and optical properties of TMOs are governed by the ground state and low-energy excitation spectrum of the  $d$  shell of the central TM ion. These spectra are successfully fit to the crystal field theory [53]. Thus, it is the strong Coulomb interaction between the  $3d$  electrons that leads to an energy splitting of the  $d^n$  and  $d^{n+1}$  states. The low-lying excited states, so-called dipole-forbidden  $d-d$  transitions, appear as weak features in optical spectra. All  $d-d$  transitions violate the parity selection rule  $\Delta l = \pm 1$  (the Laporte forbidden character in centrosymmetric cases). For the earlier work, Newman and Chrenko measured the  $d-d$  transitions in bulk NiO by using absorption spectroscopy [54]. Only recently, the experimental data have become available for  $d-d$  transitions of the bulk and (001) surface of NiO [55, 56, 57, 58, 59, 60]. These results have been revealed in a range 0.5 – 3.0 eV by means of electron energy-loss spectroscopy (EELS). The great advantage of exciting such transitions with slow electrons is the possibility of excitation by electron exchange, additionally. The multiplicity-conserving ( $\Delta S = 0$ ), as well as multiplicity-changing transitions ( $\Delta S = -1$ ), are easily observable with EELS if a suitable energy of the incident electrons is chosen [2]. It has been supposed that the intensity of triplet-singlet  $d-d$  transitions in NiO depends on the antiferromagnetic ordering of the magnetic moments [61, 62, 63], yet an investigation of  $d-d$  transitions above the Néel temperature has not been reported.

The calculated  $d-d$  excitation energies of the bulk and (001) surface of NiO were investigated at first-principles unrestricted Hartree-Fock level of theory by Mackrodt and Noguera [64]. These results allow for comparisons with optical absorption and EELS and with the theoretical works based on first-principles multi-reference CEPA [55] and CASSCF/CASPT2 [65, 66] calculations of embedded clusters of the type  $(\text{NiO}_6)^{10-}$  and  $(\text{NiO}_5)^{8-}$ . From the results of these calculations, which have included electron correlation in different ways and at different levels of sophistication, it has been concluded [55, 65, 66] that the inclusion of electron correlation effects is an essential prerequisite for an accurate description of  $d-d$  excitations in NiO. These results suggest that for NiO with its highly localized  $d$ -electrons resulting from strong on-site Coulomb and exchange interaction, the contribution from electron correlation

is approximately 0.2 – 0.3 eV for the entire of one- and two-electron excitation.

## 2.3 Second Harmonic Generation

The second order nonlinear optical technique, second harmonic generation (SHG), deals with the interactions of applied electromagnetic fields in various materials to generate new electromagnetic fields, related in frequency, phase, or other physical properties. The reflected SHG intensity from media, which lack a center of inversion symmetry, is generated by the harmonic polarization in a layer about one quarter optical wavelength thick in a transparent dielectric, or in the absorption depth in the case of a strongly absorbing medium. These early observations are therefore not surface specific. SHG with a center of inversion symmetry was first observed by Terhune *et al.* [67] in calcite. They proposed a nonlinear term of quadrupolar origin in the form of a second harmonic polarization proportional to the fundamental field and its gradient. Pershan [68] showed that in media with inversion symmetry the second harmonic polarization source term may be written in the general form,  $P_i(2\omega) = \chi_{ijk}^Q E_j(\omega) E_k(\omega)$ , where Q denotes a quadrupolar transition taken into account.

This source term in a non-absorbing dielectric is ninety degrees out of phase with the nonlinear SH polarization induced in the presence of an applied dc electric field. At such as interface a discontinuity in the normal component of electric field and in the tensor components of the quadrupolar susceptibility occur.

The developments of SHG at interfaces with inversion symmetry during the sixties are summarized in a fairly comprehensive paper by Bloembergen *et al.* [69]. Shen [70] has also reviewed the progress made during the eighties. Refined theoretical analysis carefully examined the discontinuities in the normal component of the electric field,  $E$ , as one passes from a centrosymmetric medium with dielectric constant  $\epsilon_1$  through a dipolar sheet with dielectric constant  $\epsilon'$  to a centrosymmetric medium with dielectric constant  $\epsilon_2$ . This review paper defines an effective surface nonlinear susceptibility tensor  $\chi_{ijk}^S$  which clearly delineates the three effects as:

- The electric dipole term arises from the lack of inversion symmetry at the interface. This term may be significantly enhanced by absorbed monolayers of polar molecules.
- The non-local electric quadrupolar contribution to the surface nonlinearity is controlled by the strong gradient in the normal component of the electric field. This contribution is diminished when the difference in dielectric constants or indices of refraction between the two media at the interface is small.
- The third term results from the discontinuity in the volume quadrupole moment densities of two bulk media defining the interface. The gradient operator in this case acts on  $\chi^Q$ . This term, when integrated across the interface, yields the difference of two volume susceptibilities. It represents a bulk contribution which cannot be separated from the other two specific surface contributions for one single interface.

The effective nonlinear surface tensor  $\chi_{ijk}^S(2\omega)$  must reflect the symmetry characteristic of the surface. Here the index  $i$  refers to the components of the second harmonic field, and

$j$  and  $k$  to the Cartesian components of the fundamental field. For the surface of an isotropic medium, normal to the  $z$ -direction, only three independent elements exist with the following index combinations:  $(xxz) = (xzx) = (yzy)$ ,  $(yyz)$ ,  $(zxx) = (zyy)$ , and  $(zzz)$ .

For centrosymmetric antiferromagnetic NiO, SHG spectra due to the combined contributions from magnetic-dipole (MD) and electric-dipole (ED) transitions between the  $3d^8$  levels of  $\text{Ni}^{2+}$  ion were observed by Fiebig and coworkers [17]. In this experiment, the intensity of the SH signal with distinct spectral features, which is observed in the investigated 1.6 – 2.3 eV energy range of  $2\hbar\omega$ , is comparable to the intensity measured in noncentrosymmetric compounds such as antiferromagnetic  $\text{Cr}_2\text{O}_3$  or  $\text{YMnO}_3$  in which the SH process is of the ED-type [71, 72]. They have shown that an increase of SH intensity from the forbidden ED transitions occurs due to their resonance enhancement of both the incoming and the outgoing beams (processes of MD absorption at the frequency  $\omega$  and ED emission at  $2\omega$  are resonant). A quadratic coupling of nonlinear polarization to the order parameter was also found. Fiebig *et al.* [17] reported that the  $\Gamma_3^+$ ,  $\Gamma_4^+$ ,  $\Gamma_5^+$ , and  $\Gamma_2^+$  states, into which the  ${}^3\Gamma_5^+$  state was split by the spin-orbit interaction, were clearly identified both in the absorption spectra and in the low-temperature SH spectra (in the region of lowest  $3d^8$  electronic transitions with incident and emitted [001]-polarized light). Then, they presented the energy diagram of the corresponding  $3d^8$  levels of the  $\text{Ni}^{2+}$  ion (which were split by the octahedral crystal field, the spin-orbit interaction, and the exchange field below the Néel temperature). The energy scheme derived from this experiment serves as a good reference point to our results as documented in section 4.4.2.

From the previous examples, one can conclude that SH generation is a versatile tool that might have numerous technological and experimental applications. In particular, applying it to NiO, it can be used for characterization of its magnetic structure. It is known that for this antiferromagnetic material with a Néel temperature of 523 K, several magnetic-moment ordering types are possible. However, the observation<sup>1</sup> in this material from the linear optical experiments is more complicated than in ferromagnetic one since the reduction of the spatial symmetry is not linked to an imbalance in the occupation of majority- and minority-spin states. In recent years, Dähn *et al.* [18] have shown the symmetry arguments how optical SHG can be used to detect antiferromagnetic spin arrangements at surfaces and in thin films and also to separate antiferromagnetic phases from the paramagnetic and ferromagnetic ones. This is a remarkable fact since paramagnetic structure exhibits an inversion symmetry as the antiferromagnetic state. However, the two states usually differ in the allowed space transformations, and this fact can be used to detect different phases by using different polarizations of incoming light. The full classification of all possible SH responses from the domains of antiferromagnets is presented in Ref. [73]. Theoretically, the SHG response was described in the paper of Hübner and Bennemann [34]. The expression for the nonlinear optical susceptibility tensor,  $\chi$ , was obtained from the corresponding electronic structure of material.

---

<sup>1</sup> Recently, a spatially resolved polarization dependent x-ray absorption spectroscopy was used in order to fully characterize the AF structure at the surface of NiO. All 12 possible domain types originating from the bulk termination were distinguished. The measurements also showed an evidence that the magnetic moments have the same orientation as in the bulk NiO which is in contrast to sputtered surfaces, where magnetic moments lie within surface plane, forming a magnetically relaxed structure.



# Chapter 3

## Materials and methods

Computational Chemistry has existed for half a century, growing from the province of a small nucleus of theoretical work to a large, significant component of scientific research. By virtue of the great flexibility and power of electronic computers, basic principles of classical and quantum mechanics are now implemented in a form which can handle the many-body problems associated with the structure and behavior of complex molecular systems.

John A. Pople (November 1997)  
(Nobel prize for chemistry 1998, together with Walter Kohn)

### 3.1 Quantum chemistry methods and background

#### 3.1.1 Hartree-Fock method

##### General method

The ‘*ab initio*’ approach relies on the closest practicable approximations that can be made to the true solutions of the Schrödinger equation, i.e. the orbital approximations (Hartree-Fock method), where a molecular orbital (MO) is expressed by a linear combination of atomic orbitals (LCAO). In this approach, the molecular probability function is represented by a Slater determinant. This many-electron function is built up from one-electron spin orbitals, which describe single electrons in the molecule. The total wave function  $\Psi$  of the  $2n$  electrons in a closed shell system is given, therefore as:

$$\Psi = \frac{1}{(2n)!^{\frac{1}{2}}} \begin{vmatrix} \psi_1(1) & \psi_1(2) & \dots & \psi_1(2n) \\ \psi_2(1) & \psi_2(2) & \dots & \psi_2(2n) \\ \vdots & \vdots & \ddots & \vdots \\ \psi_{2n}(1) & \psi_{2n}(2) & \dots & \psi_{2n}(2n) \end{vmatrix} \quad (3.1)$$

This form of wave function guarantees the antisymmetric behavior of electrons, as required for any type of fermions<sup>1</sup>. At this point, an expression for the MO's is needed. A natural way to present the MO's ( $\psi_i$ ) is by expanding them into a linear combination of atomic orbitals (AO's,  $\phi_\mu$ ):

$$\psi_i = \sum_{\mu=1}^N c_{\mu i} \phi_\mu. \quad (3.2)$$

The choice of the AO's ( $\phi$ ), in which the MO's ( $\psi$ ) are expanded, is called the basis set.

The unrestricted Hartree-Fock (UHF) method treats the  $\alpha$  and  $\beta$  spin orbitals separately. This theory has been commonly used for open-shell systems. Formally, the UHF<sup>2</sup> wave function ( $\Psi_{UHF}$ ) can be defined by two sets of coefficients,

$$\psi_i^\alpha = \sum_{\mu=1}^N c_{\mu i}^\alpha \phi_\mu; \quad (3.3)$$

$$\psi_i^\beta = \sum_{\mu=1}^N c_{\mu i}^\beta \phi_\mu. \quad (3.4)$$

The best MOs, that is those leading to the best approximation to the actual state of the molecule, are then obtained by choosing the coefficients  $c_{\mu i}$  to minimize the total energy (variation principle,  $E = \langle \Psi | H | \Psi \rangle$ ). This procedure is incorporated in the *Roothaan-Hall* equation [74], forming the basis of all '*ab initio*' MO calculations,

$$\sum_{v=1}^N (F_{\mu v} - \epsilon_i S_{\mu v}) c_{v i} = 0 \quad (3.5)$$

with the normalization condition

$$\sum_{\mu=1}^N \sum_{v=1}^N c_{\mu i}^* S_{\mu v} c_{v i} = 1 \quad (3.6)$$

where  $\epsilon_i$  is the one-electron energy of molecular orbital  $\psi_i$ ,  $S_{\mu v}$  are the elements of an  $N \times N$  matrix termed the overlap matrix, and  $c_{\mu i}$  is the matrix of the expansion coefficients.

The matrix representation of the Fock operator  $F_{\mu v}$  has the elements

$$F_{\mu v} = H_{\mu v}^{core} + \underbrace{\sum_{\lambda} \sum_{\sigma} P_{\lambda \sigma} \left[ (\mu v | \lambda \sigma) - \frac{1}{2} (\mu \lambda | v \sigma) \right]}_{G_{\mu v}} \quad (3.7)$$

<sup>1</sup> This concept follows the Pauli exclusion, a most important principle, that no two electrons in an atom can have the same values for all four Quantum numbers.

<sup>2</sup> the UHF method is normally used for unpaired electron systems. If  $c_{\mu i}^\alpha = c_{\mu i}^\beta$  for all doubly occupied orbitals, the method is called the restricted open-shell HF (ROHF). It is clear that ROHF always gives higher energy than UHF, but has an advantage of being faster and solving the problem of spin contamination in UHF.

where the first term is the core-hamiltonian matrix element

$$H_{\mu\nu}^{core} = \int \phi_{\mu} \hat{H}^{core} \phi_{\nu} d\tau \quad (3.8)$$

These elements of the core-Hamiltonian matrix are integrals involving the one-electron operator  $\hat{H}^{core}$  describing the electronic kinetic energy and nuclear-electron Coulomb attraction.

The overlap matrix  $S$  has elements

$$S_{\mu\nu} = \int \phi_{\mu} \phi_{\nu} d\tau. \quad (3.9)$$

The second term of Eq. 3.7 is the two-electron part  $G_{\mu\nu}$  which depends on the density matrix  $P$  with the elements for closed shell systems,

$$P_{\lambda\sigma} = 2 \sum_{i=1}^{occ} c_{\lambda i}^* c_{\sigma i} \quad (3.10)$$

and a set of two-electron integrals, describing the electron-electron interaction:

$$(\mu\nu | \lambda\sigma) = \left\langle \phi_{\mu}(1) \phi_{\nu}(1) \left| \frac{1}{r_{12}} \right| \phi_{\lambda}(2) \phi_{\sigma}(2) \right\rangle. \quad (3.11)$$

Due to their large numbers, the evaluation and manipulation of these two-electron integrals is one of the major time-consuming procedures in a Hartree-Fock calculation.

The electronic energy,  $E^{ee}$ , is now given by

$$E^{ee} = \frac{1}{2} \sum_{\mu=1}^N \sum_{\nu=1}^N P_{\mu\nu} (F_{\mu\nu} + H_{\mu\nu}^{core}). \quad (3.12)$$

### The self-consistent field (SCF) procedure

After specifying a molecule (a set of nuclear coordinates, atomic numbers, multiplicity, and number of electrons) and a basis set  $\phi_{\mu}$ , all required molecular integrals, i.e.  $S_{\mu\nu}$ ,  $H_{\mu\nu}^{core}$  and  $(\mu\nu | \lambda\sigma)$  are calculated. The iterative procedure begins by guessing a reasonable set of linear expansion coefficients  $c_{\mu i}$  and generating the corresponding density  $P_{\mu\nu}$ . A first Fock matrix is then calculated from  $H_{\mu\nu}^{core}$  and the two-electron part  $G_{\mu\nu}$ . Upon diagonalization a new matrix  $c$  is obtained. The whole process is repeated until the difference between the coefficients become insignificant for the resulting total energy. The solution is then said to be self-consistent and the method is thus referred to as the self-consistent-field (SCF) method.

### Basis set

As mentioned above, the molecular orbitals are synthesized as linear combinations of atomic orbitals (LCAO). It is apparent that different choices of basis sets produce different SCF wave functions and energies. The accuracy of the results should improve according to the choice of larger basis sets. We distinguish three types of basis sets commonly used:

- **Minimal basis sets:** one basis function per electron.
- **Extended basis set:** several basis functions per electron, adding sometimes polarization functions of higher type ( $p$  for H,  $d$ - and  $f$ -type for C, N, O, etc.).
- **Valence basis set:** the orbitals of the valence shell of each atom in the system are taken into account.

Two types of the basis set have come to dominate the area of *ab initio* molecular calculations, the Slater type orbital (STO) and Gaussian type orbital (GTO). The STO basis sets are rather of historic interest nowadays. Gaussian functions consist of an exponential of the form  $\exp(-\alpha r^2)$  with additional angular part for GTO's where  $\alpha$  is the gaussian exponent and  $r$  is the distance from the center of the function, while the STO basis includes  $r^{n-1}\exp(-\alpha r)$  plus the angular part where  $n$  defines the principal quantum number. The many integrals encountered in calculating with STO functions are extremely time consuming to evaluate and due to only numerical solution possibility, rather inaccurate for larger systems. This problem has led to the common use of the alternative GTO basis sets.

**The 6-31G\*, 6-31+G\*, and LanL2DZ basis sets.** In the 6-31G\* basis (sometimes denoted as 6-31G(d)) [75, 76], the  $1s$  AO of the first and second rows element is represented by the fixed combination of 6 GTOs, the  $2s$  ( $2p_x$  etc.) are approximated by a fixed combination of 3 GTOs and the extra valence orbitals  $2s'$  ( $2p'_x$  etc.) are just one GTO plus  $d$ -functions for the first row atoms. The 6-31+G\* designates the 6-31G\* basis set supplemented by the diffuse function. For heavy atoms with very large nuclei, electrons near the nucleus are treated in an approximate way, via effective core potentials (ECPs). One pseudopotential basis set has been used: the Los Alamos National Laboratory second Double-Zeta (LanL2DZ) basis set [77, 78, 79, 80] with effective core potentials. The double-zeta basis set consists of two basis functions per atomic orbital, and is thus twice as large as the minimal.

## 3.1.2 Configuration Interaction (CI) approach

### General Method

In *ab initio* quantum chemistry, the exact level energy  $E(\text{exact})$  is given by

$$E(\text{exact}) = E(\text{HF}) + E(\text{corr}) \quad (3.13)$$

where  $E(\text{HF})$  and  $E(\text{corr})$  represent the Hartree-Fock and correlated contributions, respectively.

Nevertheless, this formula shows the relationship between the 'experimental' or exact value and various HF energies. Because in HF calculations electrons are assumed to move in an average potential, the best HF calculation that could possibly be made (i.e. the HF limit) would still give an energy higher than the true one.

Thus, we attempt to use CI calculations to improve the ground state wave function by mixing in single, double, ... substitutions. A general multi-determinant wave function can

then be written as a linear combination of all contributions through various levels of excitation

$$\Psi = a_0\Psi_0 + \sum_i \sum_a^{occ\ vir} a_i^a \Psi_i^a + \sum_{i<j} \sum_{a<b}^{occ\ vir} a_{ij}^{ab} \Psi_{ij}^{ab} + \dots \quad (3.14)$$

Within the spirit of the variation principle, it will be possible to improve wave functions by solving the matrix eigenvalue problem, to find the best values of the  $a_0, a_i^a, a_{ij}^{ab}, \dots$  coefficients. A solution with lower energy will give us a better description of the electronic ground state.

### Comparison of Hartree-Fock and Configuration Interaction

The main differences between the HF and CI approaches can be deduced as follows:

- CI evaluates the correlation energy beyond the HF level.
- CI scales as  $N^6$ , while HF method scales as  $N^4$  (where  $N$  is the number of basis functions employed).
- CI strongly depends on the choice of the basis set.
- CI is not size consistent.

### CI-Singles

The excited-state wave function is written as a linear combination of all possible singly excited determinants, which leads us to the CIS (configuration interaction singles) method:

$$\Psi_{CIS} = a_0\Psi_0 + \sum_i \sum_a^{occ\ vir} a_i^a \Psi_i^a. \quad (3.15)$$

These CI coefficients can be deduced as normalized eigenvectors of the Hamiltonian matrix,

$$\langle \Psi_{ia} | H | \Psi_{jb} \rangle = [E_{HF} + \varepsilon_a - \varepsilon_i] \delta_{ij} \delta_{ab} - (ja || ib). \quad (3.16)$$

Here,  $\varepsilon$  represents the one-electron energy of an orbital and  $(ja || ib)$  are the usual two-electron integrals, transformed to the MO basis. The eigenvalues of this matrix are the CIS total energies for various excited states. This opens the possibility of studying the excitation of molecules much larger than can be treated by the other methods such as complete active space multiconfiguration SCF (MC-SCF), since they involve the evaluation of more complicated matrix elements than above.

Because of its importance in calculating accurate one-electron properties, the generalized CIS density matrix deserves a bit more attention. It is a sum of HF and excited state terms:

$$P_{\mu\nu}^{CIS} = P_{\mu\nu}^{HF} + P_{\mu\nu}^{\Delta}. \quad (3.17)$$

Now, we have introduced  $P^\Delta$ , the CIS delta density matrix. This can be a so-called ‘difference density matrix’, since it represents the changes in the electronic distribution upon the excitation.

The prediction of oscillator strength  $f$  for the excitation requires the calculation of the transition matrix element

$$f = \frac{2}{3} \Delta E \langle \Psi_{gs} | \hat{d} | \Psi_{es} \rangle^2 \quad (3.18)$$

where  $\Psi_{gs}$  and  $\Psi_{es}$  represent the wave function of ground state and excited state, respectively.  $\hat{d}$  and  $\Delta E$  are the transition dipole moment operator and the transition energy.

In general, the CIS wave function does not present an improvement over the HF wave function, since this approach also neglects correlation effects due to double and higher excitations.

The CIS calculation can be improved by the inclusion of some effects of electronic correlation via second order Møller-Plesset perturbation theory,

$$\begin{aligned} \Delta E_{CIS-MP2} = & -\frac{1}{4} \sum_{i<j}^{occ} \sum_{a<b}^{vir} \frac{\langle \Psi_{CIS} | H | \Psi_{ij}^{ab} \rangle^2}{\epsilon_a + \epsilon_b - \epsilon_i - \epsilon_j - \Delta_{CIS}} - \\ & \frac{1}{36} \sum_{i<j<k}^{occ} \sum_{a<b<c}^{vir} \frac{\langle \Psi_{CIS} | H | \Psi_{ijk}^{abc} \rangle^2}{\epsilon_a + \epsilon_b + \epsilon_c - \epsilon_i - \epsilon_j - \epsilon_k - \Delta_{CIS}} \end{aligned} \quad (3.19)$$

where  $\Delta_{CIS}$  is the difference between the CIS excitation and ground-state energies. The  $\Delta E_{CIS-MP2}$  can be added to  $E_{CIS}$  to define  $E_{CIS-MP2}$  for an excited state. The corresponding eigenvalues are the orbital energies  $\epsilon_1, \dots, \epsilon_n$  involving the labels  $i, j, k, \dots$  for occupied spin orbitals and labels  $a, b, c, \dots$  for virtual spin orbitals.

## CID and CISD

The inclusion of only doubly excited configurations leads to the CID (the configuration interaction approach with all double substitutions) method,

$$\Psi_{CID} = a_0 \Psi_0 + \sum_{i<j}^{occ} \sum_{a<b}^{vir} a_{ij}^{ab} \Psi_{ij}^{ab}. \quad (3.20)$$

When both single and double virtual excitations are included, the CISD (the configuration interaction approach with all single and double substitutions) wave function is obtained as

$$\Psi_{CISD} = a_0 \Psi_0 + \sum_i^{occ} \sum_a^{vir} a_i^a \Psi_i^a + \sum_{i<j}^{occ} \sum_{a<b}^{vir} a_{ij}^{ab} \Psi_{ij}^{ab}. \quad (3.21)$$

Although CID and CISD are well-defined models, given a standard basis set, they suffer some serious disadvantages. These have to do with size consistency. If a method such as CID is applied to a pair of completely separated system, the resulting energy is not the sum of the energies obtained by applying the same theory to the systems separately [81].

### Quadratic Configuration Interaction (QCI) approach

Our main method, the QCISD(T) (the quadratic configuration interaction approach including single, double, and triple substitutions) approach, accounts for correlations almost fully and possesses a large number of advantages compared to lower order CI calculations such as CIS, CID, and CISD. This method was established by Pople *et al.* [33] in 1987 and since that time has successfully been applied to a variety of systems. In the case of simple molecules a comparison with a full CI calculation is possible and shows good agreement. The results for larger systems including metal oxide clusters are presented in the literature as well (such as Ref. [82]). The scaling of the QCISD method with  $N^6$  (where  $N$  is the number of basis functions in the system) is comparable with the coupled cluster (CC) approach of the same level (i.e. CCSD) [83]. QCISD and QCISD(T) are similar to CCSD and CCSD(T), respectively, but some of the terms in CC have been omitted in QCI. The CC method is originally introduced into quantum chemistry by Cizek [84] and incorporated into Gaussian code [85, 86].

This method expresses the wave function in a fundamental equation

$$\Psi = e^T \Psi_0 \quad (3.22)$$

where  $\Psi$  is the exact nonrelativistic ground state wave function,  $\Psi_0$  is the normalized ground state HF wave function, and the operator  $e^T$  is defined by the Taylor-series expansion. The single excitation operator  $T_1$  and the double excitation operator  $T_2$  are

$$T_1 = \sum_i^{occ} \sum_a^{vir} a_i^a \hat{t}_i^a \quad (3.23)$$

and

$$T_2 = \frac{1}{4} \sum_{i < j}^{occ} \sum_{a < b}^{vir} a_{ij}^{ab} \hat{t}_{ij}^{ab}. \quad (3.24)$$

where  $\hat{t}_i^a$ ,  $\hat{t}_{ij}^{ab}$ , ... are elementary substitution operators and the arrays  $a_i^a$ ,  $a_{ij}^{ab}$ , ... involve coefficients to be determined. Various types of antisymmetric wave functions can be obtained by applying various functions of the  $T$  operators to  $\Psi_0$ ,

$$\Psi = f(T_1, T_2, \dots) \Psi_0 \quad (3.25)$$

and then determining the coefficients  $a$  by an appropriate projection of the Schrödinger function  $(H - E)\Psi$ , where  $H$  is the full Hamiltonian, and  $E$  the total energy.

Thus

$$\langle \Psi_0 | H - E | \Psi \rangle = 0, \quad (3.26)$$

$$\langle \Psi_i^a | H - E | \Psi \rangle = 0, \quad (3.27)$$

$$\langle \Psi_{ij}^{ab} | H - E | \Psi \rangle = 0, \quad (3.28)$$

where  $\Psi_i^a$  is the singly substituted determinant  $\hat{t}_i^a \Psi_0$  and so forth.

For example, the CISD wave function is written in the form

$$\Psi_{CISD} = (1 + T_1 + T_2) \Psi_0. \quad (3.29)$$

If we define

$$H = F + V, \quad (3.30)$$

$$E_{HF} = \langle \Psi_0 | H | \Psi_0 \rangle, \quad (3.31)$$

$$E = E_{HF} + E_{corr.}, \quad (3.32)$$

$$\bar{H} = H - E_{HF}, \quad (3.33)$$

$$\bar{V} = V - \langle \Psi_0 | V | \Psi_0 \rangle, \quad (3.34)$$

where  $F$  is the Fock Hamiltonian (Eq. 3.7), then the CISD projection equations can be written

$$\langle \Psi_0 | H | T_2 \Psi_0 \rangle = E_{corr.}, \quad (3.35)$$

$$\langle \Psi_i^a | \bar{H} | (T_1 + T_2) \Psi_0 \rangle = a_i^a E_{corr.}, \quad (3.36)$$

$$\langle \Psi_{ij}^{ab} | \bar{H} | (1 + T_1 + T_2) \Psi_0 \rangle = a_{ij}^{ab} E_{corr.} \quad (3.37)$$

In deriving these equations from the projection conditions eq.(3.26) to (3.28), we have replaced  $\langle \Psi_i^a | H | \Psi_0 \rangle = 0$  by zero for all  $i, a$ . This is because  $\Psi_0$  is the optimized Hartree-Fock function (Brillouin's theorem) [33].

An approximation of the effects of triple substitution is available through the QCISD(T), where three particle excitations are included by means of fourth order perturbation theory (MP4) [87, 86].

The contribution of triple substitutions ( $ijk \rightarrow abc$ ) to the fourth order correlation energy is evaluated as

$$\Delta E_T^{(4)} = -\frac{1}{36} \sum_{ijk}^{occ} \sum_{abc}^{vir} (\epsilon_a + \epsilon_b + \epsilon_c - \epsilon_i - \epsilon_j - \epsilon_k)^{-1} |w_{ijk}^{abc}|^2 \quad (3.38)$$

where  $w_{ijk}^{abc}$  is the matrix element of perturbation operator (it can be expressed via  $a_{ij}^{ab}$  as in the Eq. 3.21 and electron repulsion integrals as defined in Eq. 3.11).

In fact, the QCISD and CCSD methods have the further advantage of being completely correct for composite two-electron systems by adding a minimum number of terms to the CI level to make it size consistent ( $E_{AB}(r_{AB} \rightarrow \infty) = E_A + E_B$ ).

### The Møller-Plesset perturbation theory

We mentioned before that perturbation theory could be used to study the effects of electron correlation. Basically, the Møller-Plesset (MP) method [88] adds corrections to a zeroth-order Hamiltonian ( $\hat{H}_0$ ) by introducing a generalized electronic Hamiltonian,  $\hat{H}(\lambda)$ , according to

$$\hat{H}(\lambda) = \hat{H}_0 + \lambda \hat{V}, \quad (3.39)$$

where  $\lambda$  is some parameter and  $\lambda\hat{V}$  (or  $\hat{H}^{(1)}$ ) is a small perturbed correction applied to the unperturbed system such as HF or CI.

Then, one can express an exact or full CI wave function as a power series expansion that may be truncated as desired, viz

$$\Psi_k = \Psi_k^{(0)} + \lambda_1 \Psi_k^{(1)} + \lambda_2 \Psi_k^{(2)} + \lambda_3 \Psi_k^{(3)} + \dots \quad (3.40)$$

For instance, MP2 is truncated after the second order term and so on. The aim of perturbation theory is to seek expansions of the energy  $E$ :

$$E_k = E_k^{(0)} + \lambda_1 E_k^{(1)} + \lambda_2 E_k^{(2)} + \lambda_3 E_k^{(3)} + \dots \quad (3.41)$$

where  $E^{(1)}$  is the first-order correction to  $E$ , etc. A special case is the Rayleigh-Schrödinger method which gives  $\Psi_k^{(0)}$  as the state of interest in the absence of the perturbation.

Then, one obtains:

$$E_k^{(1)} = \int \Psi_k^{(0)} \hat{H}^{(1)} \Psi_k^{(0)} d\tau \quad (3.42)$$

$$E_k^{(2)} = - \sum_{m \neq k} \frac{\left( \int \Psi_k^{(0)} \hat{H}^{(1)} \Psi_m^{(0)} d\tau \right)^2}{E_m - E_k} \quad (3.43)$$

with corresponding results for  $\Psi^{(1)}$  and  $\Psi^{(2)}$ , etc.

### 3.1.3 Spin-orbit coupling

The atomic Hamiltonian does not involve electron spin. In reality, the existence of spin adds an additional term (usually small) to the Hamiltonian. This term, called the spin-orbit interaction, breaks spin rotation invariance and thus lifts the degeneracy of atomic levels (fine structure splitting). Spin-orbit interaction is a relativistic effect and is properly derived using Dirac's relativistic treatment of the electron as

$$H_{SO} = \xi(r) l \cdot s, \quad (3.44)$$

where  $\xi(r)$  is

$$-\frac{e\hbar^2}{2m^2c^2} \frac{1}{r} \frac{dU(r)}{dr} \quad (3.45)$$

with a spherically symmetric potential  $U(r)$  for the electron. Classically, this interaction may be viewed as the interaction of the magnetic moment of an electron spin with the magnetic field induced by the motion of the nucleus around the electron. The nucleus is seen from the coordinate system fixed on the electron.

For relativistic quantum chemical methods, analytical spin-orbit interaction are now routinely available for HF, MC-SCF, and CI wave functions. Additionally, the inclusion of spin-orbit coupling has been successfully implemented with Møller-Plesset perturbation theory as well as within the CC method. As mentioned, relativistic effects can be characterized by a

variety of ways. Here, for the underlying theory of spin-orbit coupling effects we refer to the literature [89, 90].

In recent years, Pitzer *et al.* [89] have proposed a new technique for calculating the spin-orbit interaction energy by means of Spin-Orbit Configuration Interaction. This method is obtained by the GUGA in combination with relativistic core potential and spin-orbit operators, thus providing an efficient way for treating the electronic structure of molecules containing heavy atoms. The development of the spin-orbit matrix elements and the implementation of these methods in the COLUMBUS [91, 92, 93, 94] suite of programs are described.

The relativistic effective core potential (RECP) represents, for the valence electrons, the repulsion of the core electrons, the spin-orbit interaction with the nucleus, the spin-orbit interaction with the core electrons, and an approximation to the spin-orbit interaction between the valence electrons [95], especially for heavier element systems.

The potentials obtained directly from relativistic atomic wave functions have the form

$$U^{REP} = \sum_{l=0}^{\infty} \sum_{j=|l-1/2|}^{|l+1/2|} U_{lj}^{REP}(r) \hat{O}_{lj}, \quad (3.46)$$

where REP denotes the relativistic effective potential, and  $\hat{O}_{lj}$  are (spin-dependent) projection operators as

$$\hat{O}_{lj} = \sum_{m=-j}^j |l jm\rangle \langle l jm|. \quad (3.47)$$

The REP operators can be expressed in a more readily usable form in terms of the spin-independent projection operators  $\hat{O}_l$

$$U^{REP} = \sum_{l=0}^{\infty} U_l^{AREP}(r) \hat{O}_l + \sum_{l=1}^{\infty} \xi_l(r) \hat{l} \cdot \hat{s} \hat{O}_l = U^{AREP} + h^{SO} \quad (3.48)$$

where  $U_l^{AREP}(r)$  is an averaged relativistic effective potential and  $\xi_l(r)$  depends on the difference of  $U_{l,l+1/2}(r)$  and  $U_{l,l-1/2}(r)$ . These two terms are readily identified [96, 97] as core potentials and spin-orbit operators, respectively. The  $U_l^{AREP}(r)$  are approximately independent of  $l$  when  $l \geq L$ , where  $L$  is one larger than the largest  $l$  value of the core electrons. Then  $U^{AREP}$  and  $h^{SO}$  can be reduced to

$$U^{AREP} = U_L^{AREP}(r) + \sum_{l=0}^{L-1} \left( U_l^{AREP}(r) - U_L^{AREP}(r) \right) \hat{O}_l \quad (3.49)$$

$$h^{SO} = \sum_{l=1}^L \xi_l(r) \hat{l} \cdot \hat{s} \hat{O}_l. \quad (3.50)$$

With these forms, existing programs for nonrelativistic calculations can be adapted to include relativistic effects. The additional integrals of  $U^{AREP}$  and  $h^{SO}$  are included in the COLUMBUS programs.

By using the RECP approximation in order to include the spin-orbit interaction, the total Hamiltonian is

$$H_{total} = H_0 + H_{SO} \quad (3.51)$$

where the atomic Hamiltonian  $H_0$  is given by

$$H_0 = \sum_{\mu=1}^N h(\mu) + \frac{1}{2} \sum_{\mu \neq \nu} v(\mu, \nu) \quad (3.52)$$

and  $H_{SO}$  is given by

$$H_{SO} = \sum_{\mu=1}^N h^{SO}(\mu). \quad (3.53)$$

The Hamiltonian can be written as

$$H_{total} = \sum_{i,j} h_{ij} E_{ij} + \frac{1}{2} \sum_{i,j,k,l} [ij;kl] e_{ij,kl} + \sum_{ij} \sum_{\sigma\tau} h_{i\sigma,j\tau}^{SO} E_{i\sigma,j\tau}. \quad (3.54)$$

## 3.2 Method implementation

### 3.2.1 *Ab initio* embedded cluster method

The smallest suitable cluster to simulate bulk NiO consists of one  $\text{Ni}^{2+}$  ion and six nearest-neighbour  $\text{O}^{2-}$  ions forming a cubic crystallographic arrangement with  $O_h$  group, [98]  $(\text{NiO}_6)^{10-}$ . In contrast, the NiO(001) surface has  $C_{4v}$  symmetry (considering five-fold crystal field state), therefore we use a  $(\text{NiO}_5)^{8-}$  cluster. The isolated cluster and embedded cluster models for the NiO(001) surface are illustrated in Fig. 3.1. The length of the nickel-oxygen bond has been fixed at 2.0842 Å according to experimental data [99]. This measured value has been commonly used for theoretical models in the unrelaxed case. In order to be able to treat materials with larger surface relaxation the geometry of the cluster should be optimized. For the geometry optimization on the QCISD level, one must have a possibility to compute forces on the same level of theory. Schemes that evaluate the gradient of generic CI energies have been available for several years [100, 101]. Computation of the forces for the simplest CIS method is described in Ref. [31]. Formulae for the analytical evaluation of energy gradients in quadratic configuration interaction theory, such as QCISD are derived in Ref. [87].

For the relaxed case, we would therefore not expect very strong effects since the (001) surface of NiO is nonpolar and the most stable geometry is quite close to the truncated bulk one. An experiment [102] showed that surface relaxations are 0% – 4% for the first spacing and -4% – 4% for the first-layer buckling. This supports our choice of the unrelaxed geometry. Moreover, the NiO(001) surface has been shown by low-energy electron diffraction (LEED) studied to be almost perfect bulk termination, with no rumpling and only a 2% relaxation of

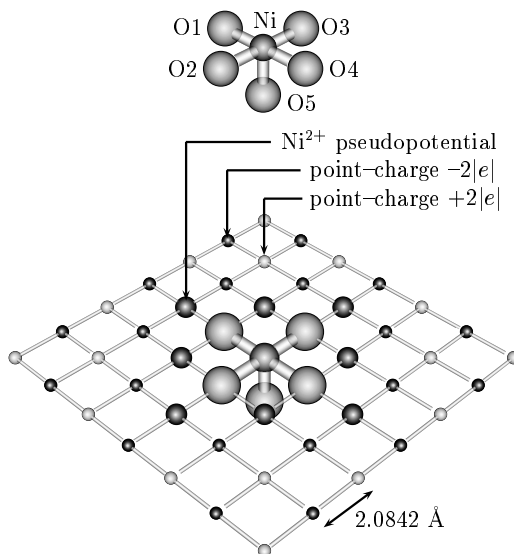


Fig. 3.1: The  $(\text{NiO}_5)^{8-}$  cluster and embedded cluster models of the NiO(001) surface (only the surface charges are shown).

the outer layer [103, 104]. In the case of  $\text{Fe}_2\text{O}_3$  or  $\text{Al}_2\text{O}_3$ , where surface relaxation may play a major role, a prior geometry optimization is necessary [105, 106, 107].

In order to correctly account for the electrostatic environment due to the rest of an ionic solid crystal, the simplest possible way is to embed the bare cluster in a set of point charges located at the lattice sites representing the Madelung potential in the environment. The point charges at the edges of the calculated slab are fractional [66]. In the vicinity of the quantum cluster, the point charges were exchanged by effective core potentials (ECPs) with charge +2; for that purpose we used magnesium cores  $1s^22s^22p^6$  deprived of 2 valence electrons in order to simulate  $\text{Ni}^{2+}$  ions. This allows for the proper description of the Pauli repulsion within the cluster and the nearest-neighbouring point charges and prevents a flow of electrons from  $\text{O}^{2-}$  ions to the positive charges [108, 109]. The structure of the NiO(001) surface was assumed fixed for long-range contributions of the semi-infinite Madelung potential ( $15 \times 15 \times 7$  ions), see Fig. 3.2. For the bulk system, our infinite Madelung potential was represented by  $15 \times 15 \times 15$  ions (Fig. 3.2).

For the ground state, we employ a single point calculation based on the unrestricted HF level of theory. As a basis set for the  $\text{Ni}^{2+}$  ion, we use the valence Los-Alamos basis plus double-zeta and effective core potentials (LanL2DZ ECP). The oxygen basis set was a 6-31G\* basis [110]. The first step of our excitation calculation is always the CIS calculation in order to estimate excitation spectrum, oscillator strength, and band gap. The basis sets used in these calculations are almost the same as for ground-state calculations, except that we add one diffuse function into the oxygen basis set (6-31+G\* basis) [111], which is necessary for the excited state calculation.

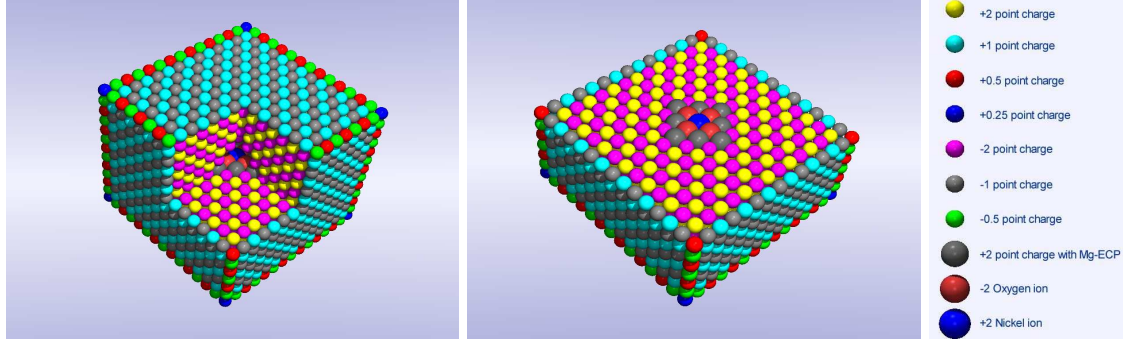


Fig. 3.2: The embedded  $(\text{NiO}_6)^{10-}$  and  $(\text{NiO}_5)^{8-}$  clusters modelling the bulk and (001) surface of NiO.

### 3.2.2 Improvements of electron correlation

This step is to study the electronic correlation effects on the low-lying excited states of NiO such as  $d-d$  transitions. At the correlated level of theory, the correlated increments, namely, CID, CISD, QCISD, and QCISD(T) were compared with CIS. We perform these calculations of five triplet states for  $d-d$  transitions:

$$\begin{aligned}
& {}^3B_1 ((d_{xz})^2, (d_{yz})^2, (d_{xy})^2, (d_{3z^2-r^2})^1, (d_{x^2-y^2})^1); \\
& {}^3E ((d_{xz})^1, (d_{yz})^2, (d_{xy})^2, (d_{3z^2-r^2})^2, (d_{x^2-y^2})^1) \\
& \text{and} \\
& (d_{xz})^2, (d_{yz})^1, (d_{xy})^2, (d_{3z^2-r^2})^2, (d_{x^2-y^2})^1); \\
& {}^3B_2 ((d_{xz})^2, (d_{yz})^2, (d_{xy})^1, (d_{3z^2-r^2})^1, (d_{x^2-y^2})^2); \\
& {}^3A_2 ((d_{xz})^2, (d_{yz})^2, (d_{xy})^1, (d_{3z^2-r^2})^2, (d_{x^2-y^2})^1); \\
& {}^3E ((d_{xz})^1, (d_{yz})^2, (d_{xy})^2, (d_{3z^2-r^2})^1, (d_{x^2-y^2})^2) \\
& \text{and} \\
& (d_{xz})^2, (d_{yz})^1, (d_{xy})^2, (d_{3z^2-r^2})^1, (d_{x^2-y^2})^2).
\end{aligned}$$

These methods allow us to take into account a part of the electronic correlation in both ground and excited states. All *ab initio* embedded calculations were done with the GAUSSIAN98 package [112].

### 3.2.3 Treatment of spin-orbit coupling

In order to investigate the low-lying excited states more fully, we consider the effect of spin-orbit coupling on these energy levels of the bulk NiO and NiO(001) surface using the spin-orbit configuration interaction approach of Yabushita *et al.* [89]

Since GAUSSIAN98 is not capable of predicting a property of spin-orbit coupling (except that MC-SCF approach is only available for spin-orbit coupling for elements through Chlorine where LS coupling is used), a different program such as COLUMBUS has been used in order to estimate this relativistic effect. Firstly, we consider the theory of the splitting of atomic energy levels in crystalline field with the symmetry including the effects of spin-orbit coupling, by

following a paper by Cracknell (1968) [113]. Then, we use the GUGA-CI programs in the COLUMBUS code for multi-reference singles and doubles CI calculations including the spin-orbit interaction in the RECP approximation [89]. The work in this part is divided into three main steps:

- We verify the triplet excited states without the spin-orbit interaction of the NiO(001) surface system during the CIS framework and compare these energies with results obtained from GAUSSIAN98.
- We determine the singlet excited states without spin-orbit interaction.
- We generate the triplet excited states including the spin-orbit interaction effect.

In order to analyze the symmetry of each levels of the ground and excited states, we first address a section of useful explanation how crystal field and spin-orbit splittings can be obtained from the unified point of view by decomposing the direct product of representations over the irreducible representations (in Section 4.4.1).

### 3.3 Nonlinear optical surface response

The electric polarization  $P$  can be expanded in terms of the electric field as

$$P = \chi^{(\omega)} E + \chi^{(2\omega)} E^2 + \chi^{(3\omega)} E^3 + \dots \quad (3.55)$$

where  $\chi^{(\omega)}$ ,  $\chi^{(2\omega)}$ ,  $\chi^{(3\omega)}$ , ... are tensors of the linear polarizability, the first order and the second order hyperpolarizabilities, respectively, and so on. In this work, we deal with  $\chi^{(2\omega)}$  representing a second-harmonic contribution. Within the ED approximation,  $\chi^{(2\omega)}$  vanishes for bulk NiO due to the inversion symmetry of the crystal, but it is allowed at the surface where inversion symmetry is broken. Thus, in the electric-dipole approximation, SHG is an ideal probe of the surface  $d$ - $d$  intragap transitions.

We consider an expression for the second order polarization

$$P_i = \chi_{ijk}^{(2\omega)} E_j E_k, \quad (3.56)$$

where

$$\chi_{ijk}^{(2\omega)}(\omega) = \frac{\rho_0}{\epsilon_0} \sum_{\alpha\beta\gamma} \left[ \langle \gamma | d_i | \alpha \rangle \overline{\langle \alpha | d_j | \beta \rangle} \overline{\langle \beta | d_k | \gamma \rangle} \times \frac{f(E_\gamma) - f(E_\beta)}{E_\gamma - E_\beta - \hbar\omega + i\hbar\delta} - \frac{f(E_\beta) - f(E_\alpha)}{E_\beta - E_\alpha - \hbar\omega + i\hbar\delta} \right] \frac{1}{E_\gamma - E_\alpha - 2\hbar\omega + 2i\hbar\delta}, \{i, j, k\} \in \{x, y, z\} \quad (3.57)$$

is the second-harmonic susceptibility tensor. It is derived from the second order perturbation theory for the density matrix and the details are given in Ref. [34]. In this formula  $f$  is the Fermi distribution, which is unity for the ground state, and vanishes otherwise.  $\rho_0$  is the

unperturbed electron density and  $\langle \alpha | d_{i,j,k} | \beta \rangle$  are the matrix elements of the dipole moment  $d = (d_x, d_y, d_z)$ . The overline denotes the symmetrization needed to fulfill the symmetry upon interchanging the two incident photons. The transition dipole matrix elements over two Slater determinants are computed according to

$$\begin{aligned} \langle \alpha | d | \beta \rangle &= \left\langle \frac{1}{\sqrt{n!}} | \chi_1^\alpha \chi_2^\alpha \cdots \chi_i^\alpha \cdots \chi_n^\alpha | d | \frac{1}{\sqrt{n!}} | \chi_1^\beta \chi_2^\beta \cdots \chi_i^\beta \cdots \chi_n^\beta \rangle \right. \\ &= \sum_{i,j=1}^n (-1)^{i+j} \langle \chi_i^\alpha | d | \chi_j^\beta \rangle M_{ij}, \end{aligned} \quad (3.58)$$

where  $M_{ij}$  are the minors of the matrix composed of the overlaps between single-particle wave-functions

$$M = \begin{pmatrix} O_{11}^{\alpha\beta} & O_{12}^{\alpha\beta} & \cdots & O_{1n}^{\alpha\beta} \\ O_{21}^{\alpha\beta} & O_{22}^{\alpha\beta} & \cdots & O_{2n}^{\alpha\beta} \\ \vdots & \vdots & \cdots & \vdots \\ O_{n1}^{\alpha\beta} & O_{n2}^{\alpha\beta} & \cdots & O_{nn}^{\alpha\beta} \end{pmatrix}.$$

For the NiO(001) surface, the symmetry analysis gives the only nonvanishing tensor elements resulting from the crystallographic structure of an undistorted cubic lattice:

$$\chi_{ijk}^{(2\omega)} = \begin{pmatrix} 0 & 0 & 0 & 0 & \chi_{xxz}^{(2\omega)} & 0 \\ 0 & 0 & 0 & \chi_{yyz}^{(2\omega)} & 0 & 0 \\ \chi_{zxx}^{(2\omega)} & \chi_{zyy}^{(2\omega)} & \chi_{zzz}^{(2\omega)} & 0 & 0 & 0 \end{pmatrix}. \quad (3.59)$$

To calculate  $\chi^{(2\omega)}$  related to surface antiferromagnetism, we need spin-orbit coupling to be included in the wave function. This however is beyond the scope of this thesis and will be the subject of a forthcoming work.

Based on the SHG tensor we compute nonlinear optical properties of the system. The second-harmonic electrical-field projection on the optical plane of the analyzer is given in the short form notation [114] by:

$$\begin{aligned} E(2\omega; \Theta, \Phi, \varphi) &= 2i\delta z \frac{\omega}{c} |E_0^{(\omega)}|^2 \begin{pmatrix} A_p F_c \cos \Phi \\ A_s \sin \Phi \\ A_p N^2 F_s \cos \Phi \end{pmatrix}^T \\ &\quad \left( \begin{array}{ccc|ccc} \cdot & \cdot & \cdot & \cdot & \cdot & \cdot \\ \cdot & \chi_{ijj}^{(2\omega)} & \cdot & \cdot & \chi_{ijk}^{(2\omega)} & \cdot \\ \cdot & \cdot & \cdot & \cdot & j \neq k & \cdot \end{array} \right) \cdot \begin{pmatrix} f_c^2 t_p^2 \cos^2 \varphi \\ t_s^2 \sin^2 \varphi \\ f_s^2 t_p^2 \cos^2 \varphi \\ 2f_s t_p t_s \cos \varphi \sin \varphi \\ 2f_c f_s t_p^2 \cos^2 \varphi \\ 2f_c t_p t_s \cos \varphi \sin \varphi \end{pmatrix} \end{aligned} \quad (3.60)$$

where  $\Theta$ ,  $\Phi$  and  $\varphi$  are the angle of incidence, polarization of the incident photon and polarization of the output photon, respectively. The nonlinear response depends as well on the

optical properties of the system. Introducing notations for the frequency dependent refraction index of the material  $n = \sqrt{\epsilon(\omega)}$  and  $N = \sqrt{\epsilon(2\omega)}$  the other parameters can be expressed as  $f_s = \frac{\sin\Theta}{n}$ ,  $f_c = \sqrt{1 - f_s^2}$  — projections of the wave vector in the system,  $t_p = \frac{2\cos\Theta}{n\cos\Theta + f_c}$  and  $t_s = \frac{2\cos\Theta}{\cos\Theta + nf_c}$  — linear transmission coefficients, and  $A_p = \frac{2\pi T_p}{\cos\Theta}$  and  $A_s = \frac{2\pi T_s}{\cos\Theta}$  — transmission field amplitudes.  $\delta z$  means the thickness of the system (in our case equal to a lattice constant of 4.1684 Å).

The intensity of the SHG response can then be obtained from:

$$I(2\omega; \Theta, \Phi, \varphi) = \epsilon_0 c |E(2\omega; \Theta, \Phi, \varphi)|^2. \quad (3.61)$$

Using the many-body wave functions and energies resulting from CID and QCISD(T) calculations, we compute the SHG tensor for the NiO(001) surface. In contrast to bulk NiO, where the SHG response is forbidden within the ED approximation because of the inversion symmetry, the  $C_{4v}$  symmetry of the surface leads to five non-zero tensor elements. From that the intensity of the non-linear optical response as a function of photon energy at different polarizations of the incident and outgoing photons is obtained. This quantity can be directly measured in experiment, and we suggest possible conditions in order to detect it.

# Chapter 4

## Results and Discussion

### 4.1 Ground state properties

First, we consider the ground-state electronic structure of an embedded cluster modelled as a  $15 \times 15 \times 7$  (seven layers deep) point-charge lattice of the NiO(001) surface. The  $3d^8$  configuration at the NiO(001) surface has the  ${}^3B_1$  electronic state as its ground state  $[(d_{xz})^2, (d_{yz})^2, (d_{xy})^2, (d_{3z^2-r^2})^1, (d_{x^2-y^2})^1]$ . In a  $C_{4v}$  symmetry, there are four different energy levels, related to the degenerate  $d_{xz}(d_{yz})$  orbitals, the  $d_{xy}$  orbital, the  $d_{3z^2-r^2}$  orbital, and the  $d_{x^2-y^2}$  orbital, respectively. More insight in the electronic structure is obtained from the calculated density of states (DOS) of the ground state following Mulliken population analysis, which is shown in Fig. 4.1. For the description of the DOS, two different sets of orbitals are assigned to the two spins based on an UHF calculation.

Figure 4.1 (a) shows the calculated DOS of the majority spin of the ground state. The lower and upper valence bands predominantly exhibit Ni(3d) and O(2p) characters, respectively. There are altogether 15 electron states between  $-11.97$  and  $-8.16$  eV and 5 states between  $-17.14$  and  $-15.51$  eV which correspond to  $2p$  and  $3d$  orbitals, respectively, of the  $O^{2-}$  and  $Ni^{2+}$  ions in the embedded  $(NiO_5)^{8-}$  cluster. Some of these states are degenerate. The main character of the localized  $3d$  orbitals consists of four electronic states such as  $d_{x^2-y^2}$ ,  $d_{3z^2-r^2}$ ,  $d_{xz}(d_{yz})$  and  $d_{xy}$  splitting from the triple degenerate of  $e_g$  and  $t_{2g}$  states in the cubic  $O_h$  symmetry, respectively. The valence band has O(2p) states at the upper edge leading to a charge-transfer gap in our study. The four lowest unoccupied orbitals are the 4s and 4p orbitals of the  $Ni^{2+}$  ion.

The DOS of the minority spins is given in Fig. 4.1 (b). The valence band consists of the O(2p) states in the energy range  $(-11.70, -8.98)$  eV. The latter comprise the  $d_{xy}$  orbital (about  $-13.69$  eV) and the degenerate  $d_{xz}(d_{yz})$  orbitals at an energy of  $-13.66$  eV. The lower edge of the conduction bands also consists of the 4s and 4p orbitals. The vicinity of the unoccupied Ni(4s, 4p) orbitals is mainly of Ni-3d character in an  $e_g$  level ( $d_{3z^2-r^2}$  and  $d_{x^2-y^2}$ ).

The detailed Mulliken procedure for this embedded cluster also shows the net atomic charge and spin values, see Table 4.1. Note, the atomic labels in Table 4.1 are given in Fig. 3.1. According to this Mulliken population analysis, the Ni and O atoms are not fully ionized, and have explicit charges of  $+1.1$  and  $-1.8$ , respectively. The net atomic spin resulting from our

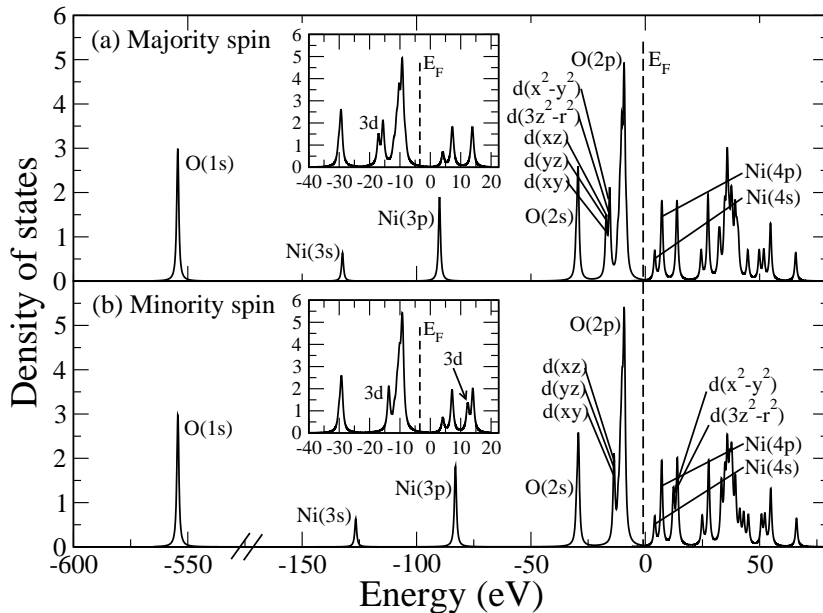


Fig. 4.1: Density of states broadened by a Lorentzian with the full width at half maximum (FWHM) of 0.5 eV.

embedded cluster calculation is similar to the data obtained by Towler *et al.* [115] employing a different approach.

This work			Ref. [115]		
Atom	$q$	$\delta n_s$	Magnetic configuration	$\delta n_s(\text{Ni})$	$\delta n_s(\text{O})$
Ni	1.1172	1.8922	NiO(AF <sub>2</sub> )	1.923	0.000
O1-O4	-1.8119	0.0208	NiO(AF <sub>1</sub> )	1.934	0.024
O5	-1.8697	0.0248	NiO(FM)	1.931	0.069

Tab. 4.1: Calculated net atomic charges ( $q$ ) and net atomic spin ( $\delta n_s$ ) carried out by Mulliken population analysis. The results of Ref. [115] for true antiferromagnetic type II (AF<sub>2</sub>) and hypothetical ferromagnetic (FM) and antiferromagnetic type I (AF<sub>1</sub>) configurations of NiO are given for comparison of the spin density distributions.

## 4.2 Excited states and optical properties

### 4.2.1 Madelung field effects

We performed calculations for the ‘slab’ of three sizes, namely  $7 \times 7 \times 3$  ions,  $11 \times 11 \times 5$  ions, and  $15 \times 15 \times 7$  ions of the NiO conventional crystal cells (note that these are defined in terms of  $3 \times 3 \times 1$ ,  $5 \times 5 \times 2$ , and  $7 \times 7 \times 3$  unit cells). For the largest crystal size used in our

calculations, the total Madelung potential is represented by 1556 ( $15 \times 15 \times 7 - 6 - 13$ ) point charges. These various sizes of slabs were chosen to check for size-related effect, to ensure reproducibility of the results and to assess the effect of electrostatic potentials.

By convention, three optical-gap energies of the bare  $(\text{NiO}_5)^{8-}$  embedding in the various Madelung field sizes were compared. These results are presented in Table 4.2. In the first row of Table 4.2, we can estimate the relative performance of these results. The larger environmental crystal size can reduce the gap energy. One can see that the gap energy does not change from the medium size to the largest size. From this we conclude that the size of our largest model to take into account the long range contribution of electrostatic potential of the NiO crystal is large enough as to yield sufficiently accurate results.

Spin	Embedded cluster size		
	$7 \times 7 \times 3$	$11 \times 11 \times 5$	$15 \times 15 \times 7$
majority spin	7.99	7.58	7.58
minority spin	8.73	8.33	8.33

Tab. 4.2: Calculated optical gap energy (eV) on NiO(001) for spin-up (majority) and spin-down (minority). Results for increasing sizes of the embedded cluster models with dimension  $n \times n \times m$  (m layers deep) are indicated.

### 4.2.2 CIS results and optical properties

In this section we discuss the ability of the CIS technique to reproduce experimental excitation energies. NiO is a complicated system for understanding excited states. It also serves as an excellent example to show the strengths, weaknesses, and pitfalls of CIS calculations. Because of the high symmetry of the crystal, care must be exercised in producing initial guess vectors for the configuration interaction procedure. All symmetry types must be present for the systematic search of the lowest excited states. In comparing results to experimental data, one must be aware of the existence of symmetry-forbidden states as well as diffuse states observed in optical spectra.

Table 4.3 contains the calculated CIS vertical excitation energies and oscillator strengths  $f$  for the first 20 excited states. In the Table 4.3, let's consider the properties of the seventh entry. The transition energy is calculated as 7.5765 eV = 163.64 nm. And,  $34A \rightarrow 35A$  ( $O(2p) \rightarrow Ni(4s)$ ) shows that the configuration resulting from an electron being excited from the 34A to 35A MO has a CI coefficient of 0.82059 and it has a dominance of 67.3% ( $= (0.82059)^2 * 100$ ). This is an example of an excited state expressed as a mixture of excited configurations. In general, the description of the excited state may require many excited configurations. Because of this, CI is also called the Configuration Mixing (CM) method. Note that, in GAUSSIAN98, if we want to determine the specific type of orbital transformation for a transition, we will need to examine the molecular orbitals for the largest components of the transition, indicated by the largest wave function coefficients. The 34A MO is the HOMO and the 35A MO is the LUMO (for the  $\alpha$  state). Thus, the tenth entry in the table represents the

State	Excitation energy		Main excited configurations			$f$
	eV	nm	MO	CI coef.	Config.	
1	0.5122	2420.69	17B $\rightarrow$ 37B	0.73301	${}^3B_1 \rightarrow {}^3E$	0.0000
2	0.5122	2420.69	16B $\rightarrow$ 37B	0.73301	${}^3B_1 \rightarrow {}^3E$	0.0000
3	0.9604	1291.01	15B $\rightarrow$ 38B	0.83926	${}^3B_1 \rightarrow {}^3B_2$	0.0000
4	1.9570	633.53	15B $\rightarrow$ 37B	0.74153	${}^3B_1 \rightarrow {}^3A_2$	0.0000
5	2.8638	432.94	17B $\rightarrow$ 38B	0.79161	${}^3B_1 \rightarrow {}^3E$	0.0000
6	2.8638	432.94	16B $\rightarrow$ 38B	0.79161	${}^3B_1 \rightarrow {}^3E$	0.0000
7	7.5765	163.64	34A $\rightarrow$ 35A	0.82059	${}^3B_1 \rightarrow {}^3B_1$	0.0000
8	8.3253	148.92	32B $\rightarrow$ 33B	0.59458	${}^3B_1 \rightarrow {}^3E$	0.0000
9	8.3283	148.92	31B $\rightarrow$ 33B	0.58471	${}^3B_1 \rightarrow {}^3E$	0.0009
10	8.4757	146.28	28B $\rightarrow$ 33B	0.62669	${}^3B_1 \rightarrow {}^3B_1$	0.0000
11	8.6962	142.57	30B $\rightarrow$ 33B	0.70344	${}^3B_1 \rightarrow {}^3E$	0.0021
12	8.6962	142.57	29B $\rightarrow$ 33B	0.70344	${}^3B_1 \rightarrow {}^3E$	0.0021
13	8.8060	140.79	33A $\rightarrow$ 35A	0.68267	${}^3B_1 \rightarrow {}^3A_1$	0.0000
14	8.8079	140.76	26B $\rightarrow$ 33B	0.67135	${}^3B_1 \rightarrow {}^3A_2$	0.0000
15	8.9114	139.13	32A $\rightarrow$ 35A	0.56118	${}^3B_1 \rightarrow {}^3E$	0.0063
16	8.9114	139.13	31A $\rightarrow$ 35A	0.56118	${}^3B_1 \rightarrow {}^3E$	0.0063
17	8.9139	139.09	25B $\rightarrow$ 33B	0.78769	${}^3B_1 \rightarrow {}^3B_1$	0.0000
18	8.9598	138.38	30A $\rightarrow$ 35A	0.62596	${}^3B_1 \rightarrow {}^3B_1$	0.0000
19	9.0011	137.74	27A $\rightarrow$ 35A	0.68812	${}^3B_1 \rightarrow {}^3A_2$	0.0000
20	9.0265	137.35	29A $\rightarrow$ 35A	0.72358	${}^3B_1 \rightarrow {}^3E$	0.1158

Tab. 4.3: CIS vertical excitation energies (eV) of the NiO(001) surface.

HOMO-LUMO transition. Similarly, the eighth state excitation corresponds to the HOMO-LUMO transition (for  $\beta$  state).

The twentieth excitation indicates the excited configuration from 29A  $\rightarrow$  35A. This state has a relatively large oscillator strength (0.1158) and corresponds to a very intense peak in the optical absorption spectrum.

### 4.2.3 Optical gap

Although the CI calculation does not directly provide information about the band gap (the band gap corresponds to experiments with variable particle number, such as x-ray photoemission, and must be obtained from a Green-function method such as GW or by identifying the ionization potential (IP) and electron affinity (EA) that will correspond to the HOMO-LUMO gap), we estimate it by keeping a track on transitions between ground and excited states from the CIS calculation possessing the symmetry of the 2p oxygen (HOMO state) and 4s nickel (LUMO) states, respectively. The lowest excited state, where this transition is strongly expressed, has an energy of 7.6 eV (the corresponding CIS coefficient is approximately 67.3%). This is much larger than the experimental value (4.0 – 4.3 eV [39, 116] in bulk NiO) or the result of a GW calculation (5.5 eV) by Aryasetiawan *et al.* [22]. Such a large discrepancy

has two origins: the importance of the correlation effects is not accounted for properly on the CIS level and the fact that the excitation energy can be identified with the HOMO-LUMO gap only in the case of infinite particle number. Therefore, to improve the gap energy we include some of the electronic correlation beyond the CIS method via second order Møller-Plesset perturbation theory called CIS-MP2 calculation. We found a smaller gap of 6.8 eV, indicating that correlation energy is of importance here. Even though our band gap between O-2p and Ni-4s state is not in good agreement with experimental data for both Mott-Hubbard and charge-transfer insulators ( $d \rightarrow d$  and  $p \rightarrow d$  characters, respectively), it provides us with an appropriate description of the low-lying  $d-d$  intragap excitations that are of interest for magnetic applications.

#### 4.2.4 Excitation spectra of NiO(001) surface

Using a Lorentzian level broadening with 0.5 eV FWHM, we obtain the density of excited states on the NiO(001) surface from 300 excitation energies (see Fig. 4.2). There are several important implications of these findings. First, in the CIS calculation, the  $d-d$  transitions lie in the range below 3.0 eV and fall within the band gap of 7.6 eV. These transitions support the results of high-resolution EELS measurements. Noguera *et al.* [64] mentioned that the EELS experiments have revealed a range of weak absorptions within the gap in the range 0.5 – 3.0 eV, which have been attributed to orbitally forbidden ( $\Delta l=0$ ) one- and two-electron bulk and (100) surface  $d-d$  excitations. Second, excitations above the gap consist of a charge-transfer (O-2p  $\rightarrow$  Ni-4s, O-2p  $\rightarrow$  Ni-4p,5p and O-2p  $\rightarrow$  Ni-3d) and an intra-atomic (Ni-3d  $\rightarrow$  Ni-4s and Ni-3d  $\rightarrow$  Ni-4p) transitions, while  $d-d$  transitions are not found in this region.

#### 4.2.5 Oscillator strengths and optical absorption spectra

In Fig. 4.3, we plot some of the oscillator strengths of allowed transitions from our 300 vertical excited states in the CIS calculation. It is shown that the oscillator strengths of optically allowed transitions correspond to O(2p)  $\rightarrow$  Ni(4s), O(2p)  $\rightarrow$  Ni(4p), O(2p)  $\rightarrow$  Ni(3d), O(2p)  $\rightarrow$  Ni(5p) and Ni(3d)  $\rightarrow$  Ni(4p) transitions labeled as (a) to (e) in Fig. 4.3. As an example, consider the group of excitations (c) for O(2p)  $\rightarrow$  Ni(3d). It is well known that the experimental band gap results from transitions of type (c), which are expected to occur at lower energies in a theory beyond the CIS level due to the correlation effects of the  $d$ -electrons. In addition, as is clear from Fig. 4.3, the oscillator strengths of these transitions are sufficiently large to make them observable. Hence, the optical absorption spectra (allowed transitions) dominantly arise from the charge-transfer states. However, it should be noted that the  $d-d$  transitions and band gap (in CIS) excitations are forbidden transitions (in linear optics) as the oscillator strength equals to zero.

#### 4.2.6 Electronic correlation effects on $d-d$ transitions

The partly filled 3d shell in solid transition-metal compounds is quite localized on the transition metal ion and gives rise to large electron correlation effects [64]. Thus, it is neces-

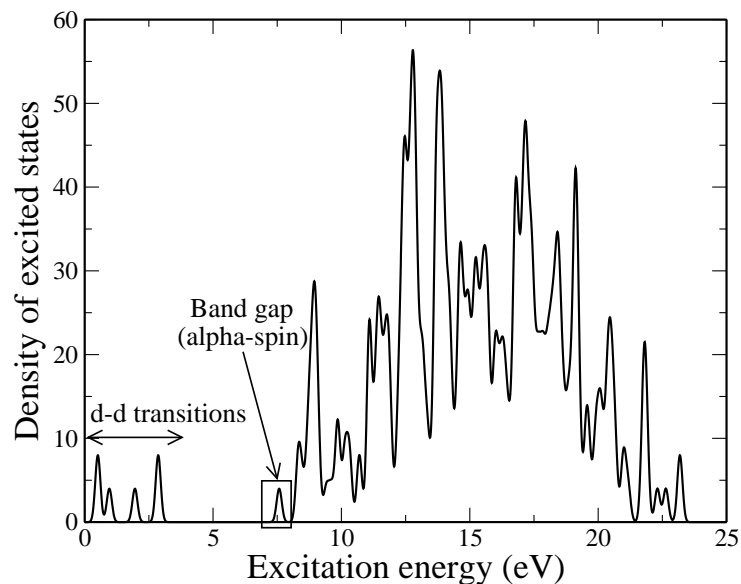


Fig. 4.2: UV/Visible spectra obtained for the NiO(001) surface.

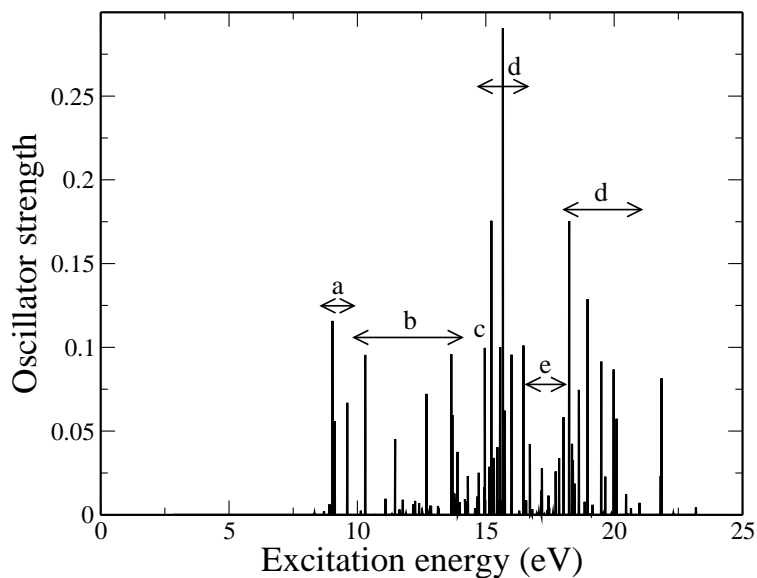


Fig. 4.3: Oscillator strengths for the optically allowed transitions. The notations (a, b, c, d and e) are used to label each transition such as  $O(2p) \rightarrow Ni(4s)$ ,  $O(2p) \rightarrow Ni(4p)$ ,  $O(2p) \rightarrow Ni(3d)$ ,  $O(2p) \rightarrow Ni(5p)$  and  $Ni(3d) \rightarrow Ni(4p)$ , respectively.

sary to include electronic correlation effects for an accurate description of  $d-d$  excitations in NiO [64, 65, 55].

Our  $d-d$  transitions for different levels of correlation, such as CID, CISD, QCISD and QCISD(T), are compared with those obtained from CIS calculation in both surface and bulk NiO (see Table 4.4). When the electronic correlation is enhanced from CID to CISD, QCISD and QCISD(T), the electron correlations significantly decrease the magnitude of excitation energies, as seen in Table 4.4. It has been clearly demonstrated that electronic correlation strongly affects the  $d-d$  transitions. Only at our highest-level theoretical method such as QCISD(T), the  $d-d$  transition energies are found to compare well with the experimental data, as shown in Table 4.5. Our bulk  $d-d$  transitions (1.13 and 2.1 eV) are somewhat higher than the SHG lines by Fiebig *et al.* [17] (1.0 eV and 1.75 eV for  ${}^3A_{2g} \rightarrow {}^3T_{2g}$  and  ${}^3A_{2g} \rightarrow {}^3T_{1g}$ , respectively).

System	Transition	Excitation energy (eV)				
		CIS	CID	CISD	QCISD	QCISD(T)
Ni <sup>2+</sup> surface	${}^3B_1 \rightarrow {}^3E$	0.51	0.51	0.52	0.53	0.53
	${}^3B_1 \rightarrow {}^3B_2$	0.96	1.02	1.04	1.16	1.17
	${}^3B_1 \rightarrow {}^3A_2$	1.96	1.64	1.64	1.32	1.21
	${}^3B_1 \rightarrow {}^3E$	2.86	2.61	2.63	2.23	1.84
Ni <sup>2+</sup> bulk	${}^3A_{2g} \rightarrow {}^3T_{2g}$	0.90	0.99	1.01	1.11	1.13
	${}^3A_{2g} \rightarrow {}^3T_{1g}$	2.74	2.53	2.55	2.27	2.10

Tab. 4.4: Calculated  $d-d$  excitation energies (eV) of the NiO(001) surface and bulk NiO at differential levels of *ab initio* correlated theory (this work).

### 4.2.7 $d-d$ transitions

In this part, we would like to emphasize our  $d-d$  transitions in the more details and discuss how the electron transfers between  $3d$ -orbitals for both bulk and (001) surface systems of NiO.

As stated before, our calculation also yields the optically active states within the gap of NiO, their character depends on the local symmetry: in the clusters which simulate bulk NiO, the gap states have a charge-transfer character. On the surface, however, a strong contribution of the optically active  $d-d$  transitions can be observed. These excited states have energies lower than the charge-transfer excitation, which is important in describing the optical properties of the TMO. An understanding of these transitions is very important for the development of the theory of surface SHG in NiO(001) [117, 118].

In Table 4.5, we compare the  $d-d$  excitation energies of Ni<sup>2+</sup> ions on the NiO(001) surface in our highest-level calculation with available theoretical and experimental data. The  $d-d$  transitions for bulk NiO are also shown for comparison of surface  $d-d$  transitions. These transitions are only related to triplet-triplet excitations. The last column in Table 4.5 shows our predicted transitions at energies of 0.53, 1.17, 1.21 and 1.84 eV. The excited states at the

lowest energy are twofold degenerate  $d_{xz}(d_{yz}) \rightarrow d_{3z^2-r^2}$  transitions; the one-electron  $d_{xy} \rightarrow d_{x^2-y^2}$  transition is at higher energy of 1.17 eV. Additionally, the one-electron  $d_{xy} \rightarrow d_{3z^2-r^2}$  transition has a relative energy of 1.21 eV and the energetically highest state is the twofold degenerate  $d_{xz}(d_{yz}) \rightarrow d_{x^2-y^2}$  transition at 1.84 eV. In bulk NiO, there are two threefold degenerate excitations ( ${}^3T_{2g}$  and  ${}^3T_{1g}$  excited states). The  ${}^3T_{2g}$  state consists of triple excitations such as  $d_{xz} \rightarrow d_{x^2-y^2}$ ,  $d_{xy} \rightarrow d_{x^2-y^2}$  and  $d_{yz} \rightarrow d_{3z^2-r^2}$ , while the  ${}^3T_{1g}$  state has  $d_{yz} \rightarrow d_{x^2-y^2}$ ,  $d_{xz} \rightarrow d_{3z^2-r^2}$  and  $d_{xy} \rightarrow d_{3z^2-r^2}$ . The excitation energies of the  ${}^3T_{2g}$  and  ${}^3T_{1g}$  states are about 1.13 and 2.10 eV, respectively. Our calculated excitation energies for  $d-d$  transitions are in good agreement with the experimental observations and with the theoretical calculations in both surface and bulk NiO. In Sec. 4.5 we will calculate and discuss the SHG spectra.

State	Transition	Excitation energy (eV)		This work	
		Theory <sup>†</sup>	Experiment <sup>†</sup>	QCISD(T)	Transition
Ni <sup>2+</sup> surface	${}^3B_1 \rightarrow {}^3E$	0.65, 0.62, 0.50	0.57, 0.60	0.53	$d_{xz} \rightarrow d_{3z^2-r^2}$ $d_{yz} \rightarrow d_{3z^2-r^2}$
	${}^3B_1 \rightarrow {}^3B_2$	1.00, 0.98, 0.83	1.00	1.17	$d_{xy} \rightarrow d_{x^2-y^2}$
	${}^3B_1 \rightarrow {}^3A_2$	1.30, 1.21	1.30	1.21	$d_{xy} \rightarrow d_{3z^2-r^2}$
	${}^3B_1 \rightarrow {}^3E$	1.44, 1.38, 1.85	1.62	1.84	$d_{xz} \rightarrow d_{x^2-y^2}$ $d_{yz} \rightarrow d_{x^2-y^2}$
Ni <sup>2+</sup> bulk	${}^3A_{2g} \rightarrow {}^3T_{2g}$	1.00, 0.81, 0.86	1.13, 1.08 1.05, 1.10	1.13	$d_{xz} \rightarrow d_{x^2-y^2}$ $d_{xy} \rightarrow d_{x^2-y^2}$ $d_{yz} \rightarrow d_{3z^2-r^2}$
	${}^3A_{2g} \rightarrow {}^3T_{1g}$	1.72, 1.81 2.07, 2.21	1.95, 1.86 1.79, 1.87	2.10	$d_{yz} \rightarrow d_{x^2-y^2}$ $d_{xz} \rightarrow d_{3z^2-r^2}$ $d_{xy} \rightarrow d_{3z^2-r^2}$

Tab. 4.5: Calculated  $d-d$  excitation energies (eV) of the NiO(001) surface and bulk NiO compared to available experimental and theoretical data.

<sup>†</sup>Taken from Ref. [64], and references therein.

### 4.3 Electron density

The pictures below are the electron density<sup>1</sup> plotted using the electronic potential calculated at points of ground and excited states for both the NiO(001) surface and bulk NiO. These serve two purposes. First, the 2D contour-line pictures are used to discuss the spin density in term of the deference between alpha and beta spin densities ( $\rho^\alpha(r) - \rho^\beta(r)$ ). Second, the 3D pictures show the electron density contributing to the better understanding of the different densities obtained at each ground and excited states. The 3D visualization of the electron density surfaces may provide a more exciting insight than the 2D representation.

<sup>1</sup> The electron density function or electron probability distribution function,  $\rho(r)$ , is a three-dimensional function defined such that  $\rho(r)dr$  is the probability of finding an electron in a small volume element,  $dr$  at some point in space,  $r$ .

### 4.3.1 NiO(001) surface

Figures 4.4 – 4.8 show the representations of spin densities for ground and excited states (only  $d-d$  transitions) on the NiO(001) surface. The contour lines in the black color correspond to the densities of 0.01, 0.005, 0.001, 0.0005, and 0.0001 a.u.<sup>-3</sup> and the red lines represent the same densities for the negative value. By comparing the results, we find significant changes as well as rather moderate changes in the spin densities among these ground and excited states. In contrast, the total electron density remains almost the same for all states. The spin density is closely related to the distribution of magnetic moments in the cluster, and can be described by the net atomic spin. The net atomic spin is a scalar quantity that can be assigned to each nuclei of the cluster and describes excess or lack of spin density on the atom. In the case of an isolated atom the net atomic spin can be defined unambiguously and is just a difference between the number of spin-up and spin-down electrons. In the case of a cluster, there are several approaches for the computation of this quantity. The simplest one assumes the net atomic spin to be just a sum of molecular orbital coefficients corresponding to the basis function residing on this atom. A more appropriate definition of this quantity can be obtained by fitting the electric field created by the electrons (all, spin-up, or spin-down) in the system to the set of point charges placed at positions of nuclei. These charges are then called net atomic charges (spins) depending on which electric field is considered. In contrast, the magnetic moment is a vector quantity that has a quantization direction and is proportional to the net spin. In order to analyze the distribution of magnetic moments in NiO we use net spins obtained from the Mulliken population analysis.

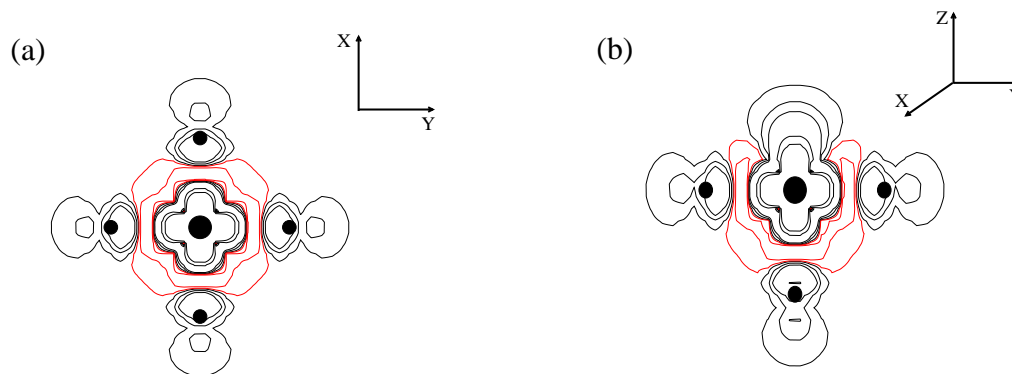


Fig. 4.4: Contour plot of the difference of spin densities between spin-up and spin-down for the ground state of the  $(\text{NiO}_5)^{8-}$  cluster modelling the NiO(001) surface: (a) top view on the section in the surface plane; (b) side view on the same section. Black lines show contours corresponding to the densities of 0.01, 0.005, 0.001, 0.0005, 0.0001 a.u.<sup>-3</sup>. Red lines show the same for negative densities.

The spin density of the ground state depicted in Fig. 4.4 demonstrates two effects that: (i) the electrons along the surface plane are localized within the  $(\text{NiO}_5)^{8-}$  cluster (Fig. 4.4 (a)), which may show that our embedding model works well, otherwise the electrons would

escape attracted by the positive point charges around the cluster; (ii) the additional spin density trying to escape the surface, tends to occupy the most diffuse atomic orbitals, which belong to Ni atom (Fig. 4.4 (b)). The ground state configuration is the most symmetric one and is characterized by an almost homogeneous distribution of the net atomic spins among the oxygen atoms (Tab. 4.1).

It is interesting to observe how the difference in symmetry and energy of the states are reflected by the distribution of the magnetic moments in the cluster. The comparison of the ground-state spin density to those of the excited states reveals the following features of their electronic structure. For the lowest  ${}^3E$  excited state (Fig. 4.5), the spin densities of the doubly degenerate state shows slightly higher net spin on the nickel atom ( $\delta n_s = 1.93$ ) due to the flowing of the spin density from the apex O atom ( $\delta n_s = 0.004$ ) and its distribution among in-plane oxygen atoms.

This is the result of the  $d_{xz} \rightarrow d_{3z^2-r^2}$  and  $d_{yz} \rightarrow d_{3z^2-r^2}$  transitions<sup>2</sup> giving the major contribution to the two modes of this state. As can be seen from the visualisation of these occupied (Fig. 4.10) and virtual orbitals (Fig. 4.11)  $3d$  orbitals, the  $d_{xz}$  and  $d_{yz}$  states can be transformed one in another by the  $\pi/2$  rotation in the  $x-y$  plane, while the  $d_{3z^2-r^2}$  has the  $z$  axial symmetry. Therefore the net atomic spin is different for the oxygen atom on the  $x$  and  $y$  axis ( $\delta n_s = 0.019$  and  $0.015$ ).

In the second  ${}^3B_2$  state the net spins reside almost completely on the Ni ( $\delta n_s = 1.97$ ) and vertex O ( $\delta n_s = 0.023$ ), while being vanishing on the rest (Figs. 4.6). This is caused by the  $d_{xy} \rightarrow d_{x^2-y^2}$  electronic transition.

The most significant changes in the distribution of net spins compared to the ground state configuration was observed for the  ${}^3A_2$  excited state (Fig. 4.7). Very high spin density was found on the in-plane oxygen atoms ( $\delta n_s = 0.027$ ) This is the result of negative net spin residing on the out of plane oxygen ( $\delta n_s = -0.001$ ) and moderate on the nickel ( $\delta n_s = 1.89$ ). As before this agrees well with the electronic transition among  $d_{xy}$  and  $d_{3x^2-r^2}$  orbitals.

The last  ${}^3E$  electronic state is highly asymmetric with in-plane preferable direction (two modes corresponding to the transitions ( $d_{xz} \rightarrow d_{x^2-y^2}$  and  $d_{yz} \rightarrow d_{x^2-y^2}$  are found). Two of the O atoms have net spins  $\delta n_s = 0.014$ , while their counterparts possess only  $\delta n_s = -0.002$ . This is understandable in view of the fact that very distorted electronic configurations are only possible at higher cluster energy. It is also interesting to remark that for none of the excited states the electron density is distributed symmetrically around the oxygen atoms as would be expected in the case of an infinitely large cluster. This clearly demonstrates the deficiency of the embedded cluster model and suggests to perform calculations with a larger number of atoms in the cluster.

Figures 4.9 – 4.14 illustrate the calculated electron densities of ground and excited states on the NiO(001) surface. The electron density of the ground state is shown as Fig. 4.9 (a) and the total electron density corresponding to the majority (alpha-spin) of the electron is depicted (see Fig. 4.9 (b)). For the ground state properties, again, we also show a series of  $d$ -orbitals

<sup>2</sup> Here we continue to use a notation for the single-particle states in accordance with spherical symmetry classification in order to emphasize their geometric structure. In fact for the  $C_{4v}$  symmetry, the states  $d_{xz}(d_{yz})$ ,  $d_{3z^2-r^2}$ ,  $d_{xy}$ , and  $d_{x^2-y^2}$  get their notation according to the irreducible representations of this point group:  $e$ ,  $a_1$ ,  $b_1$ ,  $b_2$ .

in the electron densities from Figs. 4.10 – 4.11. The Fig. 4.10 (left), (right), and (center) refer to the occupied  $d$ -orbitals of  $d_{xz}$ ,  $d_{yz}$ , and  $d_{xy}$ , respectively. For the virtual  $d$ -orbitals such as  $d_{3z^2-r^2}$  and  $d_{x^2-y^2}$ , the electron densities are carried out (Fig. 4.11 (left) and (right)).

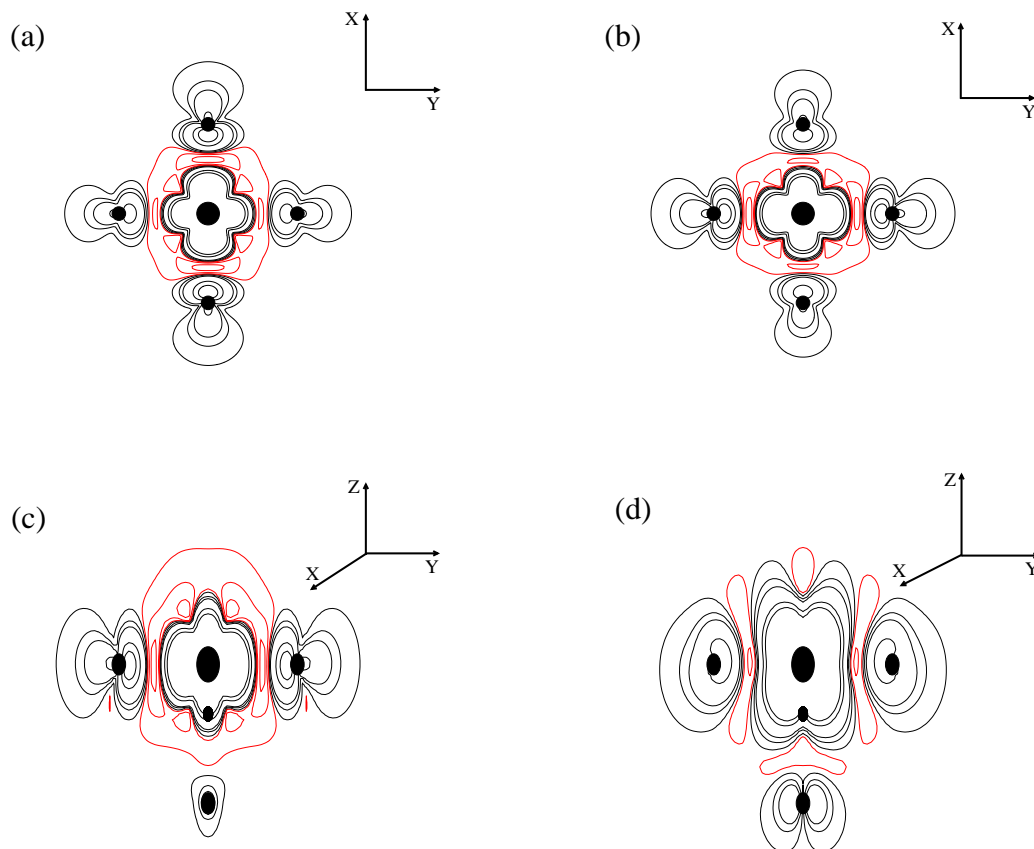


Fig. 4.5: Contour plot of the difference of spin densities between spin-up and spin-down for the double degenerate  ${}^3E$  excited state of the  $(\text{NiO}_5)^{8-}$  cluster modelling the NiO(001) surface: (a) and (b) top view on the section in the surface plane; (c) and (d) side view on the same section. Black lines show contours corresponding to the densities of 0.01, 0.005, 0.001, 0.0005, 0.0001 a.u. $^{-3}$ . Red lines show the same for negative densities.

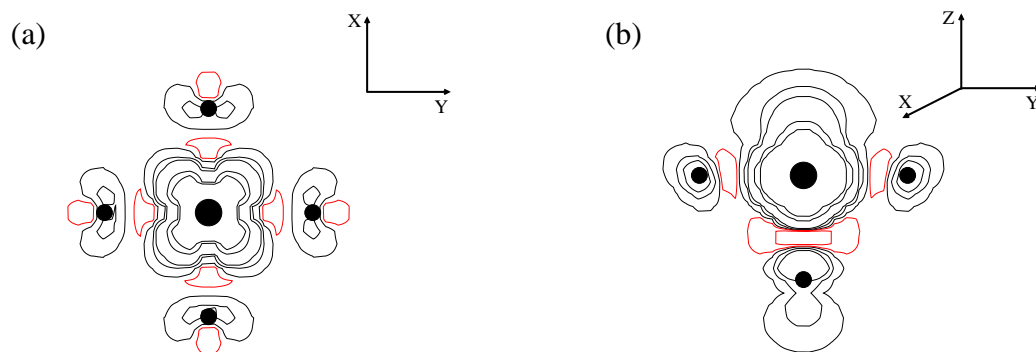


Fig. 4.6: Contour plot of the difference of spin densities between spin-up and spin-down for the  ${}^3B_2$  excited state of the  $(\text{NiO}_5)^{8-}$  cluster modelling the NiO(001) surface: (a) top view on the section in the surface plane; (b) side view on the same section. Black lines show contours corresponding to the densities of 0.01, 0.005, 0.001, 0.0005, 0.0001 a.u. $^{-3}$ . Red lines show the same for negative densities.

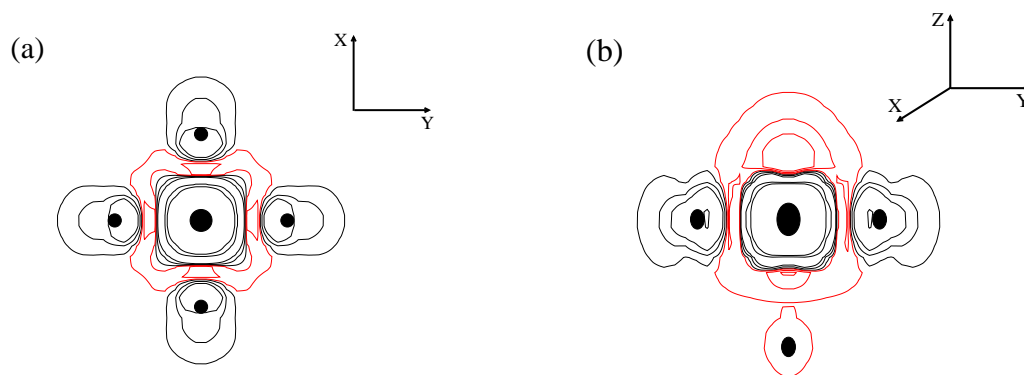


Fig. 4.7: Contour plot of the difference of spin densities between spin-up and spin-down for the  ${}^3A_2$  excited state of the  $(\text{NiO}_5)^{8-}$  cluster modelling the NiO(001) surface: (a) top view on the section in the surface plane; (b) side view on the same section. Black lines show contours corresponding to the densities of 0.01, 0.005, 0.001, 0.0005, 0.0001 a.u. $^{-3}$ . Red lines show the same for negative densities.

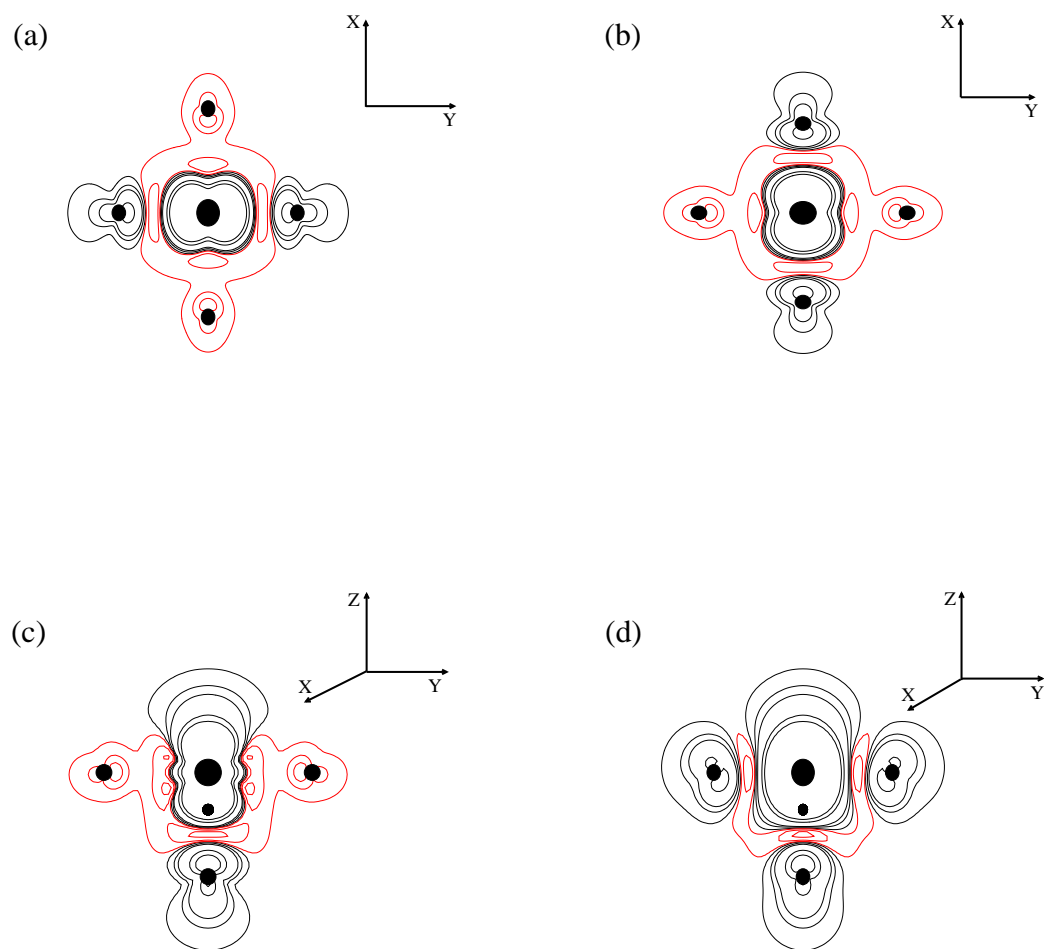


Fig. 4.8: Contour plot of the difference of spin densities between spin-up and spin-down for the double degenerate  ${}^3E$  excited state of the  $(\text{NiO}_5)^{8-}$  cluster modelling the NiO(001) surface: (a) and (b) top view on the section in the surface plane; (c) and (d) side view on the same section. Black lines show contours corresponding to the densities of 0.01, 0.005, 0.001, 0.0005, 0.0001 a.u.<sup>-3</sup>. Red lines show the same for negative densities.

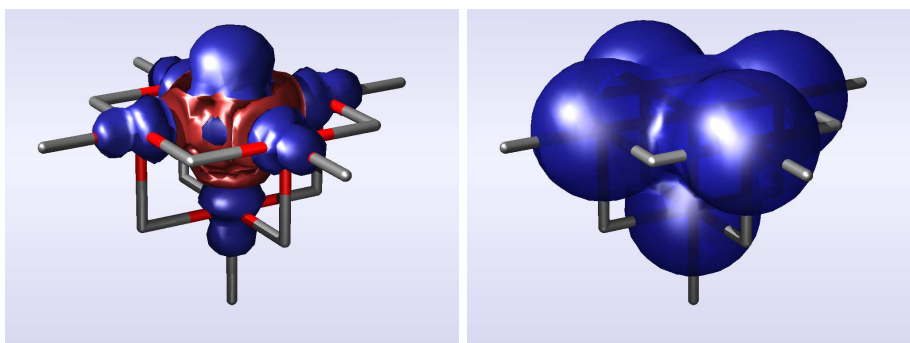


Fig. 4.9: (a) Left: surface electron density at  $0.01 \text{ a.u.}^{-3}$  of the ground state. (b) Right: the total spin electron density corresponds to the majority spin of the ground state.

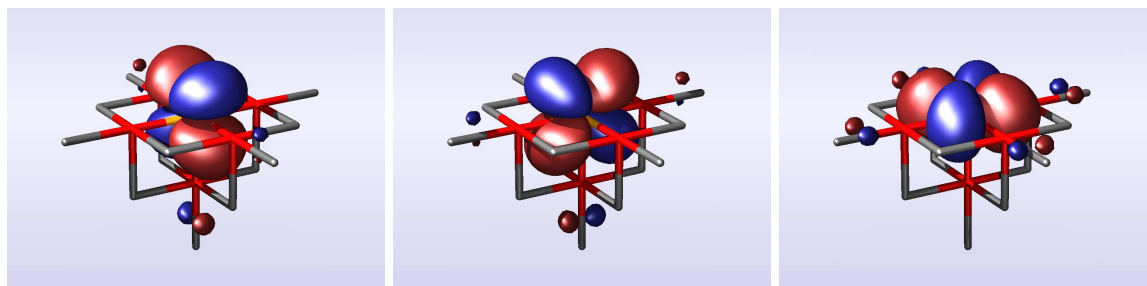


Fig. 4.10: Electron density at  $0.05 \text{ a.u.}^{-3}$  of the occupied  $d$ -orbitals. Spin-down  $d_{xz}$ ,  $d_{yz}$ , and  $d_{xy}$  orbitals are shown.

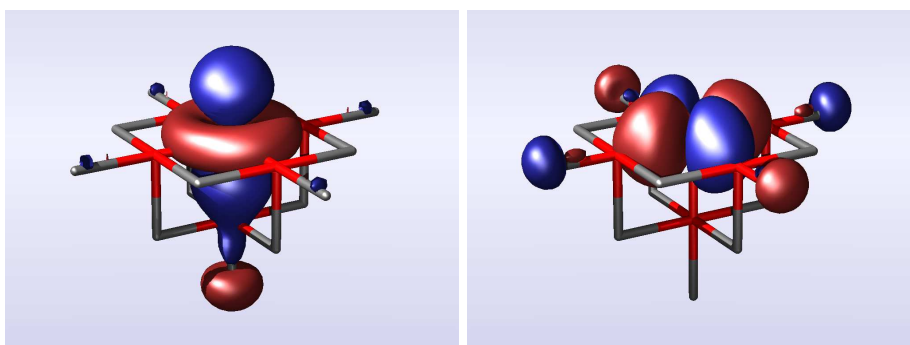


Fig. 4.11: Electron density at  $0.05 \text{ a.u.}^{-3}$  of the virtual  $d$ -orbitals. Spin-down  $d_{3z^2-r^2}$  and  $d_{x^2-y^2}$  orbitals are shown.

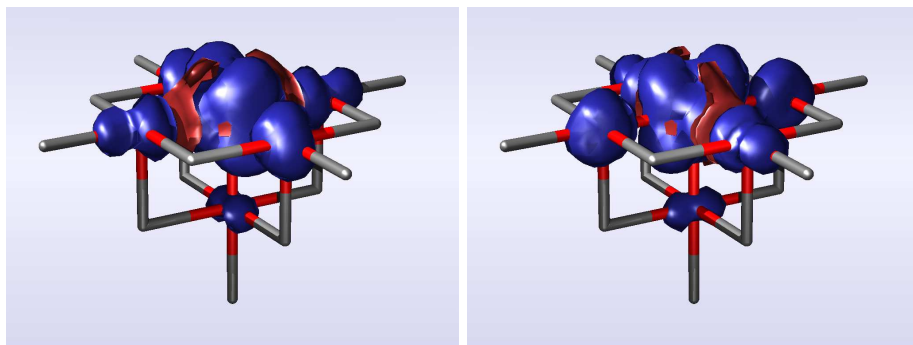


Fig. 4.12: Surface electron density at  $0.01 \text{ a.u.}^{-3}$  of the doubly degenerate 1st excited state.

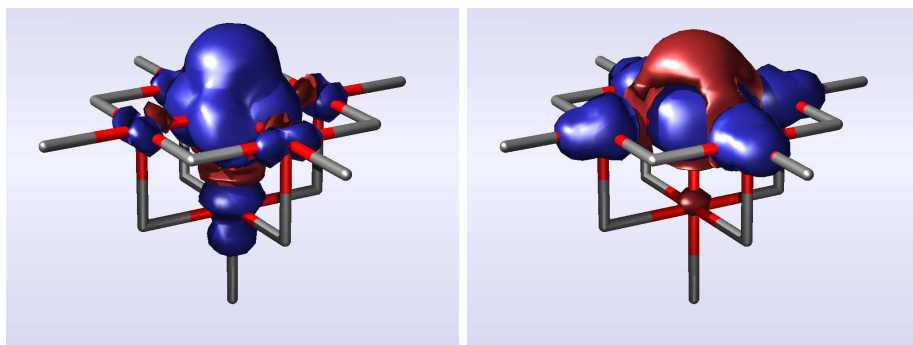


Fig. 4.13: Surface electron density at  $0.01 \text{ a.u.}^{-3}$  of the 2nd and 3rd excited states.

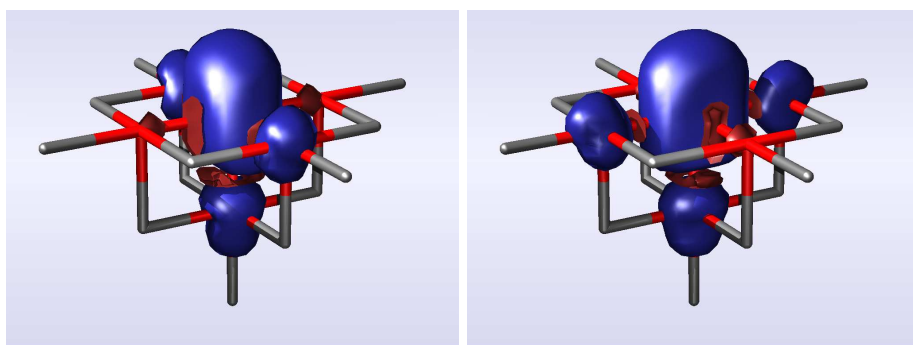


Fig. 4.14: Surface electron density at  $0.01 \text{ a.u.}^{-3}$  of the doubly degenerate 4th excited state.

### 4.3.2 Bulk NiO

Figures 4.15 - 4.17 show the contour plots of spin-densities for ground and excited states ( $d-d$  transitions) in bulk NiO. For these products, we found the most interesting features on the ground state (see Fig. 4.15 (a) and (b)). They show the same electron densities at such a point along with x-, y-, and z-axis reflecting the full ( $O_h$ ) symmetry of the ground state in bulk NiO. The areas of positive spin densities are localized around Ni and each of the O atoms. The negative spin density occupies a narrow interstitial region around the central atom.

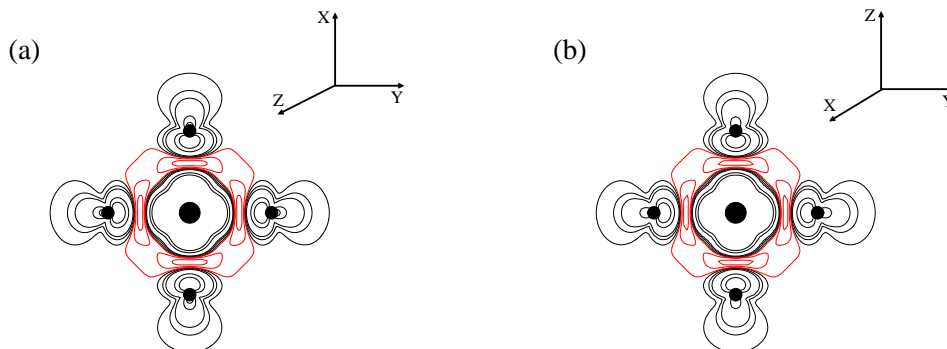


Fig. 4.15: Contour plot of the difference of spin densities between spin-up and spin-down for the ground state of the  $(\text{NiO}_6)^{10-}$  cluster modelling the bulk NiO: (a) side view along with x-axis; (b) side view along with z-axis. Black lines show contours corresponding to the densities of 0.01, 0.005, 0.001, 0.0005, 0.0001 a.u.<sup>-3</sup>. Red lines show the same for the negative densities.

The net atomic spin of the Ni atom is  $\delta n_s = 1.866$ , the rest is equally distributed over oxygen atoms ( $\delta n_s = 0.022$ ). This is interesting fact showing that the magnetic moment of Ni atom in the bulk environment is smaller than on the (001) surface<sup>3</sup> (Tab. 4.1). Comparison of the spin density plots for the bulk and surface NiO (Fig. 4.15 and Fig. 4.4) reveals how the accessing magnetic moment is formed on the surface Ni atom. In this case the termination of the broken Ni-O bond is expressed as a superfluity of alpha electrons on the diffusive Ni orbitals.

For the threefold degenerate  $T_{2g}$  excited state (Fig. 4.16), the spin-densities contain three modes corresponding to  $d-d$  transitions ( $d_{xz} \rightarrow d_{x^2-y^2}$ ,  $d_{xy} \rightarrow d_{x^2-y^2}$ , and  $d_{yz} \rightarrow d_{3z^2-r^2}$ ). These transitions course a flow of the spin density from four of the oxygen atoms to the Ni atom

<sup>3</sup> As explained before, the net atomic spin is not exactly the magnetic moment of the atom, although these quantities are closely related. Here, we would like to remark about the orbital moment contribution to the total magnetic moment of the Ni atom. A recent magnetic x-ray scattering measurement (V. Fernandez *et al.*, Phys. Rev. B **57**, 7870 (1998)) indicates that the orbital-to-spin angular momentum ratio in NiO is as large as  $L/S = 0.34$ , far from fully quenched orbital moment. In this experiment was also found that the spin and orbital moments in NiO are collinear. The importance of orbital magnetic moment was confirmed in recent LSDA+ $U$  calculations (S. K. Kwon and B. I. Min, Phys. Rev. B **62**, 73 (2000)) which give the values for the orbital moment  $\mu_L = 0.29$  and spin moment  $\mu_S = 1.64$ .

increasing its net spin ( $\delta n_s = 1.932$ ). The corresponding O atoms become than less polarized ( $\delta n_s = 0.006$ ) (see also Fig. 4.21).

Similarly, at the threefold degenerate  $T_{1g}$  excited state (Fig. 4.17), three spin densities corresponding to  $d-d$  transitions ( $d_{xz} \rightarrow d_{3z^2-r^2}$ ,  $d_{xy} \rightarrow d_{3z^2-r^2}$ , and  $d_{yz} \rightarrow d_{x^2-y^2}$ ) result in increase of the net spin of the Ni ( $\delta n_s = 1.913$ ) due to the transition of the spin density from two of the oxygen atoms ( $\delta n_s = -0.002$ ) (see also Fig. 4.22).

Various  $3d$ -orbitals of bulk NiO are shown in Figures 4.19 - 4.20. The  $d_{3z^2-r^2}$  orbital has two nodal cones. The  $d_{x^2-y^2}$  has two nodal planes. The other three  $d$ -orbitals have the same shape but have different orientations, forming three times degenerate  $t_{2g}$  state. The  $d_{xz}$  and  $d_{yz}$  orbitals have their lobes between the x and z axes and between the y and z axes, while the  $d_{xy}$  orbital has its lobes lying between the x and y axes. Both orbital and magnetic moments are larger in NiO than in fcc Ni which has  $\mu_L = 0.06$  and  $\mu_S = 0.63$ . This suggests that the  $d$ -orbitals in NiO are more localized than in Ni metal. Finally, the calculated electron densities of ground state ( $^3A_{2g}$ ) and excited states ( $^3T_{2g}$  and  $^3T_{1g}$ ) in bulk NiO are shown in Figures 4.18 and 4.21- 4.22.

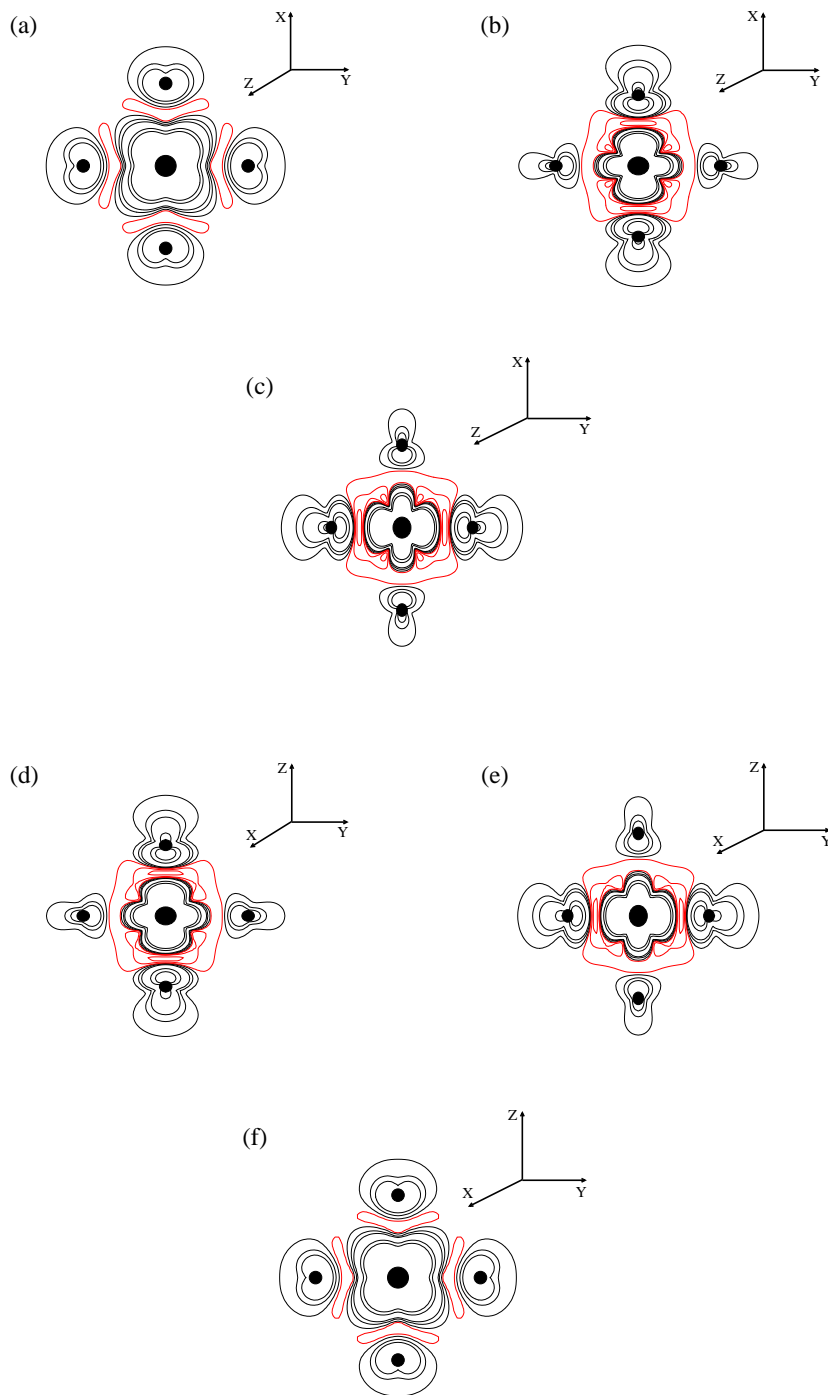


Fig. 4.16: Contour plot of the difference of spin densities between spin-up and spin-down for the triple degenerate  ${}^3T_{2g}$  excited state of the  $(\text{NiO}_6)^{10-}$  cluster modelling the bulk NiO: (a), (b), and (c) side view along with x-axis; (d), (e), and (f) side view along with z-axis. Black lines show contours corresponding to the densities of 0.01, 0.005, 0.001, 0.0005, 0.0001 a.u. $^{-3}$ . Red lines show the same for the negative densities.

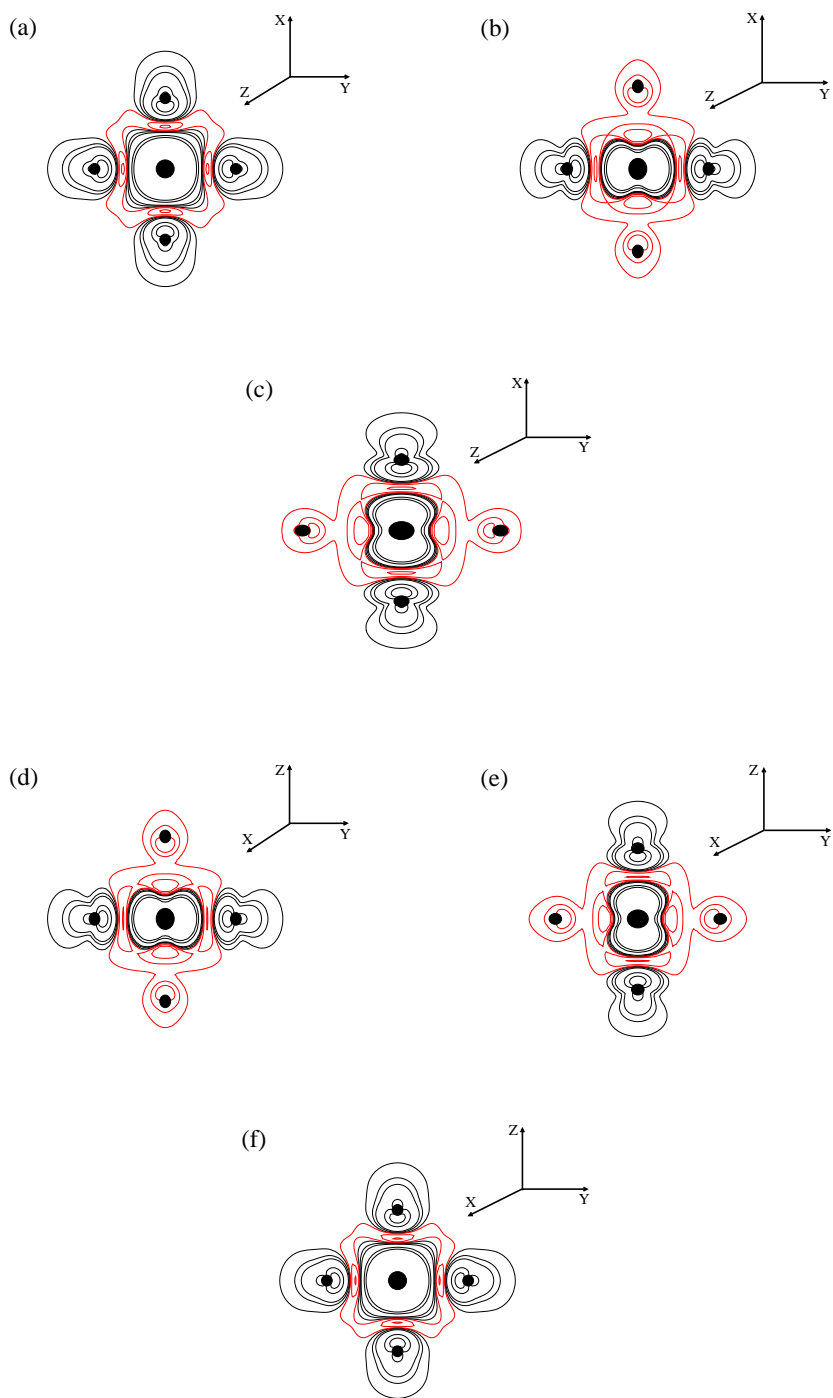


Fig. 4.17: Contour plot of the difference of spin densities between spin-up and spin-down for the triple degenerate  ${}^3T_{1g}$  excited state of the  $(\text{NiO}_6)^{10-}$  cluster modelling the bulk NiO: (a), (b), and (c) side view along with x-axis; (d), (e), and (f) side view along with z-axis. Black lines show contours corresponding to the densities of 0.01, 0.005, 0.001, 0.0005, 0.0001 a.u. $^{-3}$ . Red lines show the same for the negative densities.

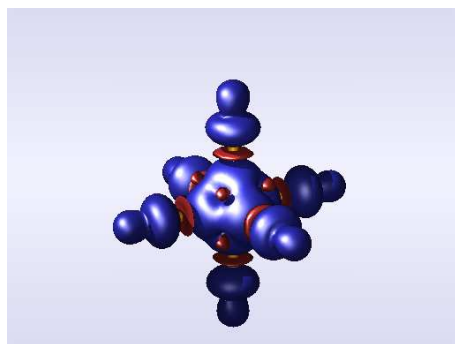


Fig. 4.18: Electron density at  $0.01 \text{ a.u.}^{-3}$  of the ground state of the  $(\text{NiO}_6)^{10-}$  cluster modelling the bulk NiO.

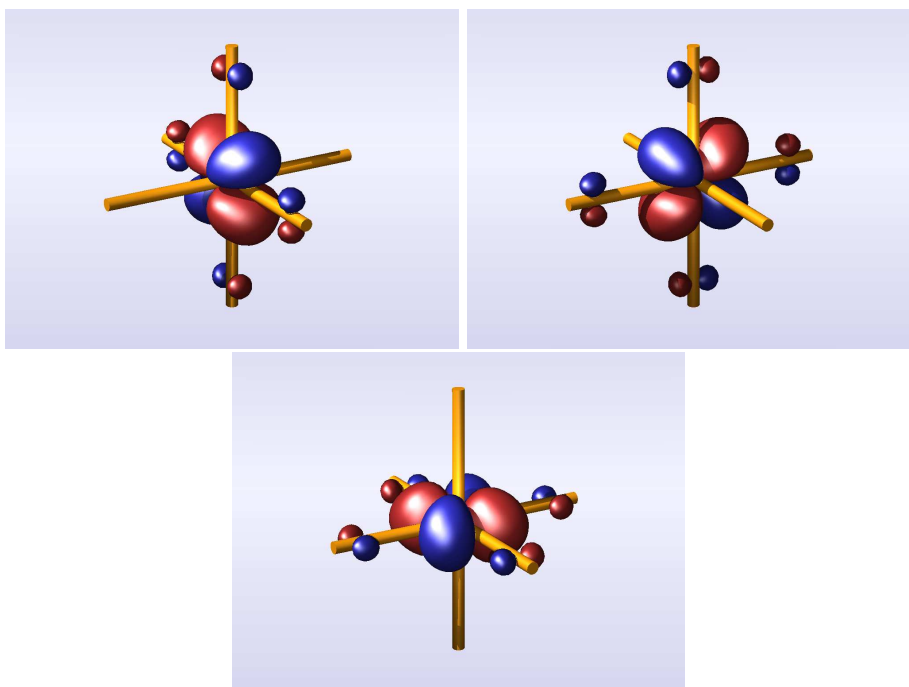


Fig. 4.19: Electron density at  $0.05 \text{ a.u.}^{-3}$  of the occupied  $d$ -orbitals. Spin-down  $d_{xz}$ ,  $d_{xy}$ , and  $d_{yz}$  orbitals are shown.

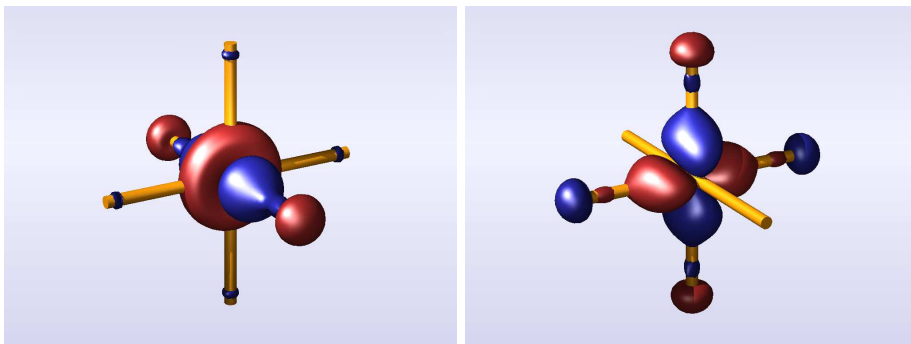


Fig. 4.20: Electron density at  $0.05 \text{ a.u.}^{-3}$  of the virtual  $d$ -orbitals. Spin-down  $d_{3z^2-r^2}$  and  $d_{x^2-y^2}$  orbitals are shown.

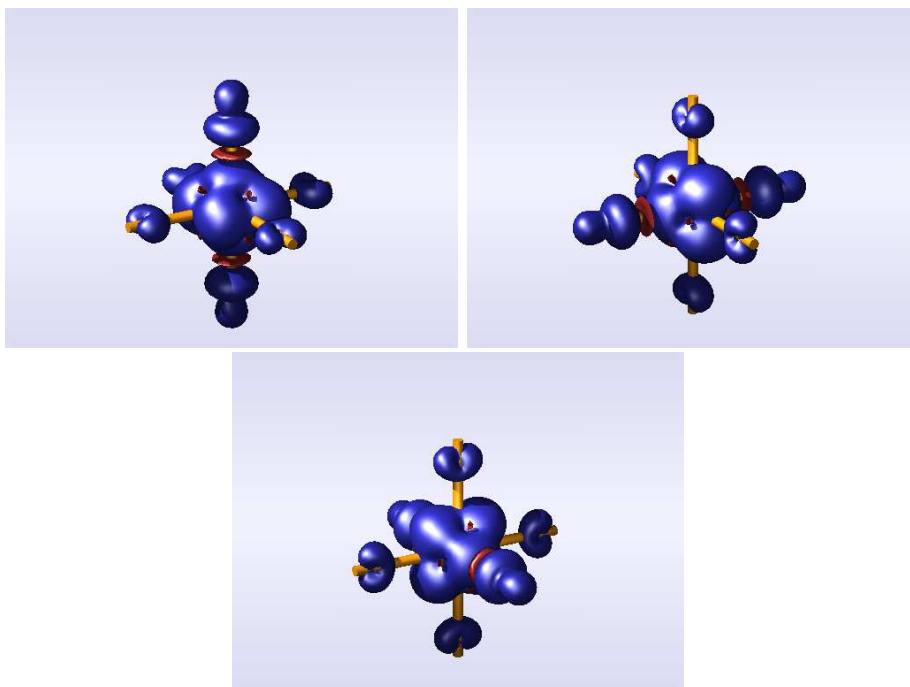


Fig. 4.21: Electron density at  $0.01 \text{ a.u.}^{-3}$  of the triple degenerate  ${}^3T_{2g}$  excited state of the  $(\text{NiO}_6)^{10-}$  cluster modelling bulk NiO.

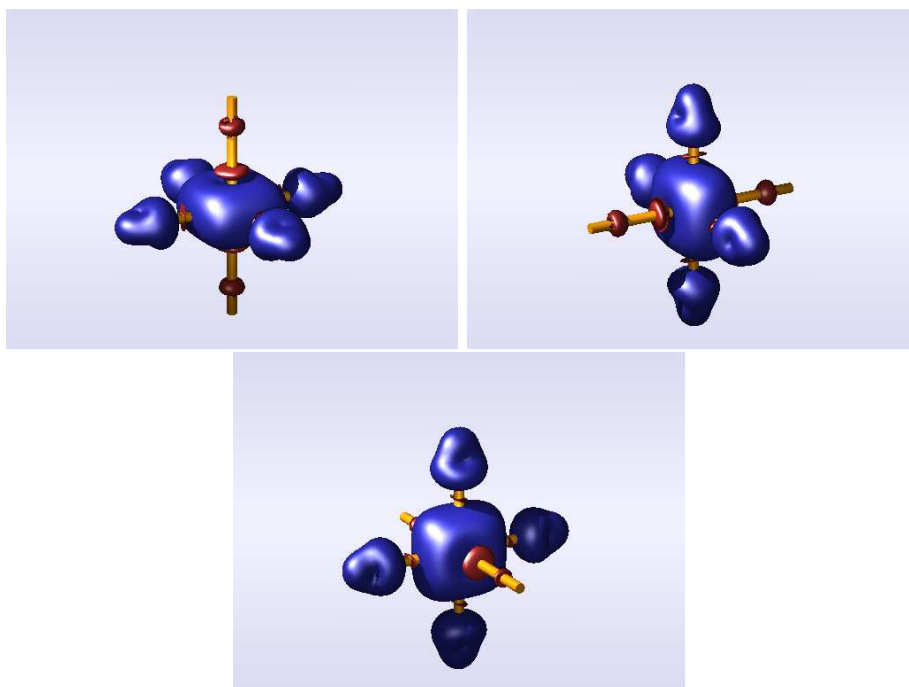


Fig. 4.22: Electron density at  $0.01 \text{ a.u.}^{-3}$  of the triple degenerate  ${}^3T_{1g}$  excited state of the  $(\text{NiO}_6)^{10-}$  cluster modelling bulk NiO.

## 4.4 Inclusion of spin-orbit coupling

### 4.4.1 Crystal field theory and the Shubnikov point groups

Cracknell (1968) [113], presented the methods for determining the splitting of atomic energy levels for various relative magnitudes of crystal field and spin-orbit coupling, where the crystal field has the symmetry of one of the magnetic (Shubnikov) point groups. It is based on the Kramers' theorem that can therefore state the following modification as below.

*Theorem:* For an odd number of electrons, in a situation whose symmetry is described by one of the type III magnetic point groups  $\mathbf{M}$ ,<sup>4</sup> every level will be at least twofold degenerate if the element is contained in the set  $\mathbf{AG}$  of the anti-unitary elements of  $\mathbf{M}$ .

In this section we show how this conventional theory is now possible to obtain a complete picture of the crystal field splitting of energy levels. It is not intended to repeat the complete theory of the deduction of the magnetic point groups. Rather, we will simply outline the essential concepts commonly used in this work.

#### For bulk NiO

We now examine how to systematically split the terms of  ${}^3F$  in  $m'3m'$  symmetry<sup>5</sup> in a crystal field, i.e.  $L = 3$ . In Table 4.6 which indicates that the  ${}^3F$  term is split by the crystalline field into one non-degenerate level ( $DA_2$ ) and two two-fold degenerate levels ( $DT_2$  and  $DT_1$ ), i.e.

$$D\mathcal{D}^L = D\mathcal{D}^3 = DA_2 + DT_2 + DT_1 \quad (4.1)$$

We are now considering a  ${}^3F$  term, that is when  $S = 1$  (spin multiplicity equals to 1). The degeneracies of the levels in Fig. 4.23, if spin is included,  $1 \times (2S + 1) = 3$  for  $DA_2$ ,  $3 \times (2S + 1) = 9$  for  $DT_2$ , and  $3 \times (2S + 1) = 9$  for  $DT_1$ . If we add weak spin-orbit coupling to the situation illustrated in Fig. 4.23, we have to reduce the inner Kronecker products:

$$D\mathcal{D}^1 \otimes DA_2 = \sum_k d_{ij,k} DX_k, \quad (4.2)$$

$$D\mathcal{D}^1 \otimes DT_2 = \sum_k d_{ij,k} DX_k, \quad (4.3)$$

$$D\mathcal{D}^1 \otimes DT_1 = \sum_k d_{ij,k} DX_k \quad (4.4)$$

<sup>4</sup> The point groups may be classified into three types, which we may call type I, type II, and type III, as follows: I: the ordinary point groups, of which are 32, II: the 'grey' point groups, of which there are also 32, and III: the 'black and white' point groups, of which there are 58. Each of the type II and type III magnetic point groups can be written as:  $\mathbf{M} = \mathbf{G} + \mathbf{AG}$ , where the elements of  $\mathbf{G}$  are unitary and form a halving subgroup of  $\mathbf{M}$  and the elements of the coset  $\mathbf{AG}$  are anti-unitary.

<sup>5</sup>  $m'3m'$  is the magnetic point group of O symmetry. Note that the bulk NiO has a high symmetry of  $O_h$  group which can be reduced to  $O \otimes C_i$  (O point group with the inversion symmetry).

The corep  $D\mathcal{D}^1$  of the group  $m'3m'$  can be seen from Table 4.6 (single-valued representations<sup>6</sup>) to be irreducible and equal to  $DT_1$ . Equations 4.17 to 4.4 therefore become:

$$DT_1 \otimes DA_2 = \sum_k d_{ij,k} DX_k, \quad (4.5)$$

$$DT_1 \otimes DT_2 = \sum_k d_{ij,k} DX_k, \quad (4.6)$$

$$DT_1 \otimes DT_1 = \sum_k d_{ij,k} DX_k \quad (4.7)$$

L	G	M
0	$A_1$	$DA_1,$ 1(1)
1	$T_1$	$DT_1,$ 1(3)
2	$E+T_2$	$DE+DT_2,$ 1(2)+1(3)
3	$A_2+T_1+T_2$	$DA_2+DT_1+DT_2,$ 1(1)+1(3)+1(3)
4	$A_1+E+T_1+T_2$	$DA_1+DE+DT_1+DT_2,$ 1(1)+1(2)+1(3)+1(3)
5	$E+2T_1+T_2$	$DE+2DT_1+DT_2,$ 1(2)+2(3)+1(3)

Tab. 4.6: The splitting of levels.

By using Table 4.7 we therefore determine the reduction of  $DT_1 \otimes DA_2$ ,  $DT_1 \otimes DT_2$ , and  $DT_1 \otimes DT_1$ , and find that

$$DT_1 \otimes DA_2 = DT_2, \quad (4.8)$$

$$DT_1 \otimes DT_2 = DA_2 + DE + DT_1 + DT_2, \quad (4.9)$$

$$DT_1 \otimes DT_1 = DA_1 + DE + DT_1 + DT_2 \quad (4.10)$$

<sup>6</sup> The inner Kronecker product will either involve two single-valued representations if  $S$  is an integer, or one single-valued and one doubled-valued representation if  $S$  is half an odd integer.

Therefore, the three levels  $DA_2$ ,  $DT_2$ , and  $DT_1$  split, when weak spin-orbit coupling is introduced, as shown in Fig. 4.23.

Products
$A_1 \otimes A_1 = A_1$ ;
$A_1 \otimes A_2 = A_2$ ;
$A_2 \otimes A_2 = A_1$ ;
$A_1 \otimes E = E$ ;
$A_2 \otimes E = E$ ;
$E \otimes E = A_1 + A_2 + E$ ;
$A_1 \otimes T_1 = T_1$ ;
$A_2 \otimes T_1 = T_2$ ;
$E \otimes T_1 = T_1 + T_2$ ;
$A_1 \otimes T_2 = T_2$ ;
$A_2 \otimes T_2 = T_1$ ;
$E \otimes T_2 = T_1 + T_2$ ;
$T_1 \otimes T_1 = A_1 + E + T_1 + T_2$ ;
$T_1 \otimes T_2 = A_2 + E + T_1 + T_2$ ;
$T_2 \otimes T_2 = A_1 + E + T_1 + T_2$ ;

Tab. 4.7: The inner Kronecker products of reps of  $\mathbf{G}$ ; single-valued  $\otimes$  single-valued.

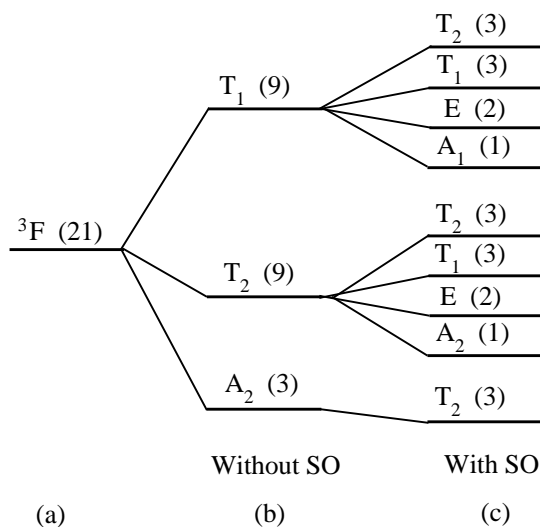


Fig. 4.23: The splitting of a  ${}^3F$  term in  $m'3m'$  symmetry, (a) free atom, (b) crystal field, no spin-orbit coupling, and (c) strong crystal field, weak spin-orbit coupling.

### For the NiO(001) surface

To find the splitting of the  ${}^3F$  term in the magnetic  $4/m'mm$  point group<sup>7</sup> is first determined by the introduction of a strong crystal field. We see from Table 4.8 that; in each of this case the  ${}^3F$  level splits in  $\mathbf{M}$  according to:

$$D\mathcal{D}^3 = DA_2 + DB_1 + DB_2 + 2DE. \quad (4.11)$$

In this case we can see from Table 4.8 for  $S = 1$  that  $\mathcal{D}^S$  is reducible and is given by:

$$\mathcal{D}^1 = A_2 + E \quad (4.12)$$

and

$$D\mathcal{D}^1 = DA_2 + DE \quad (4.13)$$

The inner Kronecker products which are to be reduced are therefore:

$$D\mathcal{D}^1 \otimes DB_1 = \sum_k d_{ij,k} DX_k, \quad (4.14)$$

$$D\mathcal{D}^1 \otimes DE = \sum_k d_{ij,k} DX_k, \quad (4.15)$$

$$D\mathcal{D}^1 \otimes DB_2 = \sum_k d_{ij,k} DX_k \quad (4.16)$$

$$D\mathcal{D}^1 \otimes DA_2 = \sum_k d_{ij,k} DX_k, \quad (4.17)$$

$$D\mathcal{D}^1 \otimes DE = \sum_k d_{ij,k} DX_k \quad (4.18)$$

which since  $\mathcal{D}^1$  is reducible can be considered as the ten products:  $DA_2 \otimes DB_1$ ,  $DE \otimes DB_1$ ,  $DA_2 \otimes DE$ ,  $DE \otimes DE$ ,  $DA_2 \otimes DB_2$ ,  $DE \otimes DB_2$ ,  $DA_2 \otimes DA_2$ ,  $DE \otimes DA_2$ , and  $DA_2 \otimes DE$ ,  $DE \otimes DE$ .

Using Table 4.9 we find that

$$DA_2 \otimes DB_1 = DB_2; DE \otimes DB_1 = DE; \quad (4.19)$$

$$DA_2 \otimes DE = DE; DE \otimes DE = DA_1 + DA_2 + DB_1 + DB_2; \quad (4.20)$$

$$DA_2 \otimes DB_2 = DB_1; DE \otimes DB_2 = DE; \quad (4.21)$$

$$DA_2 \otimes DA_2 = DA_1; DE \otimes DA_2 = DE; \quad (4.22)$$

$$DA_2 \otimes DE = DE; DE \otimes DE = DA_1 + DA_2 + DB_1 + DB_2; \quad (4.23)$$

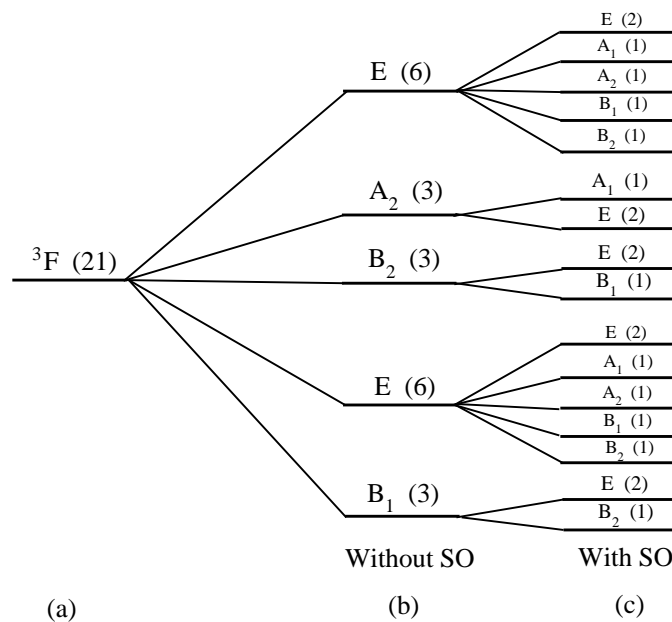
Here, it should be pretty clear, from eq. 4.19 to 4.23, that the splitting of the levels is as shown in Fig. 4.24.

<sup>7</sup> This magnetic point group belongs to the  $C_{4V}$  symmetry in the ordinary point group.

L	G	M
0	$A_1$	$DA_1,$ $1(1)$
1	$A_2 + E$	$DA_2 + DE,$ $1(1) + 1(2)$
2	$A_1 + B_1 + B_2 + E$	$DA_1 + DB_1 + DB_2 + DE,$ $1(1) + 1(1) + 1(1) + 1(2)$
3	$A_2 + B_1 + B_2 + 2E$	$DA_2 + DB_1 + DB_2 + 2DE,$ $1(1) + 1(1) + 1(1) + 2(2)$

Tab. 4.8: The splitting of levels.

Products
$A_1 \otimes A_1 = A_1; A_1 \otimes A_2 = A_2;$
$A_2 \otimes A_2 = A_1; A_1 \otimes B_1 = B_1;$
$A_2 \otimes B_1 = B_2; B_1 \otimes B_1 = A_1;$
$A_1 \otimes B_2 = B_2; A_2 \otimes B_2 = B_1;$
$B_1 \otimes B_2 = A_2; B_2 \otimes B_2 = A_1;$
$A_1 \otimes E = E; A_2 \otimes E = E;$
$B_1 \otimes E = E; B_2 \otimes E = E;$
$E \otimes E = A_1 + A_2 + B_1 + B_2;$

Tab. 4.9: The inner Kronecker products of reps of  $\mathbf{G}$ ; single-valued  $\otimes$  single-valued.Fig. 4.24: The splitting of a  ${}^3F$  term in  $4/m'mm$  symmetry, (a) free atom, (b) crystal field, no spin-orbit coupling, and (c) strong crystal field, weak spin-orbit coupling.

## 4.4.2 Fine structure of the bulk NiO and NiO(001) surface

### Comparison of GAUSSIAN98 and COLUMBUS results

We report in Table 4.10 the comparison of the energies of ground and excited states between GAUSSIAN98 and COLUMBUS codes.

As the Table indicates, we compare these excited states energies of the NiO(001) surface for two codes (GAUSSIAN98 and COLUMBUS). For GAUSSIAN98 results, we obtained these energies for two symmetry systems ( $C_{2v}$  and  $C_{4v}$ ), while COLUMBUS always reduces the high ( $C_{4v}$ ) symmetry in the surface case to the lower ( $C_{2v}$ ) symmetry. All energies were carried out with the same level of theory (CIS approach) and basis sets (6-31G\* for O atom and LanL2DZ ECP for Ni atom).

Comparing the GAUSSIAN98 and COLUMBUS results for  $C_{2v}$  symmetry, it is seen that the excited states energies of Gaussian98 results are a bit lower than the COLUMBUS ones. However, if we compare the total energies of ground states for both codes, the COLUMBUS result in CIS calculation yields basically the slightly lower energy. For the energies in the  $C_{2v}$  case, again, GAUSSIAN98 yields almost the same values compared to the energies from the higher symmetry ( $C_{4v}$ ) one.

As the result, we have concluded that how well the corresponding results of COLUMBUS compare to the results obtained from GAUSSIAN98 code, and the same trends are also observed.

$C_{2v}$		$C_{4v}$		
Symmetry	COLUMBUS	GAUSSIAN98	Symmetry	GAUSSIAN 98
$A_1$	Ground state <sup>†</sup>		$B_1$	Ground state <sup>†</sup>
$B_1$	0.6177	0.5122	$E$	0.5122
$B_2$	0.6177	0.5122	$E$	0.5122
$A_2$	1.0166	0.9603	$B_2$	0.9604
$A_2$	2.0251	1.9571	$A_2$	1.9570
$B_1$	2.6461	2.8638	$E$	2.8638
$B_2$	2.6461	2.8638	$E$	2.8638
$A_1$	7.0290	7.5766	$B_1$	7.5765

Tab. 4.10: The comparison between GAUSSIAN98 and COLUMBUS results.

<sup>†</sup>Ground state energy from GAUSSIAN98 ( $E_0^{UHF} = -1533.54865$  Hr) agrees well with the same of COLUMBUS ( $E_0^{MC-SCF} = -1533.54672$  Hr and  $E_0^{CIS} = -1533.55094$ ). We use the first number as a reference point for GAUSSIAN calculations and the last number as a reference point for COLUMBUS calculations. For Gaussian  $E_0^{UHF} = E_0^{CIS}$ , but for Columbus CIS gives small improvement to the ground state because in MC-SCF methods some restriction were imposed.

### Fine structure of the NiO(001) surface

Figure 4.25 shows the calculated fine structure of the NiO(001) surface. The energy diagram of the corresponding  $3d^8$  levels of the  $\text{Ni}^{2+}$  ion, which are split by the tetragonal-pyramidal crystal field, are reported. We note that our spin-orbit splitting calculation here were carried out at CIS level of theory in COLUMBUS code. For this model employed, C1 symmetry (no symmetry) was selected in order to yield more accurate results in this calculation. Thus, the symmetry of each splitting states is not shown since these contributions can be excluded in a C1 symmetry calculation.

The  ${}^3B_1$  ground state of  $\text{Ni}^{2+}$  is split by spin-orbit coupling into three components, but two levels corresponding one- and two-fold degeneracies, i.e. 0 meV and 3.1 meV, respectively. We should note that we take the zero-level of energy at the lowest energy of these splitting levels. However, this zero-level energy (with spin-orbit interaction) has a slightly different energy from the  ${}^3B_1$  ground state (the zero-level energy without spin-orbit interaction). When spin-orbit interaction is included, the lowest energy equals to  $-22.6$  meV compared to the previous  ${}^3B_1$  ground state (see Fig. 4.25).

The NiO(001) surface has four low-lying excited states such as  ${}^3E$ ,  ${}^3B_2$ ,  ${}^3A_2$ , and  ${}^3E$  in the  $C_{4v}$  crystal field as shown in Fig. 4.25. The splitting of the first  ${}^3E$  excited state is contributed into six components about 602.2, 608.5, 647.1, 665.7, and 689.3 meV for non-degeneracies, except the third one belongs to the twofold degeneracy. Note that these splitting energies are referred to the zero-level energy. The splitting energies based on analytical spin-orbit interaction calculation of the second  ${}^3B_2$  excited state belong to three components of single- and double-degeneracies (both values about 1072.5 and 1083.3 meV for single and double degeneracies, respectively). The splitting energy analysis of the third  ${}^3A_2$  excited state shows three components corresponding to double- and single-degeneracies. Three of them belong to two values of energies (2087.4 meV for double degeneracies and 2172.8 meV for single degeneracy). Finally, the six components of splitting of the last  ${}^3E$  excited state are also shown in Fig. 4.25. Five levels of the splitting energies, about 2947.2, 2967.5, 2968.9, 3005.9, and 3012.9 meV, are found (the first, second, fourth, and fifth values for four non-degeneracies and the third value for twofold degeneracy).

The total energies of all singlet and triplet excited states (only the first 30 excited states) for two systems (with and without the inclusion of spin-orbit interaction) are summaries in Table 4.11.

Of course, we found a good agreement between the calculated fine structure of the NiO(001) surface (see Fig. 4.25) and the atomic splitting energy diagram as illustrated in Fig. 4.24.

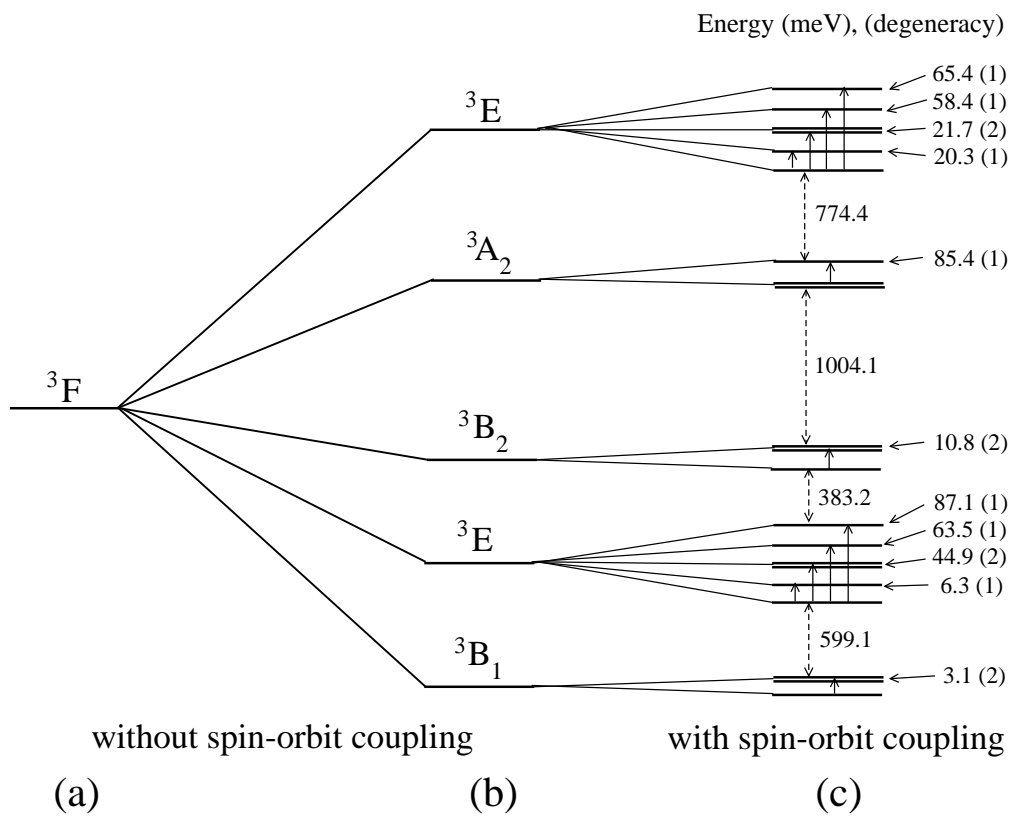


Fig. 4.25: Prediction of the fine structure splittings of the NiO(001) surface.

Multiplicity	Total energy ( $-E_h$ )	
	Without spin-orbit coupling	With spin-orbit coupling
Triplet	1533.5522161461	1533.5530455435
Triplet	1533.5522161460	1533.5529326128
Triplet	1533.5522161444	1533.5529326127
Triplet	1533.5295070994	1533.5309160967
Triplet	1533.5295070991	1533.5306859632
Triplet	1533.5295070981	1533.5292668109
Triplet	1533.5295070960	1533.5292668082
Triplet	1533.5295070956	1533.5285847371
Triplet	1533.5295070951	1533.5277187495
Triplet	1533.5134442576	1533.5136373714
Triplet	1533.5134442571	1533.5132388544
Triplet	1533.5134442559	1533.5132388534
Singlet	1533.4784139459	1533.4814364350
Triplet	1533.4762914842	1533.4763381014
Triplet	1533.4762914825	1533.4763381013
Triplet	1533.4762914816	1533.4732005499
Singlet	1533.4684593593	1533.4687544444
Triplet	1533.4434107487	1533.4447422659
Triplet	1533.4434107481	1533.4439963855
Triplet	1533.4434107449	1533.4439455107
Triplet	1533.4434106957	1533.4439454762
Triplet	1533.4434106953	1533.4425853798
Triplet	1533.4434106921	1533.4423289269
Singlet	1533.4428606084	1533.4421790127
Singlet	1533.4428605995	1533.4421789980
Singlet	1533.4322371179	1533.4321585998
Singlet	1533.4248860301	1533.4246172709
Singlet	1533.3980478598	1533.3979995534
Singlet	1533.3980478522	1533.3979995470
Singlet	1533.3750945883	1533.3748138969

Tab. 4.11: The computed total energies for 30 singlet and triplet excited states with and without spin-orbit coupling effects.

## Fine structure of bulk NiO

Although the electronic structure of the bulk NiO is much simpler than that of the surface, the Configuration Interaction calculations are considerably more demanding due to the larger number of basis function and, thus, higher dimension of the Hamiltonian matrix<sup>8</sup>. In the Table 4.12 we compare the parameters of the CIS calculations for both systems.

System	$N_{\text{docc}}$	$N_{\text{act}}$	$N_{\text{virt}}$	$H_{\text{CIS}}$ size		
				CIS <sub>Triplet</sub>	CIS <sub>Singlet</sub>	CIS+SO
(NiO <sub>5</sub> ) <sup>8-</sup>	32	2	33	3299	4357	20590
(NiO <sub>6</sub> ) <sup>10-</sup>	37	2	37	5627	4256	26609

Tab. 4.12: Parameters of CIS calculations:  $N_{\text{docc}}$  is the number of double occupied states,  $N_{\text{act}}$  – number of active states,  $N_{\text{virt}}$  – virtual states. Note that the size of Hamiltonian matrix is proportional to the product of numbers of occupied and virtual states.

Figure 4.26 shows the calculated fine structure of the bulk NiO. For the comparison with the experimental results of optical properties, the measurements are shown as a reference point in the Fig. 4.27.

There are several observations about the role of spin-orbit coupling. Firstly, its inclusion leads to a slight lowering of the ground state energy ( $E_{3A_2}$ (without SOC)– $E_{T_2}$ (with SOC)=48 meV). We should note that the corresponding symmetry of each level is taken from the reference scheme (Fig. 4.23). The broadening of the second excited state ( $\Delta E_{3T_2} = E_{E_2} - E_{A_2} = 71.3$  meV) ( ${}^3T_2$ ) agrees well with the most accurate measurements (around 70 meV) of the optical absorption and second harmonic generation spectra of NiO (Fig. 4.27). However, the important differences have been observed. The assignment of the levels to the peaks in the optical absorption spectra from Fiebig *et al.* [17] shows almost equal distance among the sub-levels of the  ${}^3T_2$  state. Very narrow splitting of the first sublevel  $E_2$  is approximately 51 meV and is attributed to the exchange field breaking of the symmetry. In contrast, our calculation shows very small distance between the second and the first, and forth and third sublevels (7.8 meV, 9.5 meV). Therefore, we argue that two sharp lines in the optical absorption spectra may also result solely from the spin-orbit coupling.

The computations of the second excited state is clearly less precise due to the importance of the correlated effects (QCISD(T) lowers its energy by 0.64 eV compared to the CIS). However, we expect that it should not affect the fine structure of the level much. The experimental resolution does not allow to clearly distinguish among the participating states, and we restrict ourselves with the remark that the broadening ( $\Delta E_{3T_1} = E_{A_1} - E_{T_2} = 55.4$  meV) is in agreement with the experimental width of  ${}^3\Gamma_2^+ \rightarrow {}^3\Gamma_4^+$  band. However, the relative position of the sub-levels differs from that proposed in the theoretical work by Ferguson and Guggenheim [119].

<sup>8</sup> For the system with two unpaired electrons the size of the CIS Hamiltonian can be expressed as a function of the number of double occupied states ( $N_{\text{docc}}$ ) and virtual states ( $N_{\text{virt}}$ ) as :  $N_{\text{CIS}_{\text{Triplet}}} = 1 + 2(N_{\text{docc}} + N_{\text{virt}}) + 3N_{\text{docc}}N_{\text{virt}}$ ,  $N_{\text{CIS}_{\text{Singlet}}} = 3 + 2(N_{\text{docc}} + N_{\text{virt}}) + 4N_{\text{docc}}N_{\text{virt}}$ ,  $N_{\text{CIS}_{\text{Triplet}}} = 6 + 8(N_{\text{docc}} + N_{\text{virt}}) + 19N_{\text{docc}}N_{\text{virt}}$  It means that increasing the number of atoms in the system in 2 times leads to the expansion of the CIS matrix in 4 times. This, in turn, increases computational time for the diagonalization by  $4^3 = 64$ .

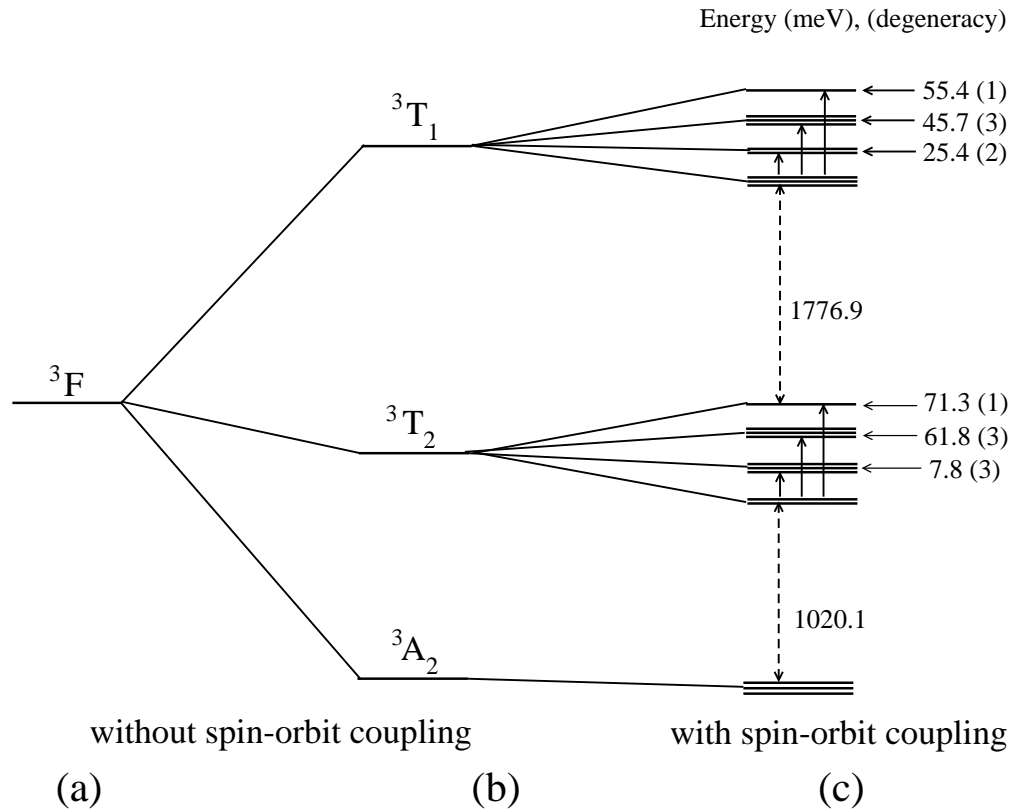


Fig. 4.26: Prediction of the fine structure splittings of the bulk NiO.

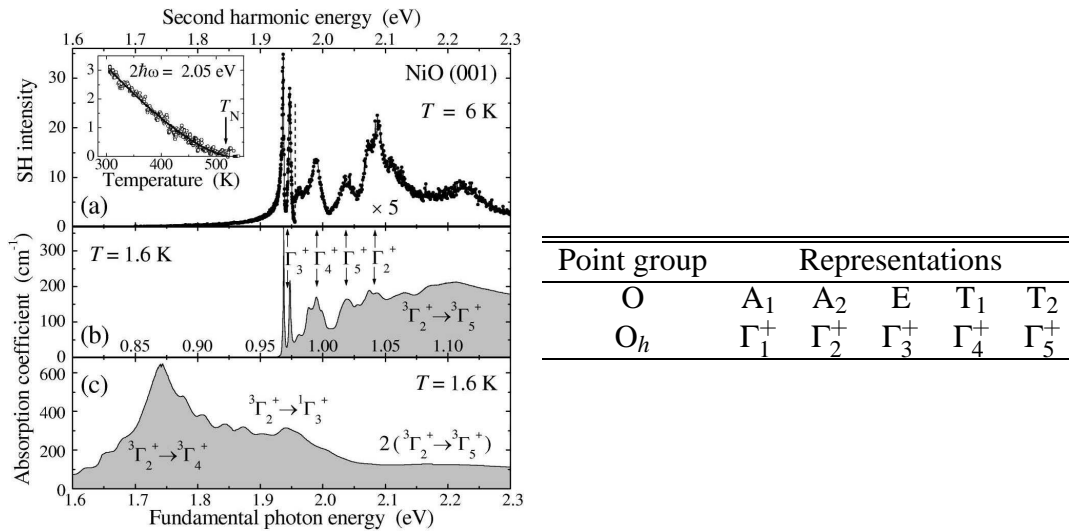


Fig. 4.27: Left panel: second harmonic and optical absorption spectra of NiO in the region of the lowest  $3d^8$  electronic transitions with incident and emitted [001]-polarized light. The result of Fiebig *et al.* [17]. Right panel: correspondence between different schemes for the representations of group  $O_h$  ( $O_h = O \otimes C_i$ ).

## 4.5 SHG intensity

We compute the frequency dependence of the nonlinear susceptibility tensor  $\chi_{ijk}^{(2\omega)}(\omega)$  based on two different levels of the treatment of correlations: CID and QCISD with a triples correction. As can be seen from Eq. (3.57), the notion of wave functions as well as the energies of the states is required. The former give rise to the dipole transition matrix elements, which control the symmetry properties of the spectrum (selection rules) as well as the magnitude of the peaks. The knowledge of the energies is necessary to get the correct position of the peaks. In order to avoid divergences of the expression close to the poles and to ensure the correct symmetry we apply a broadening of  $\delta = 0.27$  eV (i.e., 0.01 hartree) to each of the states. The transition matrix elements  $\langle \alpha | d_i | \beta \rangle$  have been computed based on the Slater determinants corresponding to each of the many-body wave functions Eq. (3.58), thus neglecting the correction resulting from the virtual transitions (second and third terms in Eq. (3.21)). This correction is important to describe the energy of excited states and is taken properly into account, while for the matrix elements it does not play a crucial role. As we do not include spin-orbit coupling here, the dipole matrix elements contain two independent contributions from spin-up and spin-down components. Important features of the SHG spectrum (Fig. 4.28) are the following:

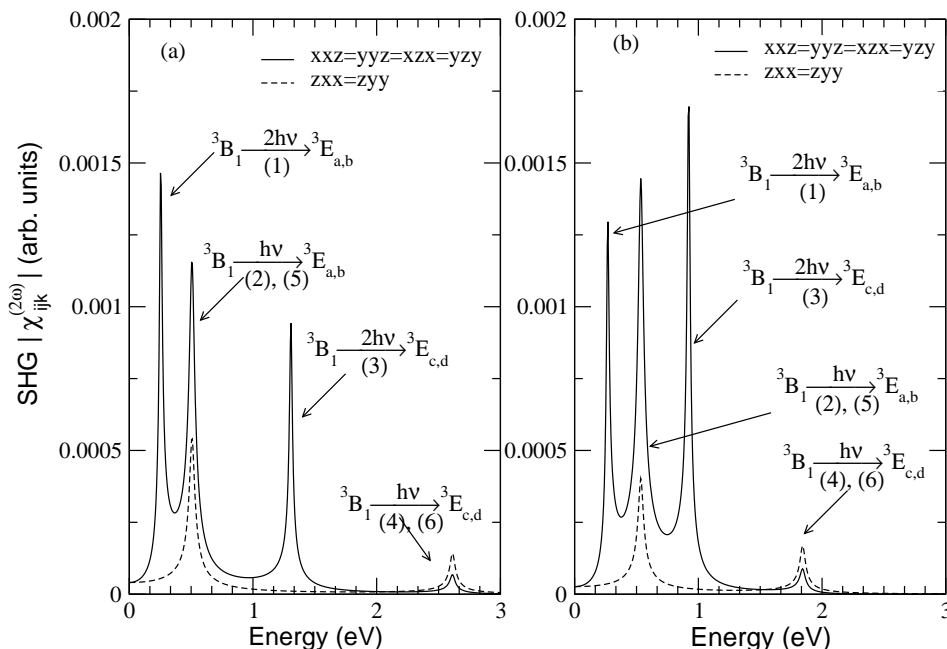


Fig. 4.28: The nonlinear SHG spectrum of the NiO(001) surface cluster. (a) CID method (b) QCISD(T) method. Note that the  ${}^3E_{a,b}$  and  ${}^3E_{c,d}$  are doubly degenerate excited states corresponding to the energies of 0.51 eV (0.53 eV) and 2.61 eV (1.84 eV) in CID (QCISD(T)), respectively. Corresponding transitions are explained on Fig.5 together with the energy scheme. The second numbers under the arrows correspond to the dashed curves.

1. Large difference between the tensor elements: the peaks around 0.35 eV and 0.95 eV are

well pronounced only for  $|\chi_{xxz}^{(2\omega)}|$  ( $=|\chi_{yyz}^{(2\omega)}|=|\chi_{xzx}^{(2\omega)}|=|\chi_{yzy}^{(2\omega)}|$ ), while they are absent for  $|\chi_{zxx}^{(2\omega)}|=|\chi_{zyy}^{(2\omega)}|$ . The tensor element  $\chi_{zzz}^{(2\omega)}$ , despite it is not forbidden by the selection rules, is accidentally absent in the present theory because of the small number of excited states included in our calculation.

2. The SHG spectrum originates from all possible combinations of ED transitions between the ground state ( ${}^3B_1$ ) and the two doubly degenerate states of  ${}^3E$  symmetry (see Fig. 4.29). Two peaks in the  $\chi_{zxx}^{(2\omega)} = \chi_{zyy}^{(2\omega)}$  result from the transitions at fundamental frequency  $\omega$  from  ${}^3B_1$  to  ${}^3E_{c,d}$  and from  ${}^3E_{a,b}$  to the ground state. The second type of tensor elements has two additional peaks that correspond to  $2\hbar\omega$  resonances between these levels.
3. The nonvanishing tensor elements have a nonzero value in the static limit and exhibit Kleinman symmetry [120] with respect to the permutation of the  $2\omega$  and  $\omega$  photons:

$$|\chi_{ijk}^{(2\omega)}| = |\chi_{jik}^{(2\omega)}| = |\chi_{kji}^{(2\omega)}| \text{ for } \omega \rightarrow 0 \quad (4.24)$$

4. Comparing SHG spectra from CID and QCISD(T) methods, a shift towards lower energies resulting from the higher-level treatment of the correlation can be observed.

Using the nonlinear susceptibility tensor, we compute the intensity of the second-harmonic field (Figs. 4.30, 4.31) according to Eq. (3.61) for different combinations of the polarization of the incident light at the fundamental frequency (for s-polarization  $\varphi = \pi/2$  and for p-polarization  $\varphi = 0$ ) and outgoing second-harmonic light (for S-polarization  $\Phi = \pi/2$  and for P-polarization  $\Phi = 0$ ). The input electric field is taken to be  $10^8$  V/m, angle of incidence is  $\pi/4$ , and the complex refractive indices at the frequencies of the fundamental incident and outgoing second-harmonic are  $n(\omega)$  and  $N(2\omega)$ , respectively. Although available from the first-principles calculation on the different levels of theory [121],  $n(\omega)$  and  $N(2\omega)$  are taken from experiment [40] in order to make the results more reliable and to avoid artifacts from linear optics. According to the symmetry analysis, the second harmonic signals in S-polarization vanish, and our calculations confirm that, numerically showing a difference in the magnitude between S- and P-polarizations to be 33 orders of magnitude (Figs. 4.30, 4.31).

It is well known that the SHG response is forbidden for crystals with inversion symmetry within the ED processes. However, taking into account a combination of the MD and ED processes, one can indeed obtain a second harmonic response from centrosymmetric NiO in the energy range  $2\hbar\omega = 1.6 - 2.3$  eV [17]. The absence of the SHG signal above the Néel temperature and selection rules that define the polarization of the observed signal prove that there is no surface contribution in the experiment. In the ED calculation, no SHG intensity is found from the  $(\text{NiO}_6)^{10-}$  cluster in the cubic lattice.

Our calculation shows the possibility to obtain second harmonic response from the surface cluster in the range of energies  $2\hbar\omega = 1.06 - 3.68$  eV. This response lies in the region of energies, where the bulk SHG signal has been detected. Thus, under certain conditions, the SHG signal from the surface, which is expected to be considerably weaker, as well as from the

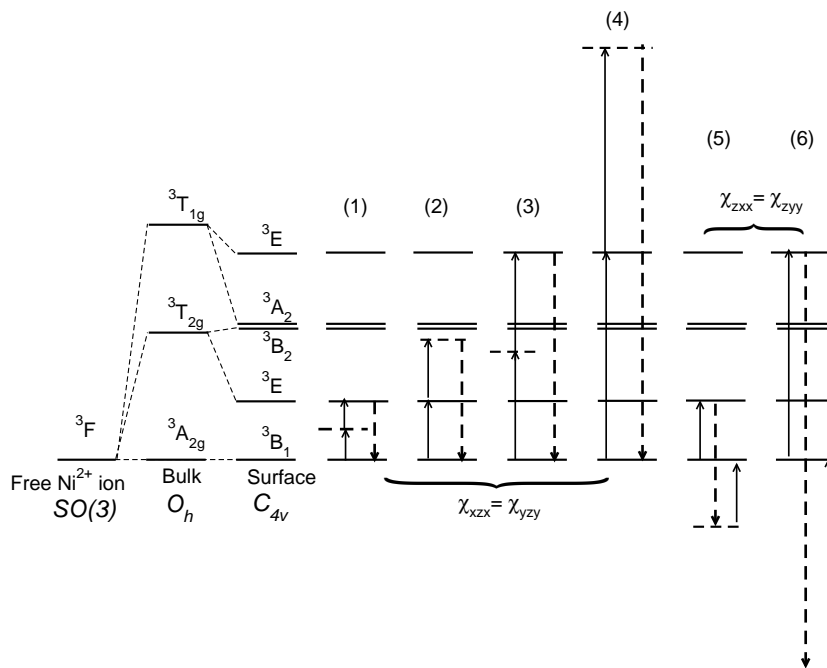


Fig. 4.29: Energy level scheme of  $\text{Ni}^{2+}$  ion in different symmetry environments. The vertical lines denote allowed ED transitions involved in the SHG spectrum (dashed lines correspond to the  $2\omega$  transitions). The  ${}^3E$  states are doubly degenerate and correspond to the  ${}^3E_{a,b}$  and  ${}^3E_{c,d}$  excitations in Fig. 4.28. The transitions are numbered according to the Fig. 4.28.

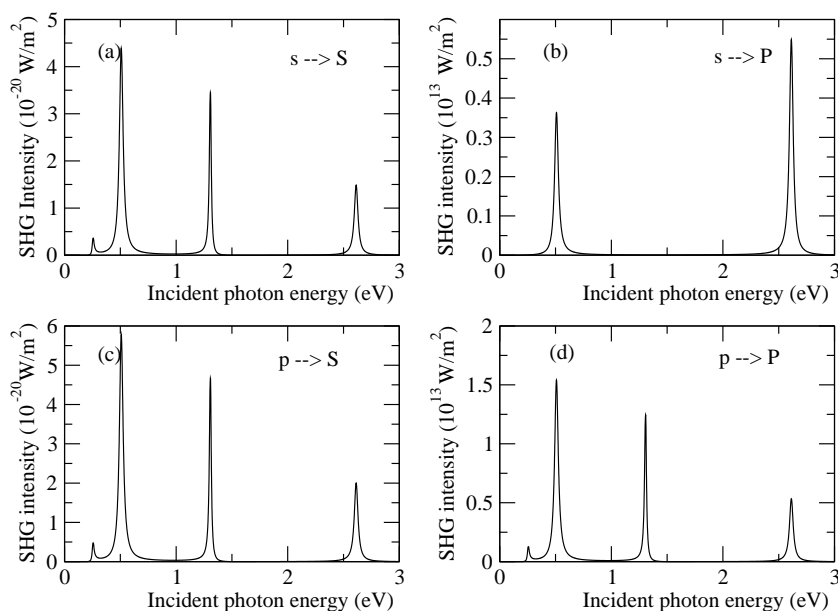


Fig. 4.30: The nonlinear optical response of NiO(001) surface, based on the CID treatment of the embedded  $(\text{NiO}_5)^{8-}$  cluster as a function of the incident photon energies for the four possible combinations of the input field and detector.

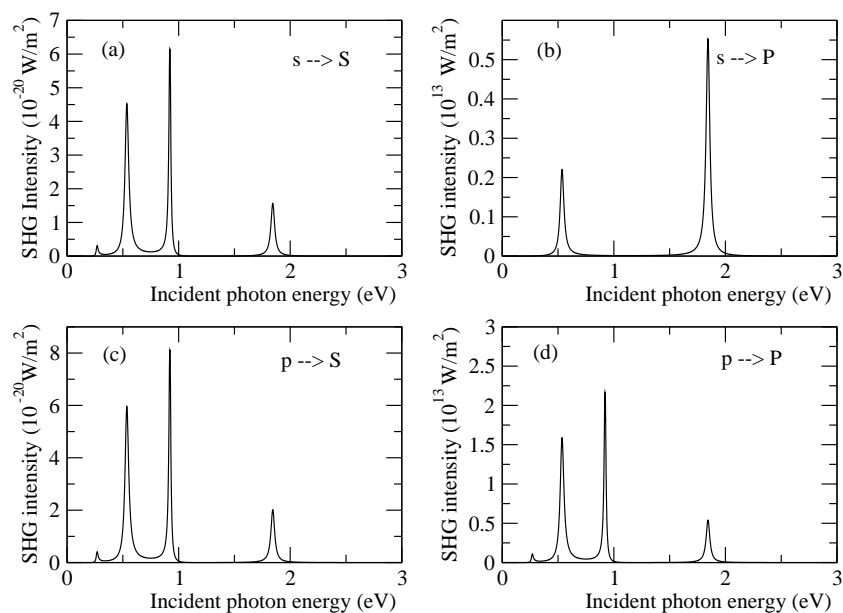


Fig. 4.31: The nonlinear optical response of NiO(001) surface, based on the QCISD(T) treatment of the embedded  $(\text{NiO}_5)^{8-}$  cluster as a function of the incident photon energies for the four possible combinations of the input field and detector.

bulk, can be observed in one experiment. In the recent investigation by Fiebig *et al.* [17], 3 ns light pulses with a pulse energy of about 1 mJ were applied to detect SHG response from the bulk. Although the MD transitions were involved, the intensity is comparable to that observed in non-centrosymmetric compounds such  $\text{Cr}_2\text{O}_3$  or  $\text{YMnO}_3$  where it is exclusively due to ED transitions. Therefore, a larger peak intensity of fundamental light is required to detect SHG response from the surface on the background of the bulk signal. Shorter laser pulses may enable the detection of both surface and bulk contribution in one experiment.



# Chapter 5

## Conclusions

NiO is a very interesting and complicated physical system. The combination of electronic and magnetic properties makes it a unique material with a wide range of applications, first of all for magnetic recording and as a building element of memory chips.

The first question about the electronic structure for which solid state physicists would like to have an answer is the value of the band gap. None of the present *ab initio* theories is able to answer this question with a high degree of precision. The problem is electronic correlations. Common spread density functional theory for the investigation of the electronic structure of solids fails in this case. It happens because it is by the definition a single-particle theory that does not fully cover the many-body nature of the problem. It was shown that two-body effects are important for NiO. Novel methods such as the GW approximation and numerical solution of the Bethe-Salpeter equation give a promising route for accounting two-body correlations. But even these methods are not capable to give a complete answer about the electronic structure. The material possesses a number of intragap states resulting from the partially filled *d*-shells of the Ni atom. In our work we have chosen a quite different route to tackle both of the problems: getting knowledge about the electronic structure and computing states inside the band gap by means of quantum chemistry methods.

One may wonder how these methods initially developed for predicting properties of small molecules can be applied for the bulk or surface materials which are translationally invariant and contain, roughly speaking, an infinite number of atoms. The main idea is to choose a sufficient large part of the bulk or surface under investigation and consider it as a cluster with a limited number of atoms for which quantum chemistry theory can already be applied. The question immediately arises: what we can call sufficiently large cluster. It is realistic to assume that its size must be big that the addition of few more atoms at the edges of the cluster does not change the electronic structure significantly. In our work, we found that it is sufficient to consider the  $(\text{NiO}_6)^{10-}$  cluster ( $O_h$  symmetry) embedded in a set of point charges in order to model bulk NiO, and the embedded  $(\text{NiO}_5)^{8-}$  cluster ( $C_{4v}$  symmetry) represents the NiO(001) surface fairly well. However, to correctly take into account the ionic environment surrounding the clusters in real materials we must add more building elements to our construction: effective core potentials and point charges. Their inclusion helps to describe the interaction of the electrons of the cluster with neighbouring atoms and corrects for the total charge and Madelung potential. Experimenting with different number of point charges we built our two

models for the bulk and surface NiO. The  $\text{NiO}_6^{10-}$  cluster is embedded into a  $15 \times 15 \times 15$  slab of point charges while for the  $\text{NiO}_5^{8-}$  the configuration  $15 \times 15 \times 7$  is the best choice. The point charges have values  $\pm 2, \pm 1, \pm 0.5$  and  $\pm 0.25$  depending on their position. As more simple surface models we consider also  $11 \times 11 \times 5, 7 \times 7 \times 3$  clusters and compare their electronic properties in order to determine the optimal size. Since our work has as a final target the optical properties of NiO for the technological application we investigate intra-gap states by means of a variety of quantum chemistry methods. Two quantum chemistry programs were used: GAUSSIAN98 and COLUMBUS. Although they are based on the same theoretical ideas, namely different levels of the Configuration Interaction, the numerical implementation imposes different routes to compute the properties of excited states. We build our calculations with GAUSSIAN98 in following way. First the electronic structure of the ground state is determined by means of unrestricted Hartree-Fock calculation (the ground state is triplet). A number of electronic properties can be determined already on this level of theory. To this belongs Mulliken population analysis and the distribution of the magnetic moments among the atoms. The examination of the molecular orbitals gives hints for the further Configuration Interaction calculation of the excited states. We obtain the symmetry of the bulk NiO ground state to be  ${}^3A_{2g}$  and the (001) surface NiO ground state is  ${}^3B_1$ . Starting from the ground states, we compute a large number of triplet excited states on the simplest 'Configuration Interaction Singles' level of theory. By analyzing the symmetry of these states and employing the assumption about the charge transfer character of the gap, we determine the optical surface gap to be around 7.6 eV. Furthermore the energies of the lowest excited states have to be computed using more sophisticated and precise methods such as CISD and QCISD(T). In contrast to the COLUMBUS program that allows to find an arbitrary number of states by iteratively diagonalizing the Hamiltonian matrix on a certain subspace (single and double substitutions) the GAUSSIAN98 code, although providing an even higher level treatment of correlations partially taking into account triple substitutions and making quadratic corrections, only gives the possibility to compute one eigenvalue. Therefore, in order to obtain several low-lying excited states we first build them on the mean field level by exciting an electron from one of the occupied states to a virtual one and optimizing the electronic configuration by UHF. The knowledge of orbital symmetry obtained on the prior ground state calculation provides the information about the presumable electronic configuration of the states of interest. In this way many excited states can be found provided we know the major single determinant contribution (which orbitals to exchange) to their electronic structure. On the next step we improve the energy of these states by accounting electronic correlations by means of configuration interaction method. We employ several levels of theory starting from the relatively simple CID and using QCISD(T) as the most sophisticated and accurate method. Comparison of energies resulting from each level of theory reveals that the inclusion of the triple excitations gives a superior improvement over the CISD, supports the initial assumption about the importance of many-body correlations and leads to accurate agreement with experiment. Thus, by employing the GAUSSIAN98 quantum chemistry program we completely describe the crystal field splitting of the  ${}^3F$  term of  $\text{Ni}^{2+}$  ion in the cubic and  $C_{4v}$  environment. This gives us the possibility to predict non-linear optical properties of the material such as second harmonic generation. Our SHG spectrum for the (001) surface can be compared with experi-

---

ment providing an alternative explanation of the possibility of detecting SHG signal from the crystal with inversion symmetry (Non-linear response is forbidden for (001) surface of the centrosymmetric NiO crystal). It was argued that the SHG response in NiO results from the combination of the magnetic dipole and quadruple transitions. We suggest that this can also be due to the symmetry breaking on the surface of the crystal. In order to make our knowledge about NiO complete, we also have to consider relativistic effects not taken into account in GAUSSIAN98 computations. The COLUMBUS code is a convenient tool for that purpose. Using this program we were able to accurately describe the spin-orbit coupling (the major relativistic effect) using the CIS level of theory and spin-orbit effective potential for the Ni atom. For each of the levels originating from the  $^3F$  states of the free  $Ni^{2+}$  ion we computed the spin-orbit splitting.

Thus, in our work we completely describe low-lying triplet states of NiO for both bulk and surface regions. The material has still a lot to be discovered. Our next target is computation of the singlet states and states with higher energy and increasing our knowledge about the optical properties of this material.



# Appendices

## A Basis sets and effective core potentials used in calculations

Here, we describe basis functions and effective core potentials used throughout the work. Basis functions reside on each of the atom  $R_a$  and have a radial part depending on the relative distance from the atomic center  $r_0 = |r - R_a|$  and an angular part that depends on the two angles  $\Theta$  and  $\phi$ . There are two possibilities how the angular part can be represented: one uses spherical or Cartesian basis functions. Spherical Gaussian basis functions of the orbital moment  $L$  containing  $k$  contracted gaussians can be represented in the following form:

$$\phi(r) = Y_{L,m}(\Theta, \phi) r_0^L \sum_{i=1}^k c_i e^{-\alpha_i r_0^2}, \quad (\text{A.1})$$

while Cartesian Gaussian basis functions are:

$$\phi(r) = x_0^{n_x} y_0^{n_y} z_0^{n_z} \sum_{i=1}^k c_i e^{-\alpha_i r_0^2}. \quad (\text{A.2})$$

In these forms,  $r_0 = (x_0, y_0, z_0)$ ,  $n_x + n_y + n_z = L$ ,  $Y_{L,m}(\Theta, \phi)$  are spherical harmonics of orbital momentum  $L$ ,  $c_i$  are contraction coefficients, and  $\alpha_i$  are corresponding exponents.

The simplest polarization basis set, termed 6-31G\*, is a representation originally proposed by Hariharan and Pople [75] for the first-row atoms and later extended to second-row elements. Polarization functions are needed: (a) in order to describe accurately the electron density in the molecule, where the symmetry is much lower than in atom, and (b) to describe the response of the electron density to an external field [122]. The 6-31G\* basis set is constructed by the addition of a set of six second order ( $xx, yy, zz, xy, xz, yz$ ,  $d$ -type) gaussian primitives to the split-valence 6-31G basis set description of each heavy (non-hydrogen) atom. The 6-31G\* basis contains no provision on hydrogen and helium atoms. Thus, a  $d$ -exponent, chosen on the basis of O atom, is a polarization function as given in Table .1.

The 6-31+G\* basis set for second-row element are constructed from the underlying 6-31G\* representation by the addition of a single set of diffuse gaussian  $s$ - and  $p$ -type functions. The gaussian exponents for both  $s$ - and  $p$ -functions, which are displayed in Table .1, have been determined for second-row elements, for example O atom.

It is important to remark the use of two completely different types of basis sets throughout this work. In addition, the LanL2DZ basis set utilising a double zeta description for the first-row elements and an effective core potential (ECP) for heavier atoms has been employed.

It was known for a long time that core (inner) orbitals are in most cases not affected significantly by changes in chemical bonding. This prompted the development of Effective Core Potential (ECP) approach, which allows treatment of inner shell electrons as if they were some averaged potential rather than actual particles. ECP's are not orbitals but modifications to a Hamiltonian, and as such are very efficient computationally. Also, it is very easy to incorporate relativistic effects into ECP (this is described in the next section), while all-electron relativistic computations are very expensive. The relativistic effects are very important in describing heavier atoms, and luckily ECPs simplify calculations and at the same time make them more accurate with popular non-relativistic *ab initio* packages. The core potentials can only be specified for shells that are filled. For the rest of electrons (i.e. valence electrons), one has to provide basis functions. These are special basis sets (such as LanL2DZ) optimized for the use with specific ECPs.

The ECP are tabulated in the literature as parameters of the following expansion:

$$U_{\text{ECP}}(r) = \sum_{i=1}^k d_i r_0^{n_i} e^{-\zeta_i r_0^2}, \quad (\text{A.3})$$

where  $k$  is the number of terms in the expansion,  $d_i$  is a coefficient for each term, as before  $r_0$  denotes distance from nucleus,  $n_i$  is a power of  $r_0$  for the  $i$ -th term, and  $\zeta_i$  represents the exponent for the  $i$ -th term. To specify ECP for a given atomic center, you need to include typically: the number of core electrons that are substituted by ECP, the largest angular momentum quantum number included in the potential, and number of terms in the 'polynomial gaussian expansion' shown above.

At present, the ECP methods are extensively used in *ab initio* calculations on molecules and crystals containing heavy atoms. One of the reasons for this is the computational saving associated to the valence-only approximation, but other advantages of the ECP methods are responsible for this as well. In the Table .1 we collected the information about the 6-31G\* basis functions for the O atom and LanL2DZ basis set for Ni atom.

## B The relativistic effective core potentials

Relativistic effects are known to be very important in the physics and chemistry of the heavy elements. Although they already manifest themselves in some properties of light elements, when it comes to molecules and solids containing elements of high Z, the relativistic effects become essentially a must for any property<sup>1</sup>.

<sup>1</sup> The strength of spin-orbit coupling can be estimated using a hydrogen atom as a model. For the case of a single electron outside the nucleus, the Dirac theory gives  $\Delta T = \frac{R\alpha^2 Z^4}{n^3} \frac{j(j+1) - l(l+1) - s(s+1)}{l(2l+1)(l+1)}$  for the spin-orbit correction to the term. Here  $n, l, j, s$  are principle, orbital, total momentum and spin quantum numbers.  $\alpha \sim 1/137$  is called the fine structure constant. One sees that the strength of this relativistic effect increases proportionally to the forth power of nucleus charge.

The relativistic effective potentials (REPs) were proposed by Christiansen *et al.* [123] and subsequently generalized to include relativity using the methodology developed by Lee, Ermler and Pitzer [124]. Briefly, the basic equation in this framework is the Dirac equation, which substitutes for the Schrödinger equation. In it, the one-electron wave functions, called spinors, are vectors made of four components, each complications appear as a consequence of this. One first solves the Dirac-Hartree-Fock (DHF) equations to obtain four-component atomic spinors. The four-component valence spinors,  $\phi_{lj}$ , are then transformed to two components,

$$\chi_{lj} = \phi_{lj} + F_{lj}, \quad (\text{B.4})$$

where  $F_{lj}$  is itself a four-component spinor with large components that cancel the radial core-like oscillations in the large components of the  $\phi_{lj}$ , but small components that completely cancel those of the  $\phi_{lj}$ . The two-component pseudospinor,  $\chi_{lj}$ , is then effectively reinserted into the DHF equation and the equation inverted to obtain the localized relativistic effective potential,  $U_{lj}^{REP}$ . The total REP could then be written as an infinite expansion of the  $U_{lj}^{REP}$ , each with the appropriate projection operators. In practice, of course, the expansion is truncated at the lowest angular momentum value,  $L$ , for which there are no longer any core-like oscillations in the large component of  $\phi_{Lj}$ . That is, the large components of  $F_{Lj}$  disappear. Due to the minimal exchange interaction between the core and higher  $l$  spinors and the absence of the  $F_{lj}$  large components for all  $l$  greater than  $L$ , this truncation is an excellent approximation. For use in conventional codes, the REPs are then averaged and differentiated for each  $l$  to form the corresponding averaged relativistic effective potentials (AREP) along with spin-orbit operators (SO).

Averaged relativistic effective potentials with effective spin-orbit operators from Christiansen and coworkers [125, 126, 127, 128, 129] are derived here as Gaussian expansions,

$$U_l^{AREP(SO)} = r^{-2} C_{li} r^{n_{li}} \exp(-\zeta_{li} r^2) \quad (\text{B.5})$$

as originally proposed by Kahn *et al.* [130]. As such the AREP can be used without modification in standard software such as the COLUMBUS program package.

While the molecular small components are not treated explicitly in the shape consistent REP formalism, the small components, along with the core oscillations, are included in the effective potential through the pseudospinor transformation and subsequent Fock equation inversion. Indeed, implicit variation of the small components in subsequent molecular environments is allowed by means of the projection operators.

Atom	Name	Number	Type	Exponent	Contracted coefficients			
O	6-31G*	6	S	5484.67170	0.183110000E-02			
				825.234950	0.139501000E-01			
				188.046960	0.684451000E-01			
				52.9645000	0.232714300			
				16.8975700	0.470193000			
				5.79963530	0.358520900			
		3	SP	15.5396160	-0.110777500	0.708743000E-01		
				3.59993360	-0.148026300	0.339752800		
				1.01376180	1.13076700	0.727158600		
		1	SP	0.270005800	1.00000000	1.00000000		
				1	D	0.800000000	1.00000000	
		O	6-31+G*	6	S	5484.67170	0.183110000E-02	
						825.234950	0.139501000E-01	
188.046960	0.684451000E-01							
52.9645000	0.232714300							
16.8975700	0.470193000							
5.79963530	0.358520900							
3	SP			15.5396160	-0.110777500	0.708743000E-01		
				3.59993360	-0.148026300	0.339752800		
				1.01376180	1.13076700	0.727158600		
1	SP			0.270005800	1.00000000	1.00000000		
				1	SP	0.845000000E-01	1.00000000	1.00000000
1	D			0.800000000	1.00000000			
Ni	LanL2DZ	3	S	7.62000000	-0.408255000			
				2.29400000	0.745530800			
				0.876000000	0.532572100			
				4	S	7.62000000	0.187259100	
						2.29400000	-0.396696400	
						0.876000000	-0.495400300	
		1	S	0.115300000	1.08443430			
				0.396000000E-01	1.00000000			
		3	P	23.6600000	-0.481558000E-01			
				2.89300000	0.625847300			
				0.943500000	0.471515800			
		1	P	0.840000000E-01	1.00000000			
				1	P	0.240000000E-01	1.00000000	
		4	D	42.7200000	0.372699000E-01			
				11.7600000	0.195610300			
				3.81700000	0.456127300			
1.16900000	0.562158700							
1	D			0.283600000	1.00000000			

Tab. .1: The 6-31G\* (also 6-31+G\*) and LanL2DZ basis sets for O and Ni atoms, respectively.

Atom	Name	Number	Type	Exponent	Contraction		
Ni	ECP	3	$d$ potential	469.93243310	-10.00000000		
				85.42364110	-69.40848050		
				21.26749840	-12.09510200		
		4	$s-d$ potential	162.16860970	3.00000000		
				176.53332320	22.02536180		
				68.95620100	443.01810880		
		4	$p-d$ potential	13.57928380	145.56964110		
				69.01815060	5.00000000		
				275.59555960	4.98828240		
				47.13154530	256.69458530		
				12.98740750	78.47544500		
Mg	ECP	5	$d$ potential	237.54848040	-10.00000000		
				47.75203670	-55.89939680		
				10.78378520	-20.13919570		
		5	$s-d$ potential	3.19921240	-7.06791070		
				1.06369530	-0.81331090		
				348.30086310	3.00000000		
		6	$p-d$ potential	59.46801330	44.00756600		
				19.07675820	107.38613440		
				5.29656130	35.82890880		
				1.38673730	10.11434350		
				1256.87390850	5.00000000		
				189.86088390	117.10536720		
		Ni	SO	6	$p-d$ potential	54.69496310	420.59720730
						13.89901370	107.61229590
						3.95971810	29.10025760
						1.25527870	7.08755700
						0.265300	0.000768
						1.509200	5.356128
5	$d$ potential			1.812800	-11.295932		
				2.212000	6.144546		
				5.485600	-0.276856		
		7.518900	0.024518				
		0.604700	-0.003842				
		1.937000	0.012924				
		5.494600	-0.005573				
		18.089500	0.021615				
		53.189400	0.122379				

Tab. .2: The effective core potential (ECP) for Ni and Mg atoms and the spin-orbit operator (SO) suitable for Ni atom in spin-orbit coupling calculation.



# Bibliography

- [1] H. Fukuyama and N. Nagaosa. Physics and chemistry of transition-metal oxides. *Springer Series in SOLID-STATE SCIENCES*, 1999.
- [2] B. Fromme. d-d excitations in transition-metal oxides. *A spin-polarized Electron Energy-Loss Spectroscopy (SPEELS) Study, Springer Tracts in Modern Physics*, 170:1, 2001.
- [3] N. F. Mott. *Proc. Phys. Soc., Sect. A*, 62:416, 1949.
- [4] D. Adler and J. Feinleib. *Phys. Rev. B*, 2:3112, 1970.
- [5] B. H. Brandow. *J. Solid State Chem.*, 12:397, 1975.
- [6] B. Koiller and L. M. Falicov. *J. Phys. C*, 7:299, 1974.
- [7] A. B. Kunz and G. T. Surratt. *Solid state commun.* 25:9, 1978.
- [8] A. B. Kunz. *Int. J. Quantum Chem., Symp.*, (15):487, 1981.
- [9] F. Gebhard. Mott metal-insulator transition: models and methods. *Springer-Verlag, Berlin, Germany.*, page 330, 1997.
- [10] K. Terakura, A. R. Williams, T. Oguchi, and J. Kübler. *Phys. Rev. Lett.*, 52:1830, 1984.
- [11] J. Zaanen, G. A. Sawatzky, and J. W. Allen. *Phys. Rev. Lett.*, 55:418, 1985.
- [12] S. Hüfner. *Solid State Commun.*, 49:1177, 1984.
- [13] I. Pollini, J. Thomas, G. Jezequel, J. C. Lemonnier, and A. Lenseink. *Phys. Rev. B*, 29:4716, 1984.
- [14] P. A. Cox. Transition metal oxides: An introduction to their electronic structure and properties. *Clarendon Press, Oxford*, 1995.
- [15] J. de Boeck and G. Borghs. *Phys. World*, 12:27, 1999.
- [16] M. Fiebig, D. Fröhlich, B. B. Krichevstov, and R. V. Pisarev. *Phys. Rev. Lett.*, 73:2127, 1994.

- [17] M. Fiebig, D. Fröhlich, Th. Lottermoser, V. V. Pavlov, R. V. Pisarev, and H.-J. Weber. *Phys. Rev. Lett.*, 87:137202, 2001.
- [18] A. Dähn, W. Hübner, and K. H. Bennemann. *Phys. Rev. Lett.*, 77:3929, 1996.
- [19] K. H. Bennemann. Nonlinear optics in metals. *Clarendon Press, Oxford*, 1998.
- [20] S. Hüfner and G. K. Wertheim. *Phys. Rev. B.*, 8:4857, 1973.
- [21] A. I. Lichtenstein and M. I. Katsnelson. *Phys. Rev. B*, 57:6884, 1998.
- [22] F. Aryasetiawan and O. Gunnarsson. *Phys. Rev. Lett.*, 74:3221, 1995.
- [23] M. Born and J. R. Oppenheimer. *Ann. Physik.*, 84:457, 1927.
- [24] P. Jorgensen and J. Simons. Second quantization-based methods in quantum chemistry. *Academic Press, New York*, 1981.
- [25] H. B. Schlegel. *Adv. Chem. Phys.*, 67:249, 1987.
- [26] R. W. Grimes, C. R. A. Catlow, and A. L. Shluger. Quantum mechanical cluster calculation in solid-state studies. *World Scientific, Singapore*, 1992.
- [27] T. A. Kaplan and S. D. Mahanti. Electronic properties of solids using cluster methods. *Plenum, New York*, 1995.
- [28] G. Pacchioni, P. S. Bagus, and F. Parmigiani. Cluster models for surface and bulk phenomena. *Plenum Press, New York*, 1992.
- [29] P. M. W. Gill, B. G. Johnson, J. A. Pople, and S. W. Taylor. *J. Chem. Phys.*, 96:7178, 1992.
- [30] P. P. Ewald. *Ann. Physik*, 64:253, 1921.
- [31] J. B. Foresman, M. Head-Gordon, J. A. Pople, and M. J. Frisch. *J. Phys. Chem.*, 96:135, 1992.
- [32] J. A. Pople, R. Seeger, and R. Krishnan. *Int. J. Quant. Chem. Symp.*, 11:149, 1977.
- [33] J. A. Pople, M. Head-Gordon, and K. Raghavachari. *J. Chem. Phys.*, 87:5968, 1987.
- [34] W. Hübner and K. H. Bennemann. *Phys. Rev. B.*, 40:5973, 1989.
- [35] K. Terakura, A. R. Williams, T. Oguchi, and J. Kübler. *Phys. Rev. B*, 40:4734, 1984.
- [36] M. R. Castell, P. L. Wincott, N. G. Condon, C. Muggelberg, G. Thornton, S. L. Dudarev, A. P. Sutton, and G. A. D. Briggs. *Phys. Rev. B*, 55:7859, 1997.
- [37] J. Hubbard. *Proc. Roy. Soc. London, Ser. A*, 276:238, 1963.

- 
- [38] P. W. Anderson. *Phys. Rev.*, 115:2, 1959.
- [39] G. A. Sawatzky and J. W. Allen. *Phys. Rev. Lett.*, 53:2339, 1984.
- [40] R. J. Powell and W. E. Spicer. *Phys. Rev. B*, 2:2182, 1970.
- [41] P. Kuiper, G. Kruizinga, J. Ghijsen, G. A. Sawatzky, and H. Verweij. *Phys. Rev. Lett.*, 62:221, 1989.
- [42] S. Hüfner, P. Steiner, F. Reinert, H. Schmitt, and P. Sandl. *Z. Physik. B*, 88:247, 1992.
- [43] A. Fujimori and F. Minami. *Phys. Rev. B*, 29:5225, 1984.
- [44] A. Fujimori and F. Minami. *Phys. Rev. B*, 30:957, 1984.
- [45] Z. X. Shen, R. S. List, D. S. Dessau, B. O. Wells, O. Jepsen, A. J. Arko, R. Bartlett, C. K. Shih, F. Parmigiani, J. C. Huang, and P. A. P. Lindberg. *Phys. Rev. B*, 44:3604, 1991.
- [46] T. C. Leung, C. T. Chan, and B. N. Harmon. *Phys. Rev. B*, 44:2923, 1991.
- [47] Ph. Dufek, P. Blaha, V. Sliwko, and K. Schwarz. *Phys. Rev. B*, 49:10170, 1994.
- [48] Z. Szotek, W. M. Temmerman, and H. Winter. *Phys. Rev. B*, 47:4029, 1993.
- [49] S. L. Dudarev, G. A. Botton, S. Y. Savrasov, Z. Szotek, W. M. Temmerman, and A. P. Sutton. *Phys. Status Solidi A*, 166:429, 1998.
- [50] A. Svane and O. Gunnarsson. *Phys. Rev. Lett.*, 65:1148, 1990.
- [51] V. I. Anisimov, J. Zaanen, and O. K. Andersen. *Phys. Rev. B*, 44:943, 1991.
- [52] D. Ködderitzsch, W. Hergert, W. M. Temmerman, Z. Szotek, A. Ernst, and H. Winter. *Phys. Rev. B*, 66:64434, 2002.
- [53] A. V. Soudackov, A. L. Tchougreeff, and I. A. Misurkin. *Int. J. Quant. Chem.*, 58:161, 1996.
- [54] R. Newman and R. M. Chrenko. *Phys. Rev.*, 114:1507, 1959.
- [55] A. Freitag, V. Staemmler, D. Cappus, C. A. Ventrice Jr., K. Al-Shamery, H. Kühlenbeck, and H.-J. Freund. *Chem. Phys. Lett.*, 210:10, 1993.
- [56] A. Gorschlüter and H. Merz. *Phys. Rev. B*, 49:17293, 1994.
- [57] B. Fromme, M. Schmitt, E. Kisker, A. Gorschlüter, and H. Merz. *Phys. Rev. B*, 50:1874, 1994.
- [58] B. Fromme, A. Hylla, C. Koch, E. Kisker, A. Gorschlüter, and H. Merz. *J. Magn. Magn. Mat.*, 148:181, 1995.

- 
- [59] B. Fromme, Ch. Kock, R. Deussen, and E. Kisker. *Phys. Rev. Lett.*, 75:693, 1995.
- [60] B. Fromme, M. Möller, Th. Anschutz, C. Bethke, and E. Kisker. *Phys. Rev. Lett.*, 77:1548, 1996.
- [61] D. Reinen and B. Bunsenges. *Phys. Chem.*, 69:82, 1965.
- [62] B. D. Bird, G. A. Osborne, and P. J. Stephens. *Phys. Rev. B*, 5:1800, 1972.
- [63] M. Belkhir and J. Hugel. *Solid State Commun.*, 70:471, 1989.
- [64] W. C. Mackrodt and C. Noguera. *Surf. Sci.*, 457:L386, 2000.
- [65] C. de Graaf, R. Broer, and W. C. Nieuwpoort. *Chem. Phys.*, 208:35, 1996.
- [66] M. Geleijns, C. de Graaf, R. Broer, and W. C. Nieuwpoort. *Surf. Sci.*, 421:106, 1999.
- [67] R. W. Terhune, P. D. Maker, and C. M. Savage. *Phys. Rev. Lett.*, 8:404, 1962.
- [68] P. S. Pershan. *Phys. Rev.*, 130:919, 1963.
- [69] N. Bloembergen, R. K. Chang, and C. H. Lee. *Phys. Rev. Lett.*, 16:986, 1966.
- [70] Y. R. Shen. *Annu. Rev. Phys. Chem.*, 40:327, 1989.
- [71] M. Fiebig, D. Fröhlich, St. Leute, and R. V. Pisarev. *Appl. Phys. B*, 66:265, 1998.
- [72] D. Fröhlich, St. Leute, V. V. Pavlov, and R. V. Pisarev. *Phys. Rev. Lett.*, 81:3239, 1998.
- [73] M. Trzeciecki, A. Dähn, and W. Hübner. *Phys. Rev. B*, 60:1144, 1999.
- [74] C. C. J. Roothaan. *Rev. Mod. Phys.*, 23:69, 1951.
- [75] P. C. Hariharan and J. A. Pople. *Theor. Chim. Acta.*, 28:213, 1973.
- [76] M. M. Francl, W. J. Pietro, W. J. Hehre, J. S. Binkley, M. S. Gordon, D. J. DeFrees, and J. A. Pople. *J. Chem. Phys.*, 77:3654, 1982.
- [77] P. J. Hay and W. R. Wadt. *J. Chem. Phys.*, 82:270, 1985.
- [78] W. R. Wadt and P. J. Hay. *J. Chem. Phys.*, 82:284, 1985.
- [79] P. J. Hay and W. R. Wadt. *J. Chem. Phys.*, 82:299, 1985.
- [80] T. H. Dunning Jr. *J. Chem. Phys.*, 90:1007, 1989.
- [81] J. A. Pople. Nobel lecture: Quantum chemical models. *Reviews of Modern Physics*, 71:1267, 1999.
- [82] A. I. Boldyrev and J. Simons. *J. Phys. Chem.*, 100:8023, 1996.

- [83] G. E. Scuseria and H. F. Schaefer III. *J. Chem. Phys.*, 90:3700, 1989.
- [84] J. Cizek. *J. Chem. Phys.*, 45:4256, 1966.
- [85] R. Krishnan and J. A. Pople. *Int. J. Quant. Chem.*, 14:91, 1978.
- [86] R. Krishnan, M. J. Frisch, and J. A. Pople. *J. Chem. Phys.*, 72:4244, 1980.
- [87] J. Gauss and D. Cremer. *Chem. Phys. Lett.*, 150:280, 1988.
- [88] C. Møller and M. S. Plesset. *Phys. Rev.*, 46:618, 1934.
- [89] S. Yabushita, Z. Zhang, and R. M. Pitzer. *J. Phys. Chem. A*, 103:5791, 1999.
- [90] R. M. Pitzer and N. W. Winter. *Int. J. Quant. Chem.*, 40:773, 1991.
- [91] H. Lischka, R. Shepard, F. B. Brown, and I. Shavitt. *Int. J. Quantum Chem., Quantum Chem. Symp.*, 15:91, 1981.
- [92] R. Shepard, I. Shavitt, R. M. Pitzer, D. C. Comeau, M. Pepper, H. Lischka, P. G. Szalay, R. Ahlrichs, F. B. Brown, and J. Zhao. *Int. J. Quantum Chem., Quantum Chem. Symp.*, 22:149, 1988.
- [93] H. Lischka, R. Shepard, R. M. Pitzer, I. Shavitt, M. Dallos, Th. Müller, P. G. Szalay, M. Seth, G. S. Kedziora, S. Yabushita, and Z. Zhang. *Phys. Chem. Chem. Phys.*, 3:664, 2001.
- [94] H. Lischka, R. Shepard, I. Shavitt, R. M. Pitzer, M. Dallos, Th. Müller, P. G. Szalay, F. B. Brown, R. Ahlrichs, H. J. Böhm, A. Chang, D. C. Comeau, R. Gdanitz, H. Dachsel, C. Ehrhardt, M. Ernzerhof, P. Höchtl, S. Irlé, G. Kedziora, T. Kovar, V. Parasuk, M. J. M. Pepper, P. Scharf, H. Schiffer, M. Schindler, M. Schüler, M. Seth, E. A. Stahlberg, J.-G. Zhao, S. Yabushita, and Z. Zhang. *COLUMBUS, an ab initio electronic structure program, release 5.8*, 2001.
- [95] R. B. Ross, W. C. Ermler, and P. A. Christiansen. *J. Chem. Phys.*, 84:3297, 1986.
- [96] R. M. Pitzer and N. W. Winter. *J. Phys. Chem.*, 92:3061, 1988.
- [97] P. Hafner and W. H. E. Schwarz. *Chem. Phys. Lett.*, 65:537, 1979.
- [98] G. J. M. Janssen and W. C. Nieuwpoort. *Phys. Rev. B.*, 38:3449, 1988.
- [99] R. W. G. Wyckoff. *Crystal Structures, Interscience, New York*, 1964.
- [100] B. R. Brooks, W. D. Laidig, P. Saxe, J. D. Goddard, Y. Yamaguchi, and H. F. Schaefer III. *J. Chem. Phys.*, 72:4652, 1980.
- [101] R. Krishnan, H. B. Schlegel, and J. A. Pople. *J. Chem. Phys.*, 72:4654, 1980.
- [102] M. R. Welton-Cook and M. Prutton. *J. Phys. C*, 13:3993, 1980.

- [103] F. P. Netzer and M. Prutton. *J. Phys. C*, 8:2401, 1975.
- [104] C. G. Kinniburgh and J. A. Walker. *Surf. Sci.*, 63:274, 1977.
- [105] W. C. Mackrodt, R. J. Davey, S. N. Black, and R. Cocherty. *J. Crystal Growth*, 80:441, 1987.
- [106] P. Hartman. *J. Crystal Growth*, 96:667, 1989.
- [107] J. M. Wittbrodt, W. L. Hase, and H. B. Schlegel. *J. Phys. Chem. B*, 102:6539, 1998.
- [108] T. Klüner, H.-J. Freund, J. Freitag, and V. Staemmler. *J. Chem. Phys.*, 104:10030, 1996.
- [109] T. Klüner, H.-J. Freund, J. Freitag, and V. Staemmler. *J. Mol. Cat. A*, 119:155, 1997.
- [110] G. A. Petersson, A. Bennett, T. G. Tensfeldt, M. A. Al-Laham, W. A. Shirley, and J. Mantzaris. *J. Chem. Phys.*, 89:2193, 1988.
- [111] M. J. Frisch, J. A. Pople, and J. S. Binkley. *J. Chem. Phys.*, 80:3265, 1984.
- [112] M. J. Frisch, G. W. Trucks, H. B. Schlegel, G. E. Scuseria, M. A. Robb, J. R. Cheeseman, V. G. Zakrzewski, J. A. Montgomery, R. E. Stratmann, J. C. Burant, S. Dapprich, J. M. Millam, A. D. Daniels, K. N. Kudin, M. C. Strain, O. Farkas, J. Tomasi, V. Barone, M. Cossi, R. Cammi, B. Mennucci, C. Pomelli, C. Adamo, S. Clifford, J. Ochterski, G. A. Petersson, P. Y. Ayala, Q. Cui, K. Morokuma, P. Salvador, J. J. Dannenberg, D. K. Malick, A. D. Rabuck, K. Raghavachari, J. B. Foresman, J. Cioslowski, J. V. Ortiz, A. G. Baboul, B. B. Stefanov, G. Liu, A. Liashenko, P. Piskorz, I. Komaromi, R. Gomperts, R. L. Martin, D. J. Fox, T. Keith, M. A. Al-Laham, C. Y. Peng, A. Nanayakkara, M. Challacombe, P. M. W. Gill, B. Johnson, W. Chen, M. W. Wong, J. L. Andres, C. Gonzalez, M. Head-Gordon, E. S. Replogle, and J. A. Pople. *Gaussian 98 (Revision A.1)*, Gaussian, Inc., Pittsburgh PA, 1998.
- [113] A. P. Cracknell. *Adv. Phys.*, 17:367, 1968.
- [114] J. Dewitz. PhD thesis, Martin-Luther-Universität Halle-Wittenberg, Halle, 1999.
- [115] M. D. Towler, N. L. Allan, N. M. Harrison, V. R. Saunders, W. C. Mackrodt, and E. Aprà. *Phys. Rev. B.*, 50:5041, 1994.
- [116] S. Hübner, J. Osterwalder, T. Riesterer, and F. Hulliger. *Solid State Commun.*, 52:193, 1984.
- [117] M. Trzeciecki and W. Hübner. *Phys. Rev. B.*, 62:13888, 2000.
- [118] M. Trzeciecki, O. Ney, G. P. Zhang, and W. Hübner. *Adv. in Solid State Phys.*, 41:547, 2001.
- [119] J. Ferguson and H. J. Guggenheim. *J. Chem. Phys.*, 44:1095, 1966.

- 
- [120] D. A. Kleinman. *Phys. Rev.*, 126:1977, 1962.
- [121] J. Hugel and C. Carabatos. *J. Phys. C*, 16:6723, 1983.
- [122] A. Hinchliffe. *Computational quantum chemistry. John Wiley and Son Press*, 1989.
- [123] P.A. Christiansen, Y.S. Lee, and K.S. Pitzer. *J. Chem. Phys.*, 71:4445, 1979.
- [124] Y.S. Lee, W.C. Ermler, and K.S. Pitzer. *J. Chem. Phys.*, 67:5861, 1977.
- [125] L.F. Pacios and P.A. Christiansen. *J. Chem. Phys.*, 82:2664, 1985.
- [126] M.M. Hurley, L.F. Pacios, P.A. Christiansen, R.B. Ross, and W.C. Ermler. *J. Chem. Phys.*, 84:6840, 1986.
- [127] L.A. LaJohn, P.A. Christiansen, R.B. Ross, T. Atashroo, and W.C. Ermler. *J. Chem. Phys.*, 87:2812, 1987.
- [128] R.B. Ross, J.M. Powers, T. Atashroo, W.C. Ermler, L.A. LaJohn, and P.A. Christiansen. *J. Chem. Phys.*, 93:6654, 1990.
- [129] R.B. Ross, J.M. Powers, T. Atashroo, W.C. Ermler, L.A. LaJohn, and P.A. Christiansen. *J. Chem. Phys.*, 101:1098, 1994.
- [130] L.R. Kahn, P. Baybutt, and D.G. Truhlar. *J. Chem. Phys.*, 65:3826, 1976.



# Acknowledgements

I have many appreciations for the help of many people.

First and foremost, I would like to thank my direct supervisor, Prof. Wolfgang Hübner for providing me with generous guidance, expert advice through all stages of this interesting research field and other wide-ranging research useful suggestions.

I wish to thank Prof. Jürgen Kirschner for providing me a very good opportunity to participate into his department at the Max-Planck-Institut für Mikrostrukturphysik, where I can find the excellent environment and condition for scientific work throughout my Ph.D. study.

I am grateful to my colleagues, Xianghong Qian, Mikolaj Trzeciecki, Torsten Andersen, Ricardo Gómez Abal, Natalya Dadoenkova, Yaroslav Pavlyukh, and Oleksandr Ney, who have provided me fruitful suggestions and discussions during my three years at MPI, Halle.

Special thanks go to my friends here (in Halle) and in Thailand for giving me continuous encouragement.

Finally, I would like to thank my parents, my elder brother and two my younger sisters, who have given me constant support and encouragement. Their love and companionship have been an essential source of strength to me during the past three years. Thanks.



# Summary

In this work, we have developed an *ab initio* theory for the second harmonic generation (SHG) from the NiO(001) surface. Our interest in this material is stipulated by the significant properties of transition metal oxides (TMOs), where the non-trivial magnetic properties are imposed by the complicated electronic structures of the partially filled  $3d$ -orbitals. These phenomena contain a great potential for the technological applications, in particular, for intensively developing computer area. Nowadays, NiO with its good insulating behavior (the band gap according to the experimental data is around 4.3 eV) and its magnetic property (NiO is a typical antiferromagnet) is a building element of magnetic recording and memory chip devices. Experimentally, the properties of the TMO surfaces and interfaces can conveniently be assessed by the technique of optical SHG, which has a unique potential to easily access antiferromagnetism occurring at surfaces and interfaces of materials which possess inversion symmetry.

Therefore, the work presented here has two main implications: first, we investigate the electronic structure and excitations of NiO by means of *ab initio* calculations. This part treats some aspects of optical spectra in a UV/visible range from the solid state material by using first-principles. Second, using many-body wave functions and energies resulting from the previous assignments, we compute the non-linear optical response of the NiO(001) surface. Finally, this allows us to obtain the intensity of SHG from the NiO(001) surface.

According to these objectives, we state our work as follows.

For the extensive investigations of the electronic structure and excitations needed, several approaches are possible to build a theory:

- Time dependent density functional theory: for example, the time dependent local density approximation (TDLDA), which has been widely applied in physics and quantum chemistry.
- Correlation methods such as the local density approximation (LDA) with gradient corrections (necessary to correctly account and predict magnetic phenomena): Green's function (GW) calculations for the improvement of the band gaps (the band gaps are poorly described by the LDA) and numerical solution of the Bethe-Salpeter equation (necessary for the optical properties).
- Density functional calculations have tended to include modifications, such as self interaction corrected (SIC) LSDA which offers an improved description of band gap compared with the LSDA.

- Correlation methods originated from the quantum chemistry calculations: in particular, the configuration interaction (CI) approach.

On the first stage of our work, we follow the last route, which is the most flexible in our opinion, allowing us to use the highly advanced methods for the investigation of ground and excited states properties, in solid-state physics.

Using *ab initio* quantum chemistry calculations, the small  $(\text{NiO}_5)^{8-}$  and  $(\text{NiO}_6)^{10-}$  clusters were embedded in a set of point charges to model the NiO(001) surface and bulk NiO, respectively. Special care is attributed to a set of point charges surrounding the bare cluster in order to correctly account for the electrostatic environment due to the rest of crystal framework. In our work, we set all distances between Ni and O atoms according to the experimental data without performing the geometric optimization. By comparing the results of different sizes of embedded cluster models, the optimum configurations are found:  $15 \times 15 \times 15$  ions and  $15 \times 15 \times 7$  ions for the bulk NiO and NiO(001) surface, respectively.

Starting from the unrestricted Hartree-Fock (UHF) level of theory, we calculate ground-state properties to provide some insight of electronic structure and excitation. We estimate the excitation energies and oscillator strengths using the single excitation configuration interaction (CIS) technique. We then demonstrate the electron correlation effects on the *d-d* transitions at several levels of *ab initio* correlated theory such as CI calculation with all double substitutions (CID) and CI calculation with all single and double substitutions (CISD). Our main method, the quadratic configuration interaction with all single, double, and triple substitutions (QCISD(T)) approach, more fully includes electronic correlation effects by building the configuration space of many-body wave functions as a combination of excitations. This method is the most accurate approximation used by us. We note that all *ab initio* embedded cluster calculations were done with the GAUSSIAN98 package.

Our main results for the optical properties of the bulk NiO and NiO(001) surface are summarized below:

- We obtain an estimated optical band gap of 7.6 eV resulting from charge-transfer excitations between O(2p) and Ni(4s) states by employing the CIS calculation, which is much higher than the experimental value of bulk NiO (4.3 eV) but yet can be a good starting point to allow for the investigation of the low-lying *d-d* excitations.
- We predict optical absorption spectra arising from charge-transfer excitations.
- We find *d-d* transitions in a range of 0 – 3 eV (for both the bulk NiO and NiO(001) surface models), which are in an excellent agreement with available experimental and theoretical data.
- We also find large electronic correlation effects on the *d-d* excitations.

On the second stage of our work, the non-linear optical properties of the NiO(001) surface are computed by using the energies and wave functions from the former calculations. It is well known that the systems with inversion symmetry yield no response on the double frequency (no SHG tensor within the electric dipole transition approximation). This contradicts the experimental situation where SHG signal from NiO has been detected. There are two

possible explanations (different between bulk and surface resonances). First, SHG can result from the combination of the magnetic dipole and electric quadrupole transitions. In this case, the intensity of the response is quite low as a consequence of very small corresponding matrix elements. Second, the inversion symmetry breaking on the surface can be a source of SHG response from centrosymmetric NiO crystal. We advocate this possibility by computing the SHG intensity as a function of photon energy at different configurations of the light source and detector, and compare this with available experimental data. In addition, the contributions of each involved electronic transition to the  $(XXZ=XZX)$ ,  $(YYZ=YZY)$ ,  $(ZXX)$ , and  $(ZYY)$  non-linear susceptibility tensor are shown. This allows us to obtain the SHG intensity, which has been demonstrated to be a particularly versatile probe of magnetic interfaces and is expected to reveal new information on antiferromagnets.

We note that, for the optical spin manipulation, it is important to include spin-orbit coupling in the electronic theory. It is a new area of research, which still requires the development of new or extension of already existing methods. The lack of these methods is confirmed by the small effects of relativistic corrections. The strength of spin-orbit coupling, which is extremely important for transition-metals, rises with the increasing of atomic number. This imposes the third complication; the spin-orbit coupling must be incorporated in the computation of excited states.

Therefore, we consider the response of the relativistic part of Hamiltonian, which describes the spin-orbit coupling by using the CIS scheme implemented within the COLUMBUS package. These effects result in the splitting of the  $d-d$  excited states. These fine structures of low-lying excitations for both bulk NiO and the NiO(001) surface form an essential part of our work and have been obtained for the first time.

A number of the other problems of great interest, still remain and will be a subject of further work.

- So far, embedded clusters that consist of only one Ni atom have been used. The fast development of the computational equipment and numerical algorithms will enable an exploration of a large cluster that better represents the bulk NiO or NiO(001) surface.
- A highly interesting point is a computation of excited states with different spin multiplicity (singlets) and with different orbital angular momentum.
- Although the inclusion of electron correlations weakly affects the spin-orbit splitting, it is interesting to repeat the relativistic calculations on the CISD or higher level of theory.
- The knowledge of a larger number of states will enable a computation of optical properties in a larger energy interval and thus lead to a better comparison with experiment.



# Zusammenfassung

In dieser Arbeit haben wir eine *ab initio* Theorie für die optische Frequenzverdopplung (optical second harmonic generation, SHG) der NiO(001) Oberfläche konstruiert. Unser Interesse an diesem Material wird durch die bedeutenden Eigenschaften der Übergangsmetalloxide (transition-metal oxides, TMOs) begründet, deren nicht-triviale magnetische Eigenschaften durch die komplizierten, elektronischen Strukturen der teilweise gefüllten  $3d$ -Orbitale verursacht werden. Diese Phänomene enthalten ein großes Potential für die technologischen Anwendungen, insbesondere für den sich intensiv entwickelnden Computerbereich. Heutzutage ist NiO mit seinem guten, isolierenden Verhalten (der Bandabstand entsprechend den experimentellen Daten beträgt etwa 4,3 eV) und seiner magnetischen Eigenschaft (NiO ist ein typischer Antiferromagnet) ein Bauelement für magnetische Lese- und Schreibköpfe. Experimentell können die Eigenschaften der TMO-Oberflächen und -grenzflächen durch die Technik der optischen SHG bequem bestimmt werden. Diese bietet ein einzigartiges Potential, den Antiferromagnetismus leicht zugänglich zu machen, der an den Oberflächen und an den Grenzflächen der Materialien auftritt, die eine Zentral-Symmetrie besitzen.

Folglich hat die Arbeit, die hier vorgestellt wird, zwei Hauptimplikationen: Zunächst untersuchen wir die elektronische Struktur und Anregung von NiO mittels *ab initio*-Berechnungen. Dieser Teil behandelt einige Aspekte der optischen Spektren im ultravioletten/sichtbaren Bereich im Festkörper mittels first-principle Theorie. Zweitens berechnen wir mit Hilfe der Vielkörperwellenfunktionen und Energien, die aus den vorhergehenden Zuweisungen resultieren, die nicht lineare, optische Antwort der NiO(001) Oberfläche. Dies erlaubt es uns letztendlich, die Intensität der SHG für die die NiO(001) Oberfläche zu erhalten.

Entsprechend diesen Zielsetzungen gliedern wir unsere Arbeit wie folgt:

Für die umfangreichen Untersuchungen der benötigten elektronischen Struktur und Anregungen, sind mehrere Ansätze zum Aufbau einer Theorie möglich:

- zeitabhängige Dichtefunktionaltheorie: z.B. zeitabhängige, lokale Dichtenäherung (TD-LDA), die weitgehend in der Physik und der Quantenchemie angewendet wird.
- Korrelationsmethoden wie z.B die lokale Dichtenäherung (LDA) mit einer Gradientenkorrektur (notwendig, um magnetische Phänomene richtig zu erklären und vorauszusagen): Greenfunktionsberechnungen (GW) für die Verbesserung der Übereinstimmung der theoretisch und experimentell bestimmten Bandlücke (Bandlücken werden schlecht durch die LDA beschrieben) und die numerische Lösung der Bethe-Salpeter-Gleichung (notwendig für die optischen Eigenschaften).

- Dichtefunktional-Berechnungen beinhalten in zunehmendem Maße Abänderungen, wie z.B. die Selbst-Wechselwirkungskorrigierte, sogenannte (SIC) LSDA, welche, verglichen mit der LSDA, eine verbesserte Beschreibung der Bandlücke liefert.
- Korrelationsmethoden, die aus Quantenchemieberechnungen erzeugt werden: insbesondere der Konfigurationswechselwirkungsansatz (CI).

Im ersten Stadium unserer Arbeit, folgen wir dem letzten Weg, der unserer Meinung nach der flexibelste ist. Er erlaubt uns die Anwendung von sehr fortgeschrittenen Methoden zur Untersuchung der Eigenschaften der angeregten und der Grundzustände in der Festkörperphysik.

Mit Hilfe von *ab initio* Quantenchemieberechnungen, wurden die kleinen  $(\text{NiO}_5)^{8-}$ - und  $(\text{NiO}_6)^{10-}$ -Cluster in einer Anordnung von Punktladungen eingebettet, um die NiO(001)-Oberfläche bzw. den NiO-Festkörper zu modellieren. Besondere Aufmerksamkeit gilt der Anordnung von Punktladungen, die den freiliegenden Cluster umgeben, um die elektrostatische Umgebung, die durch das restliche Kristallgitter erzeugt wird, korrekt wiederzugeben.

In unserer Arbeit setzen wir alle Abstände zwischen Ni- und O-Atome auf den entsprechenden experimentellen Wert, ohne die Geometrieoptimierung durchzuführen. Durch den Vergleich der Resultate der unterschiedlichen Größen der eingebetteten Clustermodelle könnten die optimalen Größen gefunden werden:  $15 \times 15 \times 15$  Ionen und  $15 \times 15 \times 7$  Ionen für den NiO-Festkörper bzw. die NiO(001)-Oberfläche.

Beginnend vom theoretischen, uneingeschränkten Hartree-Fock (unrestricted HF) Niveau errechnen wir die Eigenschaften des Grundzustands, um Einblicke in die elektronische Struktur und Anregung zu erhalten. Wir schätzen die Anregungsenergien und die Oszillatorstärken mit Hilfe der Einzelanregungskonfigurationswechselwirkungstechnik (configuration interaction with single virtual excitations, CIS). Anschließend demonstrieren wir die Elektronenkorrelationseffekte anhand der *d-d* Übergänge auf verschiedenen Niveaus der korrelierten *ab initio* Theorie, wie z.B. die CI-Berechnung mit allen Doppelsubstitutionen (configuration interaction with double virtual excitations, CID) und CI-Berechnung mit allen Einzel- und Doppelsubstitutionen (configuration interaction with single and double virtual excitations, CISD). Unsere Hauptmethode, die quadratische Konfigurationswechselwirkungsapproximation mit allen Einzel-, Doppel- und Dreifachanregungen (QCISD(T)) erklärt die elektronischen Korrelationseffekte besser, indem sie den Konfigurationsraum der Vielkörperwellenfunktionen als Kombination von Anregungen betrachtet. Diese von uns verwendete Methode ist die genaueste Näherung. Wir merken an, daß alle Berechnungen der *ab initio* eingebetteten Cluster mit dem GAUSSIAN98 Paket erfolgten.

Unsere Hauptresultate für die optischen Eigenschaften des NiO-Festkörpers und der NiO(001)-Oberfläche werden folgendermaßen zusammengefaßt:

- Wir erhalten durch CIS-Berechnungen einen geschätzten Bandabstand von 7,6 eV, resultierend aus Ladungstransferanregung zwischen O(2p) und Ni(4s) Zuständen. Das ist viel höher als der experimentelle Wert des NiO-Festkörpers (4,3 eV), kann aber ein guter Ausgangspunkt die Untersuchung tiefliegender *d-d* Anregungen sein.
- Wir sagen die optischen Absorptionsspektren voraus, die aus den Ladungstransferanregungen resultieren.

- Wir finden  $d-d$ -Übergänge in einem Bereich von 0–3 eV (für die NiO-Festkörper- und die NiO(001)-Oberflächenmodelle), die gut mit den verfügbaren theoretischen und experimentellen Daten übereinstimmen.
- Wir finden außerdem große elektronische Korrelationseffekte bei  $d-d$ -Anregungen.

Im zweiten Stadium unserer Arbeit, werden die nicht linearen, optischen Eigenschaften der NiO(001) Oberfläche unter Verwendung der Energien und Wellenfunktionen aus früheren Berechnungen bestimmt. Es ist bekannt, daß Systeme mit Inversionssymmetrie keine Antwort bei der doppelten Frequenz abgeben (kein SHG-Tensor für die elektrische Dipolübergangsnäherung). Das widerspricht jedoch den Experimenten, in denen SHG-Signale von NiO detektiert wurden. Dafür gibt es zwei mögliche Erklärungen. Erstens kann SHG aus einer Kombination von magnetischen und der elektrischen Quadrupolübergängen resultieren. In diesem Fall ist die Intensität der Antwort als Folge der sehr kleinen korrespondierenden Matrixelemente ziemlich niedrig. Zweitens kann eine an der Oberfläche gebrochene Inversionssymmetrie eine Quelle der SHG-Antwort eines zentralsymmetrischen NiO-Kristalls sein. Wir unterstützen diese Erklärungsmöglichkeit, indem wir die SHG-Intensität als Funktion der Photonenergie bei unterschiedlichen Konfigurationen von Lichtquelle und Detektor berechnen und diese mit den vorhandenen experimentellen Daten vergleichen. Zusätzlich werden die Beiträge aller beteiligten elektronischen Übergänge zu den nicht-linearen Suszeptibilitätstensoren ( $XXZ=XZX$ ), ( $YYZ=YZY$ ), ( $ZXX$ ) und ( $ZYY$ ) gezeigt. Dieses erlaubt uns, die SHG-Intensität zu erhalten, welche sich als ein besonders vielseitiger Sensor für magnetische Grenzflächen erwiesen hat, und von welcher man sich neue Informationen über Antiferromagneten erhofft.

Wir merken an, dass es für die optische Spinmanipulation wichtig ist, die Spinbahnkopplung in die elektronische Theorie einzubeziehen. Es ist ein neues Forschungsgebiet, das die Entwicklung von neuen oder die Erweiterung bereits vorhandener Methoden erfordert. Der Mangel an solchen Methoden wird durch die kleinen Effekte der relativistischen Korrekturen betätigt. Die Stärke der Spinbahnkopplung, welche für die Übergangsmetalle extrem wichtig ist, steigt mit wachsender Atomzahl an. Das bürdet uns eine dritte Schwierigkeit auf; die Spinbahnkopplung muß in die Berechnung der angeregten Zustände eingebunden werden.

Innerhalb des COLUMBUS-Programms nutzen wir das CIS-Schema, um die relativistische Antwort des Hamilton-Operators zu betrachten, welcher die Spinbahnkopplung beschreibt. Diese Effekte resultieren aus der Aufspaltung der angeregten  $d-d$ -Zustände. Diese Feinstrukturen der tiefliegenden Anregung für den NiO-Festkörper und die NiO(001)-Oberfläche bilden einen wesentlichen Teil unserer Arbeit und sind zum ersten Mal berechnet worden.

Uns bleiben eine Reihe von anderen Problemen von großem Interesse, die Thema weiterer Arbeit sein werden:

- Bis jetzt bestanden die eingebetteten Cluster, die wir verwendet haben, aus nur einem Ni-Atom. Die schnelle Entwicklung der Computerausrüstung und der numerischen Algorithmen ermöglicht eine Erforschung von größeren Clustern, die den NiO-Festkörper oder die NiO(001)-Oberfläche besser repräsentieren.

- Ein sehr interessanter Punkt ist die Berechnung der angeregten Zustände mit einer anderen Spinmultiplizität (Singlet) und mit einem anderen Drehimpuls.
- Obgleich die Einbeziehung der elektronischen Wechselwirkungen nur schwach die aufgespaltenen Spinbahnorbitale beeinflusst, ist es interessant, die relativistischen Berechnungen mit Hilfe der CISD oder einer höheren Theorie zu wiederholen.
- Das Wissen über eine größere Anzahl von Zustände ermöglicht eine Berechnung der optischen Eigenschaften in einem größeren Energiebereich und führt folglich zu einer besseren Vergleichbarkeit mit dem Experiment.

# List of publications

- K. Satitkovitchai, Y. Pavlyukh, and W. Hübner, *Ab initio* embedded cluster study of optical second-harmonic generation below the gap of a NiO(001) surface, *Phys. Rev. B* **67**, 165413 (2003).
- R. Gómez-Abal, O. Ney, K. Satitkovitchai, and W. Hübner, All-optical subpicosecond magnetic switching in NiO(001), submitted to *Phys. Rev. Lett.*



# Erklärung

Hiermit erkläre ich, dass ich diese Dissertation selbstständig und ohne fremde Hilfe verfasst habe. Ich habe keine anderen als die angegebenen Quellen und Hilfsmittel benutzt. Die den benutzten Werken wörtlich oder inhaltlich entnommenen Stellen habe ich als solche kenntlich gemacht.

Halle (Saale), den 7. Mai 2003

Khompat Satitkovitchai



# Lebenslauf

Name : Satitkovitchai  
Vorname : Khompat  
Geburtsdatum : 22.03.1972  
Geburtsort : Bangkok (Thailand)  
Staatsangehörigkeit : Thailändisch  
Familienstand : ledig  
Kinder : keine  
Eltern:  
    Mutter : Saly Satitkovitchai (geb. am 26.02.1947)  
    Vater : Wichien Satitkovitchai (geb. am 21.05.1943)  
Geschwister:  
    Bruder : Khomkrit Satitkovitchai (geb. am 14.07.1970)  
    Schwester : Wichary Satitkovitchai (geb. am 10.05.1979)  
    Schwester : Witida Satitkovitchai (geb. am 17.06.1980)  
Ausbildung:  
    1990-1994 : Bachelor of Science (Physik) an der Universität  
              Ramkhamhaeng, Bangkok, Thailand  
    1996-1999 : Master of Science (Chemie) an der Universität  
              Kasetsart, Bangkok, Thailand  
    25.09.2000-2003 : Promotionsstudium an der Max-Planck-Institut für  
                    Mikrostrukturphysik, Halle, Germany  
                    unter der Leitung von Prof. W. Hübner  
Erfahrung  
    1994-1995 : Forscher an der Firma BEST (Bangkok Engineering  
              Service and Technology), Bangkok, Thailand  
    1999 : Lehrer (ein Semester) an der Universität Kasetsart,  
          Bangkok, Thailand  
Sprachkennt : Englisch und Thailändisch in Wort und Schrift